The Corrosion/Dissolution of Used Nuclear Fuel in a Deep Geologic Repository

NWMO-TR-2022-09   **April 2022**

Martin Badley and David Shoesmith

Western University

The Corrosion/Dissolution of Used Nuclear Fuel in a Deep Geological Repository

NWMO-TR-2022-09

April 2022

Martin Badley and David Shoesmith
Western University

Document History

Title:	The Corrosion/Dissolution of Used Nuclear Fuel in a Deep Geological Repository		
Report Number:	NWMO-TR-2022-09		
Revision:	R000	Date:	April 2022
Western University			
Authored by:	Martin Badley and David Shoesmith		
Nuclear Waste Management Organization			
Reviewed by:	Mehran Behazin, Mark Gobien, Tammy Yang, Mihaela Ion		
Accepted by:	Paul Gierszewski		

Revision Summary		
Revision Number	Date	Description of Changes/Improvements
R000	2022-04	Initial issue

ABSTRACT

Title:	**The Corrosion/Dissolution of Used Nuclear Fuel in a Deep Geological Repository**
Report No.:	**NWMO-TR-2022-09**
Author(s):	Martin Badley and David Shoesmith
Company:	Western University
Date:	April 2022

This report reviews the basic properties of UO_2 nuclear fuel, how they are changed by in-reactor irradiation, and how these changes influence fuel behaviour inside a failed used nuclear fuel container in a deep geologic repository (DGR). Studies conducted on UO_2 (pellet/powder), simulated spent fuel (SIMFUEL), alpha doped UO_2, and spent fuel have been reviewed. Radionuclides can be divided into those rapidly released on contact with groundwater (the instant release fraction (IRF), and those released at a rate controlled by the degradation rate of the fuel matrix (matrix inventory). For typical current fuel burn-up fuel, the IRF will be small with the matrix inventory comprising > 90% of the radionuclides. The corrosion and the consequent radionuclide release rate of the fuel will be controlled by the redox conditions produced at the fuel surface by the radiolysis of water (to produce predominantly H_2O_2 and H_2) and by the anoxic corrosion of the steel vessel in the presence of groundwater to produce the potential reductants Fe^{2+} and H_2. Assuming a reasonable containment period of nuclear fuel in containers prior to contact of groundwater with the fuel, alpha radiolysis will be the dominant radiation source.

If Fe^{2+} and H_2 are not considered, the fuel corrosion release rate will be proportional to the alpha radiation source strength, with the dominant oxidant being H_2O_2. Greater than 95% of the H_2O_2 radiolytically-produced will undergo decomposition to H_2O and the much less aggressive oxidant, O_2, as a consequence of the stabilization of the UO_2 matrix by fission product doping. Of the groundwater species to which the fuel will be exposed, only HCO_3^- could lead to an increase in corrosion rate with Ca^{2+} and silicate leading to suppression of the corrosion rate. Any influence of groundwater pH will be negligible within the pH range of groundwaters anticipated in a DGR.

Both Fe^{2+} and H_2 lead to the suppression of fuel corrosion/radionuclide release with H_2 exerting the major influence. Both extensive experimental studies and model calculations show that even small (micromolar) H_2 concentrations, orders of magnitude below those that will be produced by steel corrosion, can completely suppress fuel corrosion. This can be attributed to the ability of H_2 to utilize both the UO_2 surface and noble metal particles (produced in the fuel by the in-reactor fission process) to catalyze its reaction with H_2O_2 leading to their recombination to H_2O, thereby avoiding corrosion of the UO_2 matrix by establishing reducing conditions

Under these reducing conditions only chemical dissolution can lead to destruction of the fuel matrix and radionuclide release. Since in the reduced state, U^{IV} existing in the fuel has an extremely low solubility, and transformation of the UO_2 matrix to a more stable phase (such as coffinite) is very unlikely, fuel dissolution leading to radionuclide release should be extremely slow. This conclusion is strongly supported by analyses of the Cigar Lake uranium ore deposit which demonstrates stability of uranium in the predominantly reduced state (as U^{IV}). The geochemical observations, chemical analyses, and radiolysis model calculations performed on this uranium ore deposit demonstrate the major role of H_2 in maintaining U in the reduced U^{IV} state.

TABLE OF CONTENTS

Page

TABLE OF TABLES

Page

TABLE OF FIGURES

Page

1. INTRODUCTION

Permanent disposal of used nuclear fuel in a deep geologic repository (DGR) is the internationally preferred option and has been extensively studied in Canada since the 1970s. The internationally accepted design concept of a DGR involves disposal at a depth of about 500 m in suitably dense intact rock. To ensure containment, the fuel will be sealed in a corrosion resistant container capable of withstanding the anticipated hydrostatic, lithostatic and glaciation loads. To provide long term containment, a multiple barrier approach is planned, involving the fuel waste form, durable metal container, bentonite clay buffer and seals around the container, and the intact rock.

While the container will provide long-term containment (Hall et al. 2021), it is necessary to consider the consequences of its failure which could lead to exposure of the fuel to groundwater. Since the fuel contains radioactive fission and activation products, its behaviour in contact with groundwater provides the critical radioactivity source term in the assessment of DGR safety (Werme and Lilja 2010).

Over the past few decades, a substantial international effort has been expended to determine the behaviour of spent fuel under a range of proposed DGR conditions (Werme and Lilja 2010; Johnson and Shoesmith 1988; Johnson et al. 1994, 1996; Shoesmith et al. 1995, 2005; Grambow et al. 1996a, 2008, 2010; Poinssot et al. 2005; Oversby 2000; Kienzler et al. 2015; USA Department of Energy 2004; Lemmens et al. 2019). This report will review the present understanding of fuel corrosion/dissolution leading to the release of radionuclides.

2. BASIC PROPERTIES OF URANIUM DIOXIDE

The universally common form of commercial nuclear fuel is uranium dioxide close to stoichiometric (UO_{2+x} with $0.001 \geq x \geq 0.0001$). Here a brief review of important UO_2 properties is included, a more extensive review having been published previously (Shoesmith et al. 1994 (and references therein)).

As with other actinide oxides, UO_2 adopts a cubic fluorite structure with each U atom surrounded by 8 equivalent nearest neighbour O atoms (Figure 1). An important feature of the lattice is the large, cubically coordinated interstitial sites, which can accommodate additional interstitial O atoms (O_I). In the stoichiometric form, UO_2 can be considered a Mott-Hubbard insulator with electronic conductivity requiring promotion of electrons from the fully occupied 5f level to the conduction band (Figure 2), a strongly activated process with an extremely low probability at room temperature.

The conductivity of UO_2 can be increased by either the introduction of O_I atoms into the many available lattice locations, as indicated in Figure 1, or by the replacement of a fraction of U^{IV} atoms in the matrix by lower valent species which create holes in the 5f band, with charge balance maintained by the creation of an equivalent concentration of U^V atoms (Shoesmith et al. 1994 (and references therein)). Since spent nuclear fuel contains significant quantities of lower valent dopants (in particular, rare earth (RE^{III}) atoms with the amount depending on in-reactor burn-up) and the O potential of the fuel increases with burn-up, both these changes would lead to an increase in the electrical conductivity of the fuel. This would facilitate the coupling of the

anodic and cathodic sites required to support corrosion. Since the formation of metallic alloys also occurs in reactor, this enhanced conductivity will also allow their coupling to the fuel matrix as catalytic anodes or cathodes depending on the redox conditions to which the fuel is exposed.
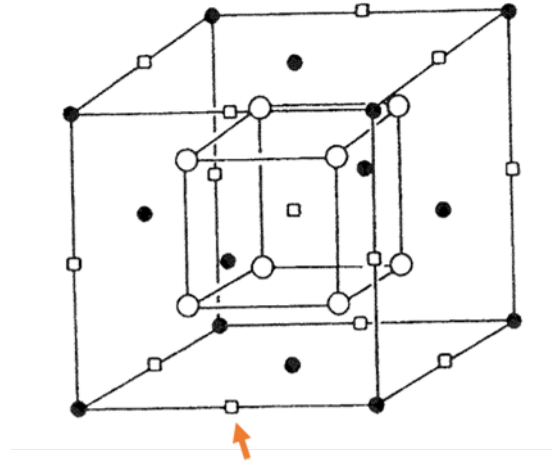
Figure 1: Cubic Fluorite Structure Adopted by Actinide Dioxides (● Uranium: ○ Oxygen: □ Cubically Coordinated Empty Interstitial Sites) showing Oxidation by the Injection of O^{II} into Interstitial Sites (Indicated by the Arrow) Leading to the Increase in Adjacent U Oxidation States
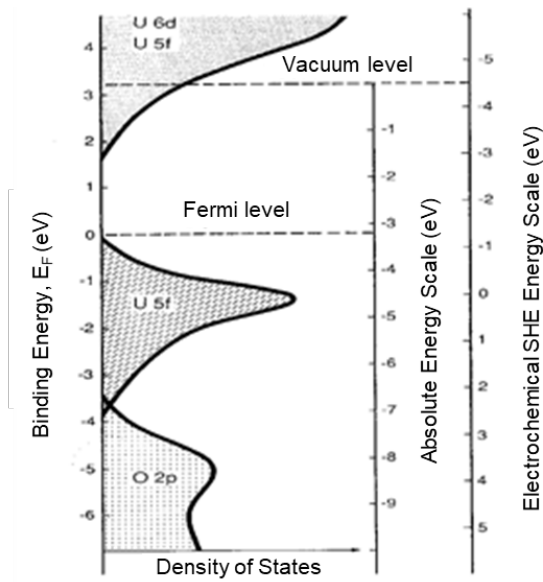
Figure 2: Schematic Energy Level Diagram for UO$_2$ Derived from Spectroscopic and Electrochemical Data (Expressed on the Standard Hydrogen Scale (SHE)). The Filled Valence Band Has Predominantly O 2p Character, and the Empty Conduction Band Consists Mainly of U5f, 6d and 7s States. The U5f Band Contains Two Electrons Per U Atom

The theoretical solubility of crystalline UO_2, calculated from thermodynamic data, is extremely low (Werme et al. 2004). However, measurements (Parks and Pohl 1988; Grenthe et al. 1992; Fuger 1997; Neck and Kim 2001; Rai et al. 2003; Casas et al. 1998; Yajima et al. 1995; Rai et al. 1990; Guillamont et al. 2020) yield values of the order of ~$10^{-9.5}$ mol/L for pH > 4 since the solid is generally not in the perfect crystalline form. Above pH ~ 4, the solubility is insensitive to pH, Figure 3.

Under oxidizing conditions, UO_2 can be oxidized to U^{VI}, e.g., as $U^{VI}O_2^{2+}$, and dissolve, since the solubility of U^{VI} is many orders of magnitude greater than that of U^{IV}, as shown for the common phase schoepite ($U^{VI}O_3 \cdot 2H_2O$) in Figure 3. This renders the fuel susceptible to oxidative dissolution (corrosion) when oxidants are present. Within the pH range anticipated in a DGR (~ 5.5 to 9.5), the common groundwater anions would be expected to increase the solubility of U^{VI} by the formation of soluble complexes but not that of U^{IV} which does not form anion-stabilized complexes (Shoesmith et al. 1994; Lemire and Tremaine 1980; Lemire and Garisto 1989; Paquette and Lemire 1981; Mühr-Ebert et al. 2019) (section 5.8 (below)).
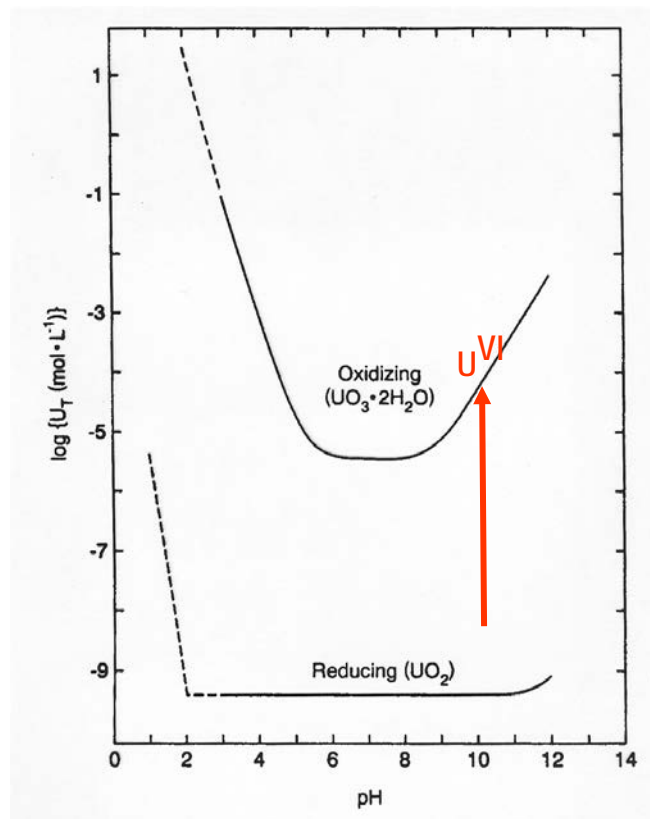
Figure 3: Solubilities of UO₂ and Schoepite (UO₃·2H₂O) as a Function of pH. The Vertical Arrow Indicates the Difference in Solubilities between Reduced U^{IV} and Oxidized U^{VI} States

3. PROPERTIES OF USED FUEL

For use in-reactor, UO_2 is fabricated in the form of ceramic pellets (94% to 97% of theoretical density). While CANDU (Canada Deuterium Uranium) fuel is unenriched (0.72% [235]U), light water reactor (LWR) fuel is enriched (up to 5%). Some LWR fuel is mixed oxide (MOX) fuel consisting of UO_2 blended with up to 5% PuO_2. CANDU fuel pellets are sealed within Zircaloy tubes and collected in multielement (usually 28 and 37) fuel bundles (Figure 4). CANDU fuel typically is exposed to burnups of 8.3-9.2 GWd/tU (200-220 MWh/kgU) (Lampman 2019). LWR fuels operate to higher burnup of about 50 GWd/tU because of their enrichment.

In-reactor burn-up leads to complex changes in the properties of the fuel (Hastings 1982; Johnson and Shoesmith 1988). Changes in fuel density occur as fabrication sintering porosity is eliminated and the generation of fission gas bubbles expands the lattice with bubbles interlinking to form grain boundary tunnels (Johnson and Shoesmith 1988; Hastings 1982; Hastings et al. 1978). At higher linear power ratings grain growth occurs and thermal stresses lead to cracking (Johnson and Shoesmith 1988). Collision cascades initiated by fission and alpha particle recoil events create a large number of atomic defects, with the final number of defects limited by thermal annealing (Matzke 1982). Inhomogeneity arises at both microscopic and macroscopic levels because of temperature and neutron flux gradients within the fuel. The key features of this evolution in microstructure of relevance to the present discussion are illustrated in Figure 5.
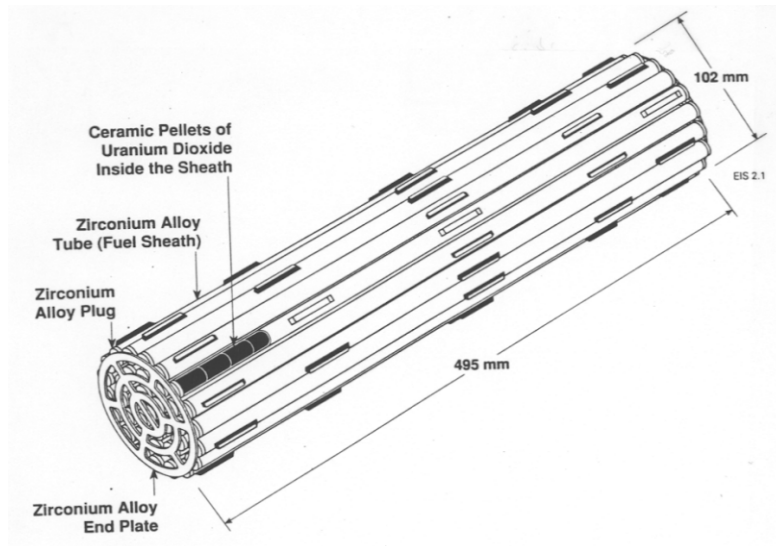
Figure 4: Schematic Illustration of a Canadian (CANDU) 37 Element Fuel Bundle

For CANDU fuel, the radial variation in grain size and porosity is small, while for LWR fuel a significant increase in porosity is observed around the rim of the fuel (Spino and Papaioannou 2000). The increased fission rate in this area in LWR fuel causes subdivision of the original grains and the increased formation and fission of Pu isotopes increases the burn-up leading to a higher fission product content and alpha activity (Rondinella and Wiss 2010).

Besides physical changes, in-reactor irradiation leads to the formation of a wide range of radionuclides as a result of fission reactions, e.g.,

$$^{235}U + n \rightarrow {}^{142}Ba + {}^{91}Kr + 3n \tag{1}$$
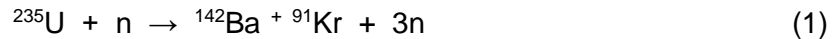
neutron capture, e.g.,

$$^{238}U + n \rightarrow {}^{239}Pu + e^- \tag{2}$$

And, to a lesser extent, activation, e.g.,

$$^{14}N + n \rightarrow {}^{14}C + {}^{1}H \tag{3}$$

where n denotes a neutron. Freshly discharged CANDU used fuel contains numerous radionuclides, with many decaying quickly. Analyses are available that list the radionuclide inventories (Heckmann and Edward 2020; Kleykamp 1985), and also identify those that are deemed important under disposal conditions (Gobien et al. 2021).
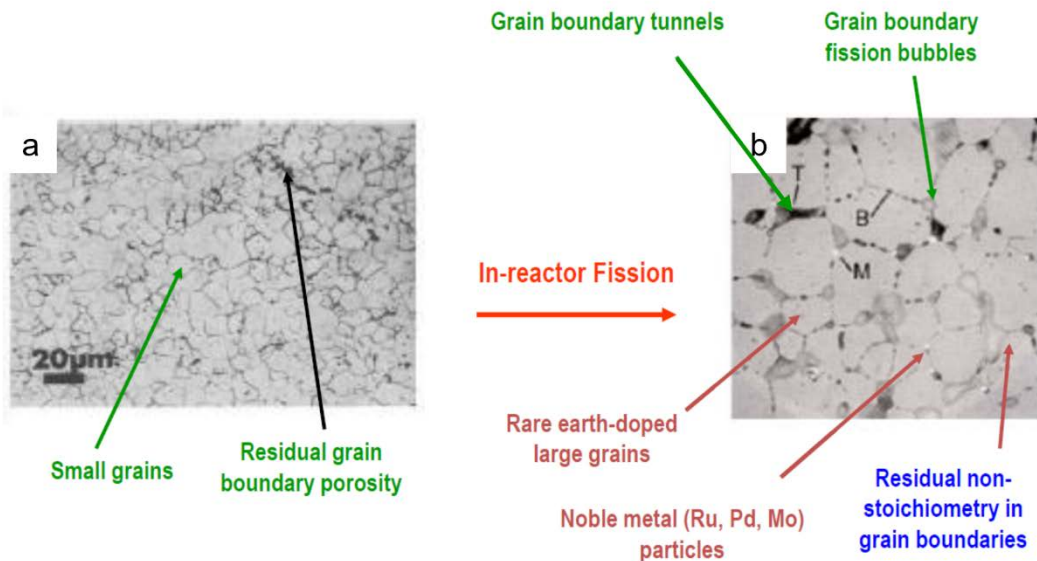
Figure 5: SEM Micrographs of UO$_2$ Fuel: (a) Unirradiated UO$_2$, (b) Fuel Irradiated at High Burn-up (770 MWh/kgU at 52 kW/m). In (a) Two Key Features of the Unirradiated Fuel are Noted. In (b) Some of the Key Features Caused by In-reactor Irradiation are Noted. Features of Irradiated Fuel Noted in Brown and Blue Can Be Simulated in Unirradiated UO$_2$ While Those in Green (in Panel b) Cannot

The chemical composition and microstructure of spent nuclear fuel have been studied in detail (Kleykamp 1985, 1988, 1993; Johnson and Shoesmith 1988; Hanson 1998). These studies show that, while the majority (> 90%) of fission and activation products remain at the location where they were formed, the high reactor operating temperatures lead to some redistribution. The species produced can be grouped according to their chemical behaviour.

(a)   Gaseous or volatile species, such as He, Kr, Cs, and I, have relatively high diffusion coefficients under in-reactor conditions and can migrate within the fuel. Small amounts of these species are expressed from the grains into cracks and voids in the fuel and the fuel-cladding gap. Slightly larger amounts become trapped at grain boundaries, while the majority remains as bubbles in the lattice.

(b)   Fission products which can form stable oxides incompatible with the UO_2 matrix (e.g., Rb, Cs, Ba, Zr, Nb, Mo, Tc, Sr) can separate into segregated oxides which adopt a perovskite structure with the general composition ABO_3 (A = Ba, Sr, Cs; B = Zr, Mo, U, Pu, rare earths).

(c)   Non-volatile species unstable as oxides (e.g., Mo, Ru, Pd) can diffuse within the fuel at high temperatures to form metallic alloy phases commonly referred to as noble metal (ε) particles.

(d)   Many elements, including actinides (including Np, Am, Pu, Cm), rare earths (including La, Ce, Pr, Nd, Pm, Sm, Eu, Gd, Y) and Sr, Zr, Ba, Te and Nb can remain as ion substitutes in the fuel matrix, within the limits of their solubility to the extent they have not precipitated as ABO_3 phases.

Two fission products exert additional influences on the fuel. Mo can coexist in the metallic and oxide forms and, hence, can maintain the fuel close to stoichiometry. Zr, which can be segregated to ABO_3 phases, can also be retained by the fuel matrix, within which it can exert an influence on the lattice dimensions. Finally, small inventories of activation products can form by neutron capture within the fuel cladding. Figure 6 summarizes this distribution of fission products, and actinides within the spent fuel matrix (Johnson and Shoesmith 1998).

The key thermodynamic factor that influences the chemical state of many fission products in the fuel is the O potential, which is initially very low since the used fuel is stoichiometric (Lindemer and Bessman 1985). However, burn-up raises the ratio of O to U because the O released cannot be completely bonded by the generated fission products many of which either possess lower oxidation states than IV or are stabilized in the metallic form (Cordfunke and Konings 1988). Much of this O is neutralized by formation of ZrMo oxide and reaction with the inner surface of the Zircaloy cladding (Kleykamp 1990; Floyd et al. 1992). For CANDU fuel, the approximate change in fuel stoichiometry has been calculated to range from $UO_{2.001}$ to $UO_{2.007}$ (Smith et al. 1987), while O/M measurements indicate only marginal fuel oxidation in both low and high burn-up LWR and BWR fuel (Une et al. 1981; Matzke and Matzke 1995).

The irradiation history of spent fuel is characterized by its power rating and burn-up, with the radionuclide inventory at the time of emplacement of the waste in the DGR depending on how long it has been since its discharge from the reactor. The age of the fuels to be placed in a Canadian DGR will vary with the earliest dating back to the 1950s for some research fuels. Because the DGR will not open before 2040, the ages of the fuel will range from 10 to > 60 years. The power rating and burn-up history of CANDU fuel is known (Lampman 2019), and the used fuel radionuclide inventories for CANDU fuel of various burn-ups have been calculated (Heckman and Edward 2020).
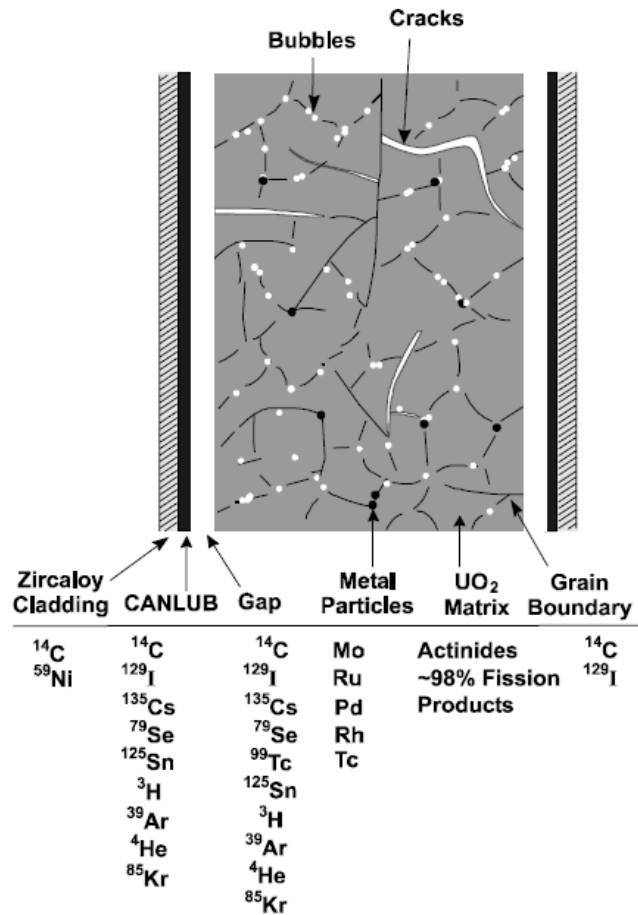
Figure 6: Schematic Illustration Showing the Conceptual Distribution of Fission and Activation Products within A Spent Fuel Element

Based on these studies, three radionuclide inventories can be defined, as illustrated in Figure 7.

(i)   The gap inventory, comprising volatile radionuclides which have accumulated in the fuel-cladding gap, which would be expected to be readily soluble and, hence, rapidly released on contact with groundwater.

(ii)   The inventory of radionuclides which have segregated to grain boundaries within the fuel. Their release will depend on their chemical nature and the chemical and physical properties of their location and could require a protracted period of groundwater exposure.

(iii)   The matrix inventory of radionuclides retained within the fuel grains whose release would be controlled by the corrosion/dissolution of the UO_2 matrix.
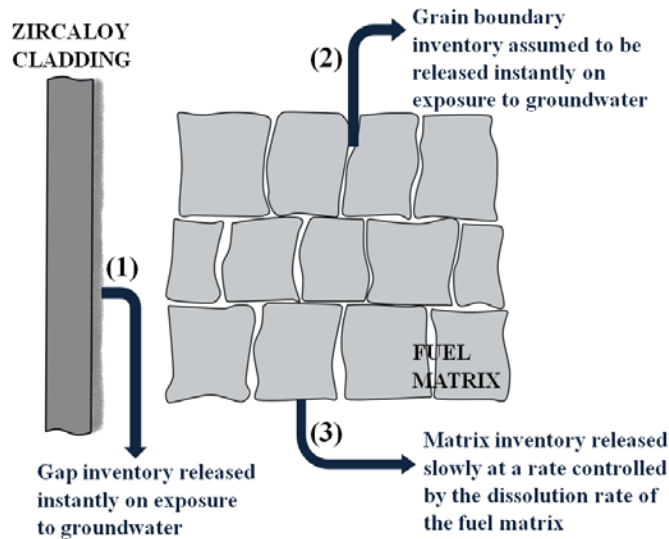
Figure 7: Conceptual Illustration of the Three Categories of Radionuclide within a Spent Fuel Element

Of these inventories, (i) and (iii) have been extensively studied, while determination of the grain boundary inventory ((ii)) is more difficult to assess despite considerable recent effort (Kienzler et al. 2015). As a consequence, when assessing radionuclide release, only two release fractions are considered: (a) an instant release fraction (IRF) comprising inventories (i) and (ii), and a matrix dissolution fraction comprising inventory (iii).

4. PROPERTIES OF USED FUEL AFTER DISCHARGE FROM REACTOR

4.1 Radionuclide Diffusion

Based on the extrapolation of measurements at high temperatures, it was calculated that thermally-induced diffusion of radionuclides within the fuel matrix can be considered negligible over an assumed container lifetime of 10^4 years (Ferry et al. 2006; Lovera et al. 2003). Since many of the radionuclides within the spent fuel matrix are alpha (α) particle emitters, the UO_2 crystalline structure could experience α-recoil damage after discharge from the reactor since the high temperatures which allow annealing of such damage in-reactor would no longer prevail. This damage has the potential to accelerate the athermal diffusion of volatile species from within the fuel grains to the grain boundaries. Such an increase in the grain boundary inventory would be an additional contribution to the IRF (Poinssot et al. 2005, 2006; Ferry et al. 2008; Lovera et al. 2003; NWMO 2019).

Calculations based on conservative assumptions were used to estimate the extent of transport of fission products to grain boundaries (Johnson et al. 2005; Poinssot et al. 2006) for LWR fuel. The cumulative fraction transported after 10^4 years was calculated to be 5% of the radionuclide inventory rising to an estimated 7-8% after 10^6 years. Desgranges et al. (2003) concluded that alpha self-irradiation would not significantly modify fission product distribution, with further calculations (Ferry et al. 2008) indicating that enhanced radionuclide diffusion via this

mechanism was approximately three orders of magnitude lower than earlier estimates. Given the lower burnup of CANDU fuel (by a factor of 5 to 6), such a redistribution of radionuclides, leading to an increase in the IRF, can be considered negligible.

4.2   Build-up of Helium Gas Pressure

The decay of α-emitters could damage the fuel via the accumulation of He atoms in the fuel potentially leading to lattice swelling and micro-cracking of grains (Ferry et al. 2008, 2010; Pencer et al. 2017). Conservative calculations based on the assumption all the He produced will be trapped in bubbles yield pressures which are much lower than the critical values derived from fuel rupture criteria, making grain rupture and the propagation of cracks unlikely in LWR fuel during the first 10^4 years of emplacement in a DGR (Ferry et al. 2008). Given the much lower burnups in CANDU fuel compared to LWR fuel, Pencer et al. (2017) concluded that significant effects from α-damage would not be expected (NWMO 2019).

4.3   Evolution of Activity Associated with the Fuel

On discharge from the reactor, the fuel is highly radioactive, but its activity decreases quickly with time. The overall radioactivity for CANDU fuel decreases after ~ 10 years to ~ 0.01% of its value on discharge. The evolution in radioactivity beyond 10 years is shown for reference CANDU fuel (220 MWh/kgU burn-up) in Figure 8. The basis for choosing this reference value has been discussed elsewhere (Heckman and Edward 2020). For a presently uncertain time up to, or possibly longer than, 100 years the fuel will be in dry storage.
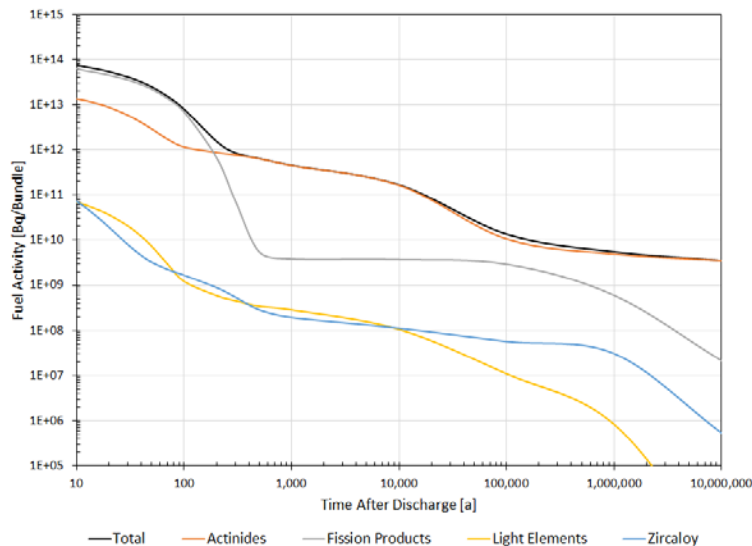
Figure 8: Radioactivity of Reference CANDU Used Fuel (220 MWh/kgU Burn-up) as a Function of Time after Discharge from Reactor (Gobien et al. 2021)

A majority of the gamma (γ) emitting fission products and activated impurities within the cladding will decay within the first 100 years (Figure 8), beyond which the decay will be dominated by α-particle emission predominantly from the actinide content. Since radioactivity is

related to the behaviour of specific radionuclides, both the overall decreases in activity level and the radionuclide composition of the fuel are important. Table 1 lists the initial composition of the CANDU fuel.

Table 1: Composition of Fresh and Used CANDU UO$_2$ Fuel Bundle (220 MWh/kgU Burnup, 30 Years Storage)

Component *	Fresh (Unirradiated) Bundle	Used Bundle
	Bundle Mass %	Bundle Mass %
Actinides		
U-238	79.41%	78.60%
Pu-239	-	0.22%
U-235	0.58%	0.14%
Pu-240	-	0.10%
U-236	-	0.06%
Th-232	0.04%	0.04%
Am-241	-	0.02%
Pu-242	-	0.01%
Pu-241	-	0.01%
U-234	0.004%	0.003%
Other Actinides	-	0.005%
Other Elements and Fission Products		
O	10.73%	10.79%
Zr	8.68%	8.73%
Zr-96	0.25%	0.28%
Sn (Stable)	0.16%	0.16%
Xe (stable)	-	0.13%
C (stable)	0.07%	0.07%
Mo (stable)	-	0.05%
Ce (stable)	-	0.05%
Ru (stable)	-	0.05%
Nd (stable)	-	0.05%
Ba (stable)	-	0.04%
Cs (stable)	-	0.03%
Nd-144	-	0.03%
Mo-100	-	0.02%
Tc-99	-	0.02%
Zr-93	-	0.02%
Cs-137	-	0.01%
Other Radionuclides	-	0.04%
Others Stable Isotopes	0.09%	0.24%

*Includes impurities naturally present in fuel

5. MATRIX CORROSION AND RADIONUCLIDE RELEASE UNDER DISPOSAL CONDITIONS

The determination of the behaviour of used nuclear fuel under disposal conditions requires the consideration of two radionuclide release processes on contact with groundwater assuming container failure has occurred: (i) the IRF, and (ii) the matrix corrosion/dissolution fraction. Since > 90% of radionuclides are contained within the solid-state matrix of the used fuel, the matrix corrosion/dissolution fraction would be expected to be dominant.

5.1   The Instant Release Fraction (IRF)

Determination of the IRF requires knowledge of the radionuclide inventories, the half lives and decay sequences of the individual radionuclides, and analytical measurements of the gap and grain boundary inventories. The half lives of most radionuclides are known and tabulated (Chadwick et al. 2011) and radionuclide inventories can be determined using well developed codes. The gap and grain boundary inventories can be measured by first puncturing the fuel cladding and measuring the fission gas released, and then leaching both clad fuel specimens (to obtain the gap inventory) and crushed fuel specimens (to obtain the gap and grain boundary inventories). The IRF of a specific radionuclide can then be determined by comparing the amount released to the calculated inventory. These measurements and calculations have been described in detail for various types of fuel (Gray et al. 1991; Roudil et al. 2007, 2009; Johnson and McGuinnes 2002) including CANDU fuel (Stroes-Gascoyne 1996; Stroes-Gascoyne et al. 1987, 1992a. 1992b, 1994), and thoroughly reviewed (Johnson and Shoesmith 1988; Kienzler et al. 2015; Gobien et al. 2018; Johnson et al. 2005). More recent studies have been described in detail for LWR fuel (Kienzler et al. 2015).

5.2   The Influence of Redox Conditions

The release of > 90% of radionuclides contained within the fuel matrix (the matrix inventory (iii)) will be governed by the corrosion/dissolution of the fuel. The rate of this process will be related to, but not necessarily directly proportional to, the solubility of uranium in the groundwater (Section 2). At DGR depths, groundwaters are inevitably O_2-free, and O_2 having been introduced during construction of the DGR and its operation prior to sealing will have been relatively rapidly consumed by mineral and biochemical reactions in the clays surrounding the emplaced waste container and by corrosion of the container materials, Cu and carbon steel in a Canadian DGR (Hall et al. 2021; King et al. 2017).

While groundwater entering a failed container may be anoxic, its radiolysis due to radioactive decay processes within the fuel will produce a variety of chemical species including oxidants which can oxidize the UO_2 to the more soluble $U^{VI}O_2^{2+}$ state (Figure 3), a process which can be considered a corrosion reaction. The thermodynamic driving force for a corrosion process is illustrated in Figure 9. The redox potential of the groundwater ($E_{Red/Ox}$, commonly termed E_h) must be greater than the equilibrium potential for fuel oxidative dissolution, $(E^e)_{UO2/(UO2)2+}$, with the driving force for corrosion being the potential difference, $(E^e)_{Red/Ox} - (E^e)_{UO2/UO2(2+)}$. Under these conditions, the fuel will establish a corrosion potential (E_{CORR}) at which the anodic dissolution rate and the cathodic reagent reduction rate are equal, with the overall corrosion reaction being

$$U^{IV}O_2 \ + \ Ox \ \rightarrow \ U^{VI}O_2^{2+} \ + \ Red \qquad\qquad\qquad (4)$$
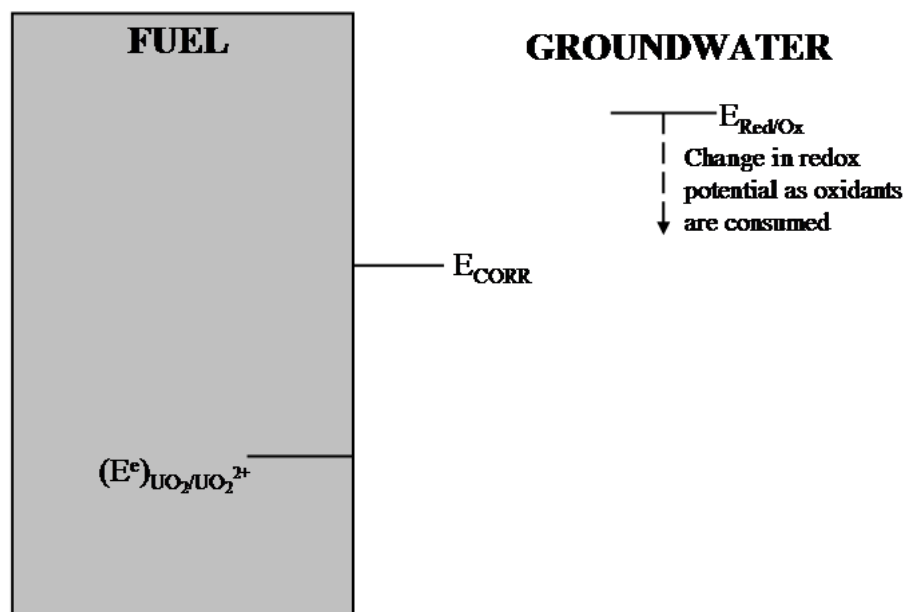
Figure 9: Illustration Demonstrating the Thermodynamic Driving Force for Fuel Corrosion in An Aqueous Solution Containing Oxidants: E_{CORR} Is the Corrosion Potential at Which the Overall Corrosion Process Occurs on the Fuel Surface

Early studies clearly demonstrate that the rate of this reaction is dependent on the redox conditions established inside a container containing groundwater, with corrosion rates determined by the available radiolytic oxidants (Werme et al. 2004; Johnson et al. 1996; Shoesmith et al. 2003; Sunder et al. 1997; Shoesmith and King 1998). Since radiation fields decay with time (Figure 10), the corrosion rate will decrease as the radiolytically-established redox conditions change with time.
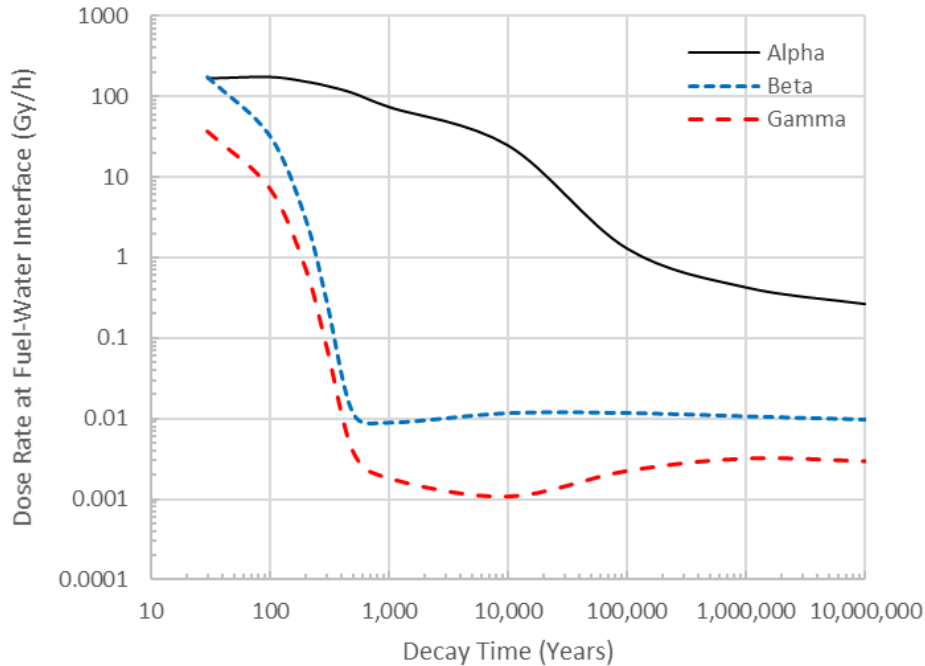
Figure 10: Alpha (α), Beta (β) and Gamma (γ) Dose Rates (Gy/h) as a Function of Time for a Layer of Water in Contact with a CANDU Fuel Bundle with a Reference Burn-up of 220 MWh/kgU (I. Ariani 2022)

Two corrosion fronts will exist within a failed container: one on the fuel surface driven by radiolytic oxidants, and a second one on the steel surface sustained by H_2O reduction producing the potential redox scavengers Fe^{2+} and H_2. Since a reasonable assumption is that waste containers will remain unbreached over a period of at least a few 100 years, when γ/β radiation fields are significant (Figure 10), only α-radiolysis is considered as a source of oxidants. Among α-radiolysis products only molecular oxidants, such as H_2O_2 (Ekeroth et al. 2006), are expected to be important since radical oxidants have short lifetimes and steady-state concentrations which are orders of magnitude lower than those of molecular products (Wren et al. 2005). Figure 11 shows the equilibrium potentials (E^e) for the coupled anodic and cathodic reactions on the two surfaces, and the respective E_{CORR} values adopted by the two surfaces in the neutral to slightly alkaline conditions anticipated under disposal conditions (Shoesmith 2000; Lee et al. 2006a, 2006b). The zone marked E_h indicates the redox condition possible at high α dose rates. The redox gradient between the two corroding surfaces is clearly apparent in the difference in E_{CORR} values established. The possibility that radiolytic oxidants will lead to passivation of the steel and, hence, the blocking of the supply of redox scavengers has been investigated and found to be negligible (Hill et al. 2015).
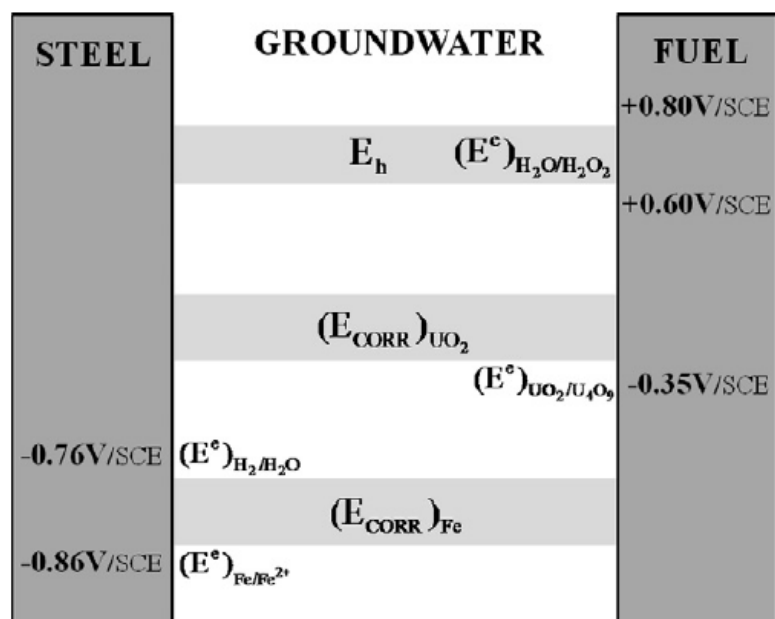
Figure 11: Illustration Showing the Two Corrosion Fronts Existing within a Failed, Groundwater Flooded Waste Container, One on the Fuel Surface Established by Reaction with Radiolytic Oxidants, and A Second One on the Steel Surface Established by Reaction with H₂O

As α-radiation fields evolve with time (Figure 10), both $(E^e)_{H2O/H2O2}$ and E_{CORR} on the UO₂ surface will decrease as the driving force for corrosion decreases. If E_{CORR} were to decrease to or below $(E^e)_{UO2/U4O9}$, the corrosion driving force would disappear and the fuel become electrochemically stable. If fuel degradation were to continue, it would have to be by chemical dissolution (as U^{4+}) not corrosion as $U^{VI}O_2^{2+}$. Calculations based on available thermodynamic data (Grenthe et al. 1992; Lemire and Tremaine 1980; Paquette and Lemire 1981) show that E_h would need to be ≤ -0.35 V (vs SCE) for this condition to apply.

5.3   Simulating Spent Fuel Properties

The properties of the spent fuel can be investigated directly, but the actual handling and security facilities required are elaborate and expensive. While most of the physical changes are difficult to simulate in unirradiated analogues (Section 2, Figure 5), termed SIMFUELs, the key chemical changes can be simulated. Various fuel specimens have been custom-fabricated and studied, ranging from SIMFUELs with different degrees of simulated burn-up to specimens with controlled degrees of average non-stoichiometry (x in UO_{2+x}). SIMFUELS are natural UO₂ doped with non-radioactive fission product elements (Ba, Ce, La, Mo, Sr, Y, Zr, Rh, Pd, Ru, Nd) to replicate the chemical effects of in-reactor burn-up (Lucuta et al. 1991). The SIMFUELS used in Canadian studies have ranged from 1.5 at% (9 GWd/MgU) (high burn-up CANDU fuel) to 6 at% (28 GWd/MgU) (low-burn-up LWR fuel). Non-stoichiometric specimens with nominal O/U ratios of 2.002, 2.011, 2.05, and 2.1 were prepared using a coulometric titration apparatus (Verrall et al. 2005; Corcoran et al. 2007).

Using SIMFUELs, it is possible to simulate the influence of lattice doping, especially with rare earths, and the dispersion of noble metal particles throughout the rare earth doped UO_2 lattice. As noted in Section 2, rare earth dopants increase the electrical conductivity of the UO_2 lattice. This, combined with the presence of noble metal particles, could facilitate corrosion by providing a network of separated and galvanically-coupled anodes (UO_2) and cathodes (ε-particles) which would be expected to influence fuel corrosion in the presence of oxidants and/or reductants.

Fuels recently discharged from reactor and stored for relatively short time periods do not represent those expected to be exposed to groundwaters after a considerable period of containment in a DGR. As shown in Figure 10, it would be expected that the β/γ radiation fields, which are intense in fuels shortly after discharge, will have decayed to insignificant levels over the early disposal period when the fuel would be isolated from groundwater by an intact container. By contrast α-radiation fields will persist over an extended period of time. The influences of α-radiation without interference from β/γ radiation have commonly been studied on unirradiated UO_2 specimens doped with α-emitters (most commonly ^{238}Pu, ^{239}Pu, ^{233}U) to levels which simulate spent fuels of various ages.

5.4   Oxidation of the Uranium Dioxide Surface

Uranium generally exists in one of three oxidation states, $U^{IV/V/VI}$, but is effectively only soluble as U^{VI} (Grenthe et al. 1992; Guillamont et al. 2020). Applying electrochemical methods, and subsequently analysing the surface by X-ray photoelectron spectroscopy (XPS), the composition of a $U^{IV}O_2$ surface has been mapped as a function of the potential applied to the surface. Figure 12 shows the increasingly oxidized state of the surface as the applied potential is increased from a value of -0.5 V (vs. SCE), which is below the potential at which the oxidation of UO_2 should commence (as discussed in Section 5.2), to a value of +0.5 V (vs SCE), which is well above any E_{CORR} achievable under open-circuit corrosion conditions in a DGR (Santos et al. 2004). The relative amounts of the three oxidation states observed at the lowest potential are indistinguishable from those measured on surfaces strongly reduced at -1.5 V (vs SCE) making them representative of the unoxidized $U^{IV}O_2$ surface. The procedures used to deconvolute spectra into contributions form U^{IV}, U^V and U^{VI}, have been described (Ilton et al. 2005, 2007; Schindler et al. 2009; Razdan et al. 2012).

All three oxidation states can be detected with the extent of oxidation proceeding through the compositional sequence indicated in Figure 12 (Santos et al. 2004; Broczkowski et al. 2007; Razdan and Shoesmith 2014b; Liu et al. 2018). Oxidation occurs in a two-step process,

$$U^{IV}O_2 \rightarrow U^{IV}_{1-2x}U^V_{2x}O_{2+x} \rightarrow U^{VI}O_3 \cdot yH_2O \tag{5}$$
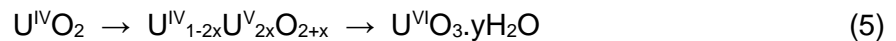
The first step involves the injection of O^{II} into vacant interstitial lattice sites (Figure 1) to form a thin (≤ 5 nm) U^{IV}/U^V surface layer. As the potential is increased, the outer regions of this layer are converted to a U^{VI} alteration product which can dissolve as $U^{VI}O_2^{2+}$. For high applied potentials, this alteration layer can dissolve more extensively at surface sites where the hydrolysis of already dissolved $U^{VI}O_2^{2+}$ leads to acidification,

$$nU^{VI}O_2^{2+} + yH_2O \rightarrow (U^{VI}O_2)_n(OH)_y^{(2n-y)+} + yH^+ \tag{6}$$
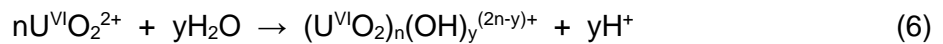
and an increase in solubility (Figure 3). This hydrolysis/acidification process leads to the decrease in U^{VI} which exposes the underlying U^{IV}/U^{V} layer (Figure 12).
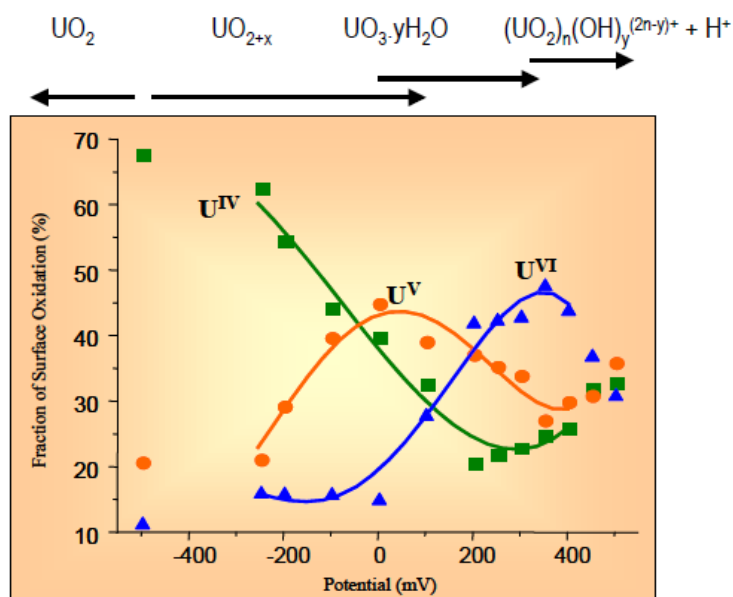
Figure 12: The Fractions of Various Oxidation States of U in a 1.5 at% SIMFUEL Electrode Surface as A Function of Applied Electrochemical Potential. The Electrode Was Anodically Oxidized at Each Potential for 1 Hour in 0.1 mol/L NaCl (pH = 9.5) Solution and then Analyzed by X-ray Photoelectron Spectroscopy (XPS) (Santos et al. 2004)

5.5   Reactivity of the Uranium Dioxide Surface

Attempts to measure fuel corrosion rates show a wide variation in fuel reactivity (Shoesmith and Sunder 1992; Oversby 1999; Poinssot et al. 2005) although it is often unclear whether these differences are attributable to real differences in reactivity or to differences in either experimental conditions, specimen treatment, or analytical measurements. Photothermal deflection spectroscopy measurements (Rudnicki et al. 1994), performed on undoped UO_2 in solutions not containing known complexants for UO_2^{2+}, detected anodic dissolution at potentials as low as -0.3 V (vs. SCE) suggesting the release could commence as soon as the oxidation of the matrix became thermodynamically possible. It was speculated, but not demonstrated, that dissolution at such low potentials could be due to the preferential oxidation and dissolution of non-stoichiometric grain boundaries. Early reports of a difference between the measured dissolution currents (in electrochemical measurements) (Nicol and Needes 1973) for single crystals and sintered discs by a factor of 10^3, and between the dissolution rates (measured chemically) for UO_2 and natural uraninite specimens containing ill-defined impurities (Grandstaff 1976), indicate that the presence of defects and impurities could exert a significant effect on fuel corrosion rates. These observations suggest that in-reactor burn-up leading to lattice doping with fission products and the formation of noble metal (ε) particles will have an influence on fuel corrosion rates.

5.6   Fission Product Doping

Fission product doping of the UO_2 lattice has been shown to change the kinetics of air oxidation of UO_2 (Thomas et al. 1993; Choi et al. 1996; Cobos et al. 1998; McEachern and Taylor 1998; Ha et al. 2006; McEachern et al. 1998; McEachern 1997; You et al. 2000; Hanson 1998; Campbell et al. 1989). This reaction proceeds in two stages,

$$UO_2 \; \rightarrow \; U_4O_9/U_3O_7 \; \rightarrow \; U_3O_8 \tag{7}$$
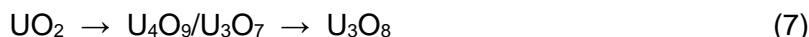
and a key feature is that the nature of the intermediate phase changes as the doping level is increased. For pure and lightly doped UO_2, oxidation occurs relatively rapidly to the tetragonal U_3O_7, and the subsequent conversion to the orthorhombic U_3O_8 is readily completed. However, the oxidation of UO_2 containing large amounts of dopants (such as Gd) is kinetically slower and proceeds through U_4O_9, which retains the fluorite structure, and is kinetically more difficult to transform to U_3O_8. These observations are supported by a range of studies with SIMFUEL (Lucuta et al. 1991), LWR fuels (highly doped) (Einziger et al. 1992) and CANDU fuel (Wasywich et al. 1993).

Park and Olander (1990, 1992) offered an explanation for the stabilization of RE^{III}-doped UO_2 against oxidation based on O potential calculations. The experimental O potential data could be fitted using a model which showed that, as the Gd level was increased, the lattice was stabilized by the formation of dopant-oxygen vacancy (RE^{III}-O_V) clusters which led to a reduction in availability of the interstitial lattice sites (Figure 1) required for the incorporation of O_I during oxidation.

More relevant to the present discussion is the question of under what redox conditions does oxidation of UO_2 lead to its dissolution? Figure 13 compares the dissolution charges (extent of dissolution measured electrochemically in voltammetric experiments) (Liu et al. 2017a) for a UO_2 specimen close to stoichiometric ($UO_{2.002}$), 1.5 at% SIMFUEL, and two RE^{III}-doped UO_2 specimens with stoichiometric compositions.

For $UO_{2.002}$, minor dissolution commenced at potentials as low as -0.7 V (vs SCE), which is well below the thermodynamic threshold for the oxidation of UO_2 (~ -0.4 V vs SCE). Current sensing atomic force microscopy (CS-AFM) indicates this could be due to the presence of non-stoichiometric surface locations in the vicinity of the grain boundaries (Liu et al. 2017a) consistent with the claims of Rudnicki et al. (1994) based on photothermal deflection spectroscopic measurements. This influence of non-stoichiometry is discussed in more detail in Section 5.7. The extent of dissolution (Figure 14) decreased in the order

$$UO_{2.002} > SIMFUEL > Gd\text{-}UO_2 \sim Dy\text{-}UO_2$$
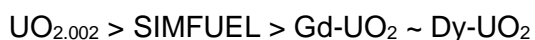
demonstrating the influence of RE^{III}-doping in decreasing the reactivity of the UO_2 surface.

Raman spectroscopy has been used to characterize the influence of RE-doping on the structure of UO_2 (Figure 14). These spectra show two key features: (i) a peak at ~ 445 cm^{-1} assigned to the symmetric O-U^{IV} stretching mode in the UO_2 fluorite lattice; and (ii) a broad band between 500 and 700 cm^{-1} attributed to lattice distortions caused by doping. The spectrum for $UO_{2.002}$ is not shown since only the 445 cm^{-1} peak is exhibited by the non-doped undisturbed lattice. As

shown, the region between 500 and 700 cm^{-1} can be deconvoluted into three contributions at 540 cm^{-1}, 570 cm^{-1} and 640 cm^{-1}. The peak at 570 cm^{-1} has been shown to be independent of the doping level in a series of SIMFUELs (He et al. 2007) and is associated with the undisturbed fluorite structure (He and Shoesmith 2010). The peak at 540 cm^{-1} can be attributed to the creation of O_V (Razdan and Shoesmith 2014a) consistent with the observations of Desgranges et al. (2012a) on Nd^{III}-doped UO$_2$, who attributed a peak at this wavenumber to a local phonon mode associated with O_V-induced lattice distortions. The presence of local structural disorder accompanied by the formation of U^V and the formation of O_V has been confirmed by XRD and X-ray absorption spectroscopy studies (Elorrieta et al. 2016; Herrero et al. 2020). Although performed on Nd-doped UO$_2$ it was noted in this last study that charge compensation mechanisms do not depend on the chemical nature of the dopant. The peak at 640 cm^{-1}, present only in the SIMFUEL, has been assigned to a Zr-O$_8$-type complex, this material being the only one containing Zr (Li et al. 2011; Garcia et al. 2004). Recent experimental and computational studies support this assignment (Lee et al. 2019).
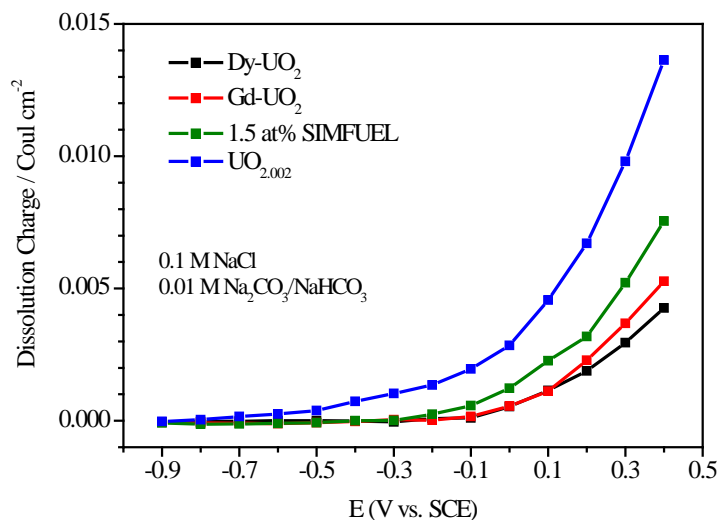
Figure 13: Dissolution Charges Calculated for Four UO$_2$ Materials from Voltammograms Recorded in 0.1 mol/L NaCl Solution Containing 0.01 mol/L [CO$_3$]$_{tot}$. Dy-UO$_2$ (12.9 wt% Dy$_2$O$_3$); Gd-UO$_2$ (6.0 wt% Gd$_2$O$_3$); 1.5 at% SIMFUEL; Undoped UO$_{2.002}$

Based on the increasing prominence of the 540 cm^{-1} peak compared to the 445 cm^{-1} peak as the RE^{III}-doping level increased and the presence of the 640 cm^{-1} peak in the Zr-containing SIMFUEL, two lattice-stabilizing features due to in-reactor fission can be claimed: (i) the formation of RE^{III}-O_V clusters decreases the availability of the vacancies required to accommodate the injection of O_I (Figure 1) necessary for the oxidation to occur; and (ii) a stabilizing decrease in the lattice parameter due to the Zr content, Zr^{IV} having a significantly smaller ionic radius then U^{IV}.
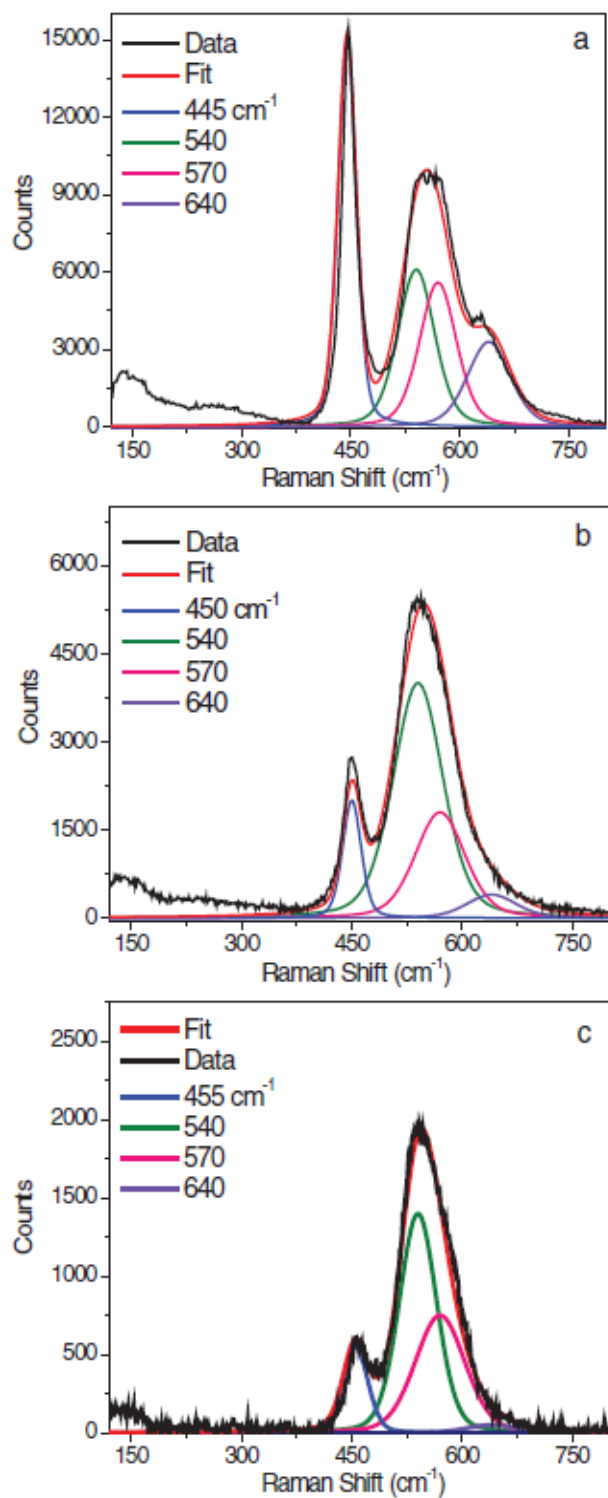
Figure 14: Raman Spectra Recorded on (a) 1.5 at% SIMFUEL; (b) Gd (6%)-doped UO₂; (c) Dy (12.9%)-doped UO₂

The inhibiting influence of RE[III]-doping on the corrosion of UO_2 was observed in early chemical dissolution studies. Oversby (1999) observed a decrease in corrosion rate by a factor of 15 for SIMFUELs, which contain a variety of dopants to simulate fission products (Section 5.3), and more recently by Casella et al. (2016) who found a decrease in corrosion rate of approximately an order of magnitude for Gd-doped UO_2 (0 to 4 wt% Gd_2O_3) at room temperature. At higher temperatures and dissolved $[O_2]$, the latter study found an even larger difference in corrosion rates between doped and undoped UO_2. Using doping levels from 0 to 8 wt%, Barreiro-Fidalgo and Jonsson (2019) observed a similar influence with the discrepancy in U^{VI} dissolution between undoped and doped UO_2 particularly marked at the highest (8 wt%) doping level. This influence was much more marked than that observed in a series of electrochemical experiments which showed only a minor influence in dissolution currents for $U_{1-y}Gd_yO_2$ over the range $0 \leq y \leq 0.1$ (Liu et al. 2017c).

By comparing the amounts of U^{VI} dissolved to the amounts of H_2O_2 consumed, Barreiro-Fidalgo and Jonsson (2019) demonstrated that, while the effect of Gd-doping on dissolution is very marked, its influence on the consumption of the H_2O_2 oxidant used is much less marked. Clearly, while suppressed slightly, the consumption of H_2O_2 by decomposition to O_2 and H_2O (discussed in Section 5.10) still occurs. A similar ability of Zr-doping to stabilize the UO_2 matrix against dissolution while catalyzing H_2O_2 decomposition has also been observed (Kumagai et al. 2017).

5.7   Non-stoichiometry

As noted in section 3, the approximate change in fuel stoichiometry for CANDU fuel has been calculated to range from $UO_{2.001}$ to $UO_{2.007}$ while the higher burnup LWR/BWR fuels exhibit only marginal oxidation.. As indicated in Figure 1, the face centered cubic UO_2 lattice contains a large number of octahedral vacant sites, which gives the lattice the ability to accommodate large amounts of O_I to form hyperstoichiometric $U^{IV}_{1-2x}U^V_{2x}O_{2+x}$. Incorporation of O occurs readily since the energy of formation of an O_I is negative (Crocombette et al. 2001; Freyss et al. 2005; Gupta et al. 2007; Geng et al. 2008; Nerikar et al. 2009). This, and the ability of U to form multiple oxidation states (U^{IV}, U^V, U^{VI}), allows the formation of a complex family of binary metal oxides within the range from UO_2 to U_3O_7 (Conradson et al. 2004). As noted above, this increases the electrical conductivity and provides donor-acceptor relay sites in the surface of the oxide which can catalyze oxidant reduction reactions (Section 5.9).

In CANDU fuel the stoichiometry can be up to 2.007 while for LWR fuel it is lower (Section 3). By studying a range of stoichiometries that extend to higher values, three aspects of the corrosion process can be investigated: (i) the composition (UO_{2+x}) at which the surface becomes unstable and susceptible to dissolution can be identified (this Section); (ii) the influence of surface composition on the kinetics of the cathodic reactions supporting corrosion can be determined (Section 5.9); and (iii) the importance of surface composition on the kinetics of radiolytically-produced H_2O_2 decomposition can be evaluated (Section 5.10).

The changes in the properties of the oxide, and their influence on the reactivity of UO_2, have been characterized by Raman spectroscopy using a specimen with a nominal stoichiometry of $UO_{2.1}$ (He and Shoesmith 2010). Figure 15 shows the surface of this specimen exhibits four distinct features which can be distinguished according to the relationship between their topography and composition. The Raman spectra recorded on such locations, Figure 16, show that the relative decrease in intensity of the peak at 445 cm^{-1} (indicative of the undisturbed

fluorite lattice) is accompanied by a relative increase in the peaks within the band between 500 and 700 cm^{-1} (indicative of the increasingly disturbed lattice as non-stoichiometry increases). A small peak at 155 cm^{-1} (indicating of the onset of tetragonal lattice distortions) is also observed at higher degrees of non-stoichiometry.
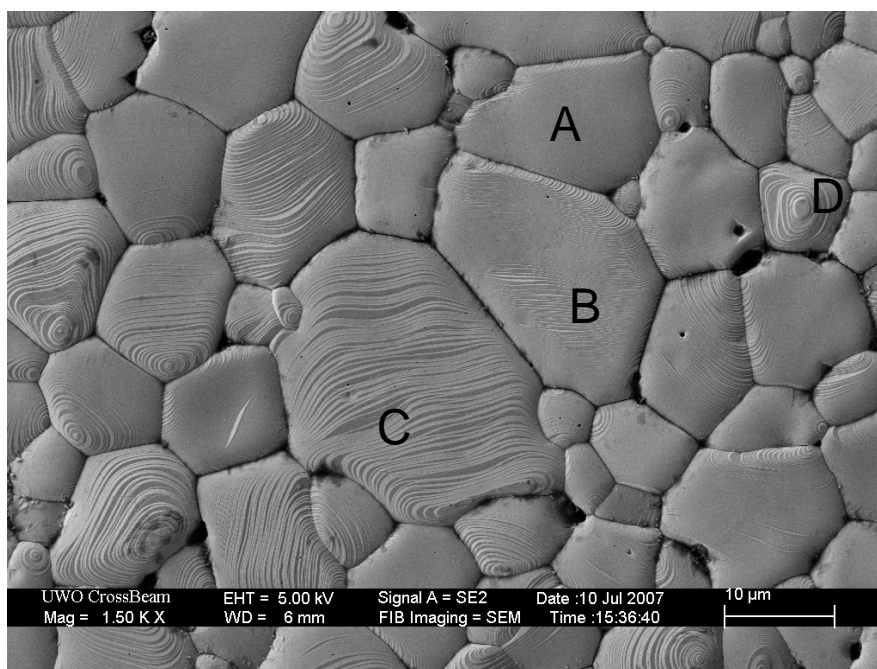
Figure 15: SEM Image of a Typical Surface Morphology Observed on a Uranium Dioxide Specimen with a Nominal Stoichiometry of UO$_{2.1}$. (A) A Smooth Flat Grain with an Approximate O/U Ratio 2.01; (B) A Grain with a Very Shallow Stepped Pattern with a Slightly Hyperstoichiometric Composition of ~ 2.15; (C) A Grain with a Pronounced Stepped Pattern of Ridges Oriented Horizontally Along the X-Y Plain with a Composition of ~ 2.22; (D) A Highly Non-Stoichiometric Spiral-like Grain with a Composition of ~ 2.31

An extensive series of Raman spot analyses and an accompanying XRD analysis yielded a relationship between the various Raman peaks and their connection to lattice composition and structure. Interpretation of these changes (He and Shoesmith 2010) are indicated in Figure 17:

- For relatively low degrees of non-stoichiometry, the number of randomly distributed O_I increases.

- Beyond x ~ 0.05, further increases in non-stoichiometry lead to the association of defects into clusters.

- For a sufficiently high degree of non-stoichiometry (> 0.15), the generation of large cuboctahedral clusters leads to a major loss of cubic symmetry with the observance of a band at 155 cm^{-1} indicating the onset of a cubic to tetragonal structural transition.

Figure 16: Raman Spectra Recorded on the Four Types of Grains (A) to (D) Shown and Described in Figure 14. The O/U Ratios Are ~2.01 (A), ~2.15 (B), ~2.22 (C), ~2.31 (D)

The cuboctahedral cluster is the most densely packed defect cluster which minimizes the damage to the UO_2 lattice induced by the incorporation of excess O by optimizing the spatial distribution of vacancies and interstitials (Bevan et al. 1986; Garrido et al. 2003; Willis 1987). These observations are consistent with published literature (Bevan et al. 1986; Elorieta et al. 2016; Brincat et al. 2015; Desgranges et al. 2016). As the degree of non-stoichiometry is increased, oxidation of the surface progresses to much deeper levels. This is clearly demonstrated in a series of voltammetric experiments on UO_{2+x} specimens with nominal compositions of $UO_{2.002}$, $UO_{2.011}$, $UO_{2.05}$ and $UO_{2.1}$. These specimens have been extensively characterized (He and Shoesmith 2010; He et al. 2009a, 2009b, 2010; He 2010) and shown to range from a specimen almost uniformly stoichiometric ($UO_{2.002}$) to one ($UO_{2.1}$) comprised of individual grains ranging from stoichiometric to extremely non-stoichiometric (~$UO_{2.32}$), as shown in Figure 15.

Figure 18 shows voltammograms recorded on these four specimens with anodic currents indicating the extent of oxidation on the forward potential scan (from negative to positive potentials) and cathodic currents the extent of reduction of the anodically oxidized surface on the reverse potential scan.

Figure 17: The Relationships between the Intensities of the Band at 445 cm⁻¹ (T₂g) and the Bands at 1150 cm⁻¹ and 155 cm⁻¹ Based on Raman Spot Analyses. The Points A-D Show Spectra Recorded at Locations Similar to Those Labelled in Figure 15. The Vertical Lines Indicate the Transitions between Defect Structures. The Compositions Indicate the Degree of Non-stoichiometry at Which the Transitions Occur. The Statements Beneath the Figure indicate the Lattice Features which are Changing as the T₂g Peak Intensity Decreases.
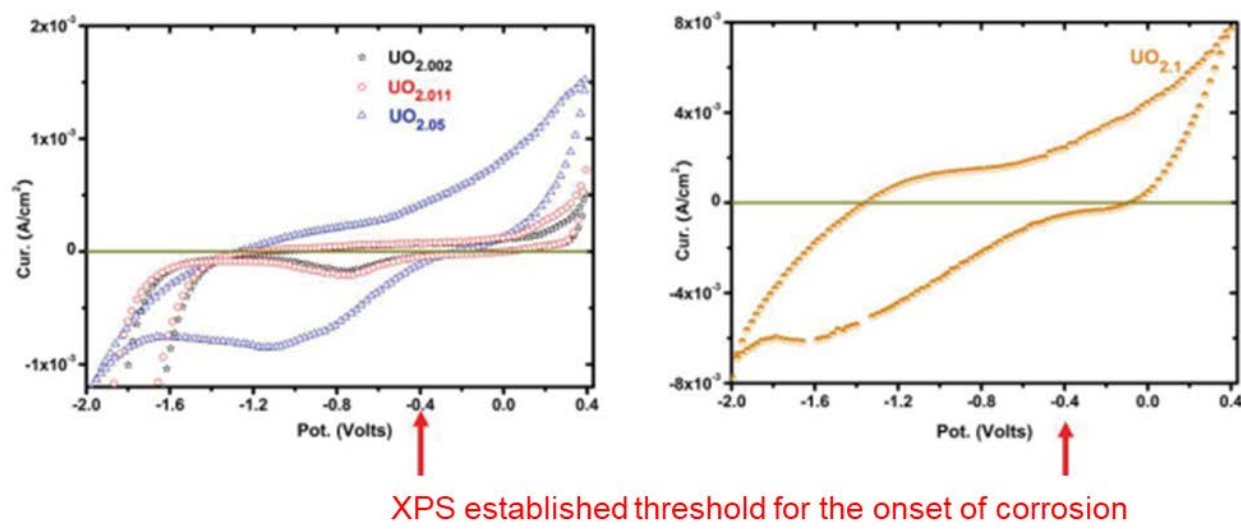
Figure 18: Voltammograms Recorded on Four Hyperstoichiometric Electrodes in 0.1 mol/L NaCl Solution (pH 9.5) at A Scan Rate of 5 mV/s. The Threshold is that Established for the Onset of Oxidation (Figure 13)

For the two specimens closest to stoichiometric, anodic oxidation currents were low with the reduction current peak (between -0.7 V and -0.9 V) indicating only a thin oxide surface layer was formed on the forward scan. The very low currents ($UO_{2.002}$, $UO_{2.011}$) recorded at potentials below the threshold, indicate minimal sub-thermodynamic oxidation as expected and are consistent with Raman spectroscopic measurements (He and Shoesmith 2010; He et al. 2009b, 2010). As the degree of non-stoichiometry increases ($UO_{2.05}$, $UO_{2.1}$), the anodic current both below and above the threshold increases markedly, indicating the facile and more extensive oxidation of non-stoichiometric regions of the surface with the large reduction current on the reverse scan confirming the formation (on the forward scan) of a much more extensively oxidized surface. A combination of SEM and SECM measurements confirm that oxidation occurs preferentially on non-stoichiometric grains (He et al. 2009a, 2009b, 2010).

This influence of surface stoichiometry can be appreciated by reconsidering the results in Figure 13 for the Dy-UO_2 specimen. These experiments were conducted in carbonate-containing solutions to stimulate dissolution rather than the retention of U^{VI} in alteration phases on the UO_2 surface, as discussed in more detail below (Section 5.11). This procedure enabled XPS analyses of the surface to detect changes in composition in the $U^{IV}_{1-2x}U^{V}_{2x}O_{2+x}$ layer unobscured by the presence of U^{VI} deposits (Figure 19). Over the potential range from -0.2 V (vs SCE) to 0.1 V (vs SCE), the extent of surface oxidation increases markedly, as indicated by the more rapid increase in U^V content with potential, with the results in Figure 13 showing this increase is accompanied by the onset of dissolution. Since the surface content of U^{VI} changed only marginally, this enhanced oxidation can be attributed to the thickening of the $U^{IV}_{1-2x}U^{V}_{2x}O_{2+x}$ layer.

This change occurred at a surface composition of ~ $U^{IV}_{0.7}U^{V}_{0.3}O_{2.15}$, a composition around which Raman spectroscopy first detects the onset of the distortion of the cubic lattice to a tetragonal structure (Figure 17) (i.e., the appearance of the band at 155 cm^{-1}) (He and Shoesmith 2010). This is consistent with SECM measurements which show that, beyond an intermediate composition in this range, the rate and depth of anodic oxidation increased markedly (He et al.

2009b). These coincidences, and their consistency with the phase transformations occurring during oxidation, demonstrate that it is the onset of tetragonal distortions of the cubic lattice which leads to dissolution. Raman spectroscopy (He and Shoesmith 2010) demonstrates that this transformation involves a switch from shallow oxidation involving randomly distributed O_I ions to deeper oxidation involving lattice distortions and the formation of cuboctahedral clusters. An attempt to illustrate this change is shown in Figure 20.

Dissolution experiments performed on stoichiometric UO_2 and $UO_{2.3}$ in bicarbonate solutions containing H_2O_2 are consistent with this analysis (Kumagai et al. 2019). The release of U^{VI} from stoichiometric UO_2 was initially significantly slower than from the non-stoichiometric $UO_{2.3}$ despite the more rapid consumption of H_2O_2 on the UO_2 surface. These observations are consistent with the need to oxidize the UO_2 surface to a threshold composition ($UO_{2.15}$) beyond which tetragonal lattice distortions lead to dissolution. By contrast the $UO_{2.3}$ surface, with a composition ($U^{IV}_{0.7}U^{V}_{0.3}O_{2.15}$) already beyond the threshold, would immediately experience dissolution. The more rapid consumption of H_2O_2 on UO_2 despite the lack of dissolution can then be attributed to the catalyzed decomposition of H_2O_2 on the $U^{IV}_{1-2x}U^{V}_{2x}O_{2+x}$ ($x \leq 0.15$) as discussed below in Section 5.10.
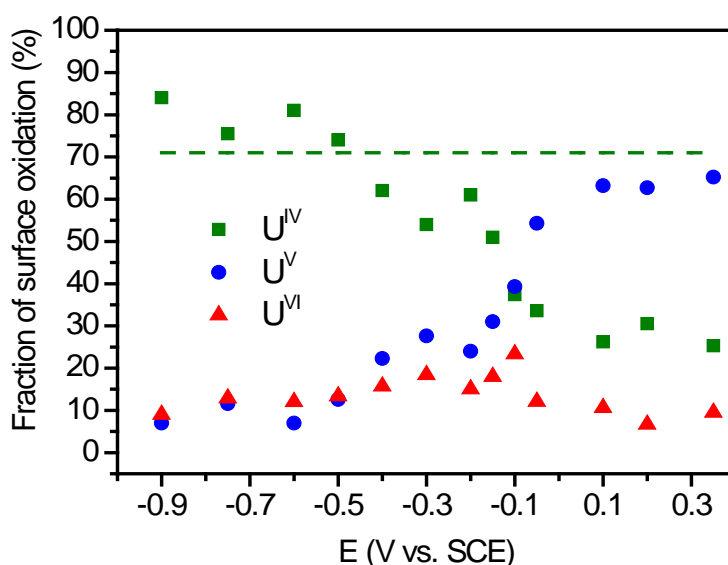
Figure 19: Relative Fractions of U Oxidation States as a Function of Applied Potential, Recorded on Dy-UO$_2$ (12.9 wt% Dy) after 1 hour of Oxidation in 0.1 mol/L NaCl + 0.05 mol/L [CO$_3$]$_{tot}$ Solution. The dashed line shows the fraction of U^{IV} recorded on a freshly polished Dy-UO$_2$ Surface

Measurements of the extent of anodic oxidation as a function of electrochemical potential showed that, for $U^{IV}O_2$ nominally close to stoichiometric ($UO_{2.002}$), minor dissolution commenced at potentials as low as -0.7 V (vs SCE) (Figure 13). Current-sensing atomic force microscopy (CS-AFM) demonstrates this could be attributable to the presence surface locations in the vicinity of the grain boundaries with a stoichiometry already beyond the threshold of $UO_{2.15}$ (Liu et al. 2017a).

$$U^{IV}O_2 \longrightarrow U^{IV}_{0.7}U^{V}_{0.3}O_{2.15} \longrightarrow U^{IV}_{0.5}U^{V}_{0.5}O_{2.25}$$

Randomly distributed O_I defects with limited diffusivity into the matrix

Scenario of cuboctahedral clusters facilitating enhanced diffusivity and leading to dissolution
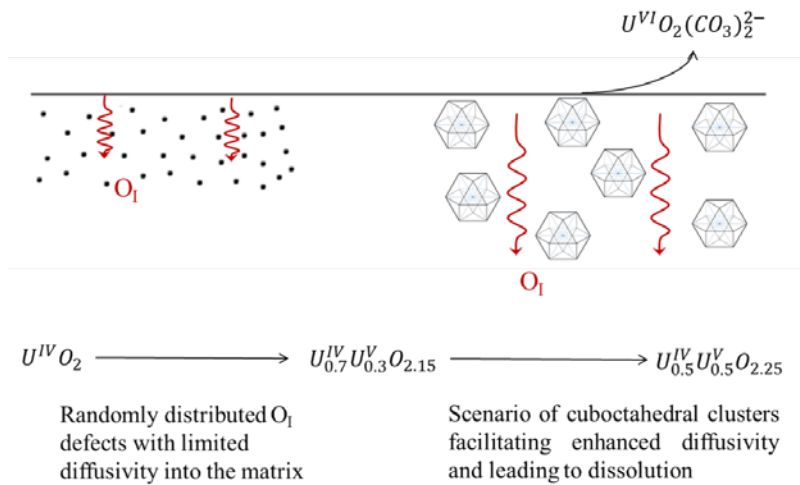
Figure 20: Schematic Illustrating the Influence of Major Tetragonal Distortions Leading to the Extensive Formation of Cuboctahedral Clusters and the Onset of Dissolution

5.8   Groundwater Species

The composition of the groundwater entering a failed container will depend on the type of host rock and the interaction between groundwater and the surrounding clay as DGR conditions evolve with time. Groundwater compositions from Canadian sedimentary rocks (e.g., Michigan Basin) and crystalline rocks have been measured (Garisto 2017; NWMO 2017, 2018). The reference groundwater compositions are noted in Hall et al. (2021). Both chemical analyses and the application of speciation codes and ion-exchange expressions have been used to determine the influence of evolving DGR conditions on the groundwater composition (King et al. 2017). The effect of bentonite clay and the container on the groundwater composition was also investigated (Colàs et al. 2021, 2022). Based on these studies, the key groundwater species likely to influence fuel dissolution are the anions Cl^-, SO_4^{2-} and HCO_3^- and the cations, H^+, Na^+ and Ca^{2+}.

Within the pH range anticipated in a DGR (~5.5 to 9.5), the solubility of uranium is extremely low in the U^{IV} state and at a minimum for the oxidized U^{VI} state (Figure 3). Measured corrosion rates in an aerated ClO_4^- solution (i.e., a solution containing no complexants for $U^{VI}O_2^{2+}$) (Torrero et al. 1997; Thomas and Till 1984; Sunder et al. 1991a; Shoesmith 2000) show only a slight increase in corrosion rate at the acidic end of the pH range (noted above) with almost no influence within the anticipated pH range in the DGR. Based on the results of Torrero et al. (1997), corrosion rates for the pH range 3 to 6.7 could be fitted to the rate (R) equation,

$$R \;=\; 3.5(\pm 0.8) \times 10^{-8}[H^+]^{0.37\pm 0.01}[O_2]^{0.31\pm 0.02} \tag{8}$$

The partial reaction order with respect to $[H^+]$ was interpreted as an indication that complexed surface species were involved with the fractional reaction orders indicating a competition for key surface sites between H^+ and O_2.

Studies on the effect of pH on the anodic dissolution of UO_2 (Santos et al. 2006c) confirm the originally proposed mechanism (Nicol and Needes 1973, 1975),

$$U^{IV}O_2 + H_2O \rightarrow (U^VO_2OH)_{ads} + H^+ + e^- \qquad (9)$$

$$(U^VO_2OH)_{ads} + H_2O \rightarrow (U^{VI}O_2(OH)_2)_{ads} + H^+ + e^- \qquad (10)$$

$$(U^{VI}O_2(OH)_2)_{ads} + 2H^+ \rightarrow U^{VI}O_2^{2+} + 2H_2O \qquad (11)$$
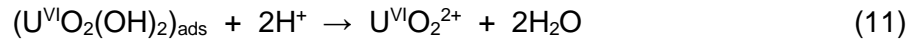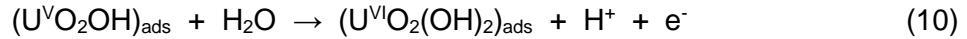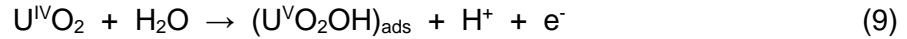
with the U^V intermediate (identified by XPS) present as a surface adsorbed species not as an ion incorporated into a $U^{IV}_{1-2x}U^V_{2x}O_{2+x}$ surface layer. Based on electrochemical measurements, this transition from a surface to an adsorbed layer occurs around pH ~ 5; i.e., the pH below which the measured solubility begins to increase (Figure 3).

In more alkaline solutions (pH $\geq$ 10) (in the absence of complexing anions) the mechanism of surface oxidation and dissolution is the same as in neutral solutions, but the $U^{IV}_{1-2x}U^V_{2x}O_{2+x}$ layer becomes thicker and the dissolution rate increases due to stabilization of soluble U^{VI} by hydrolysis

$$U^{VI}O_2^{2+} + xOH^- \rightarrow U^{VI}O_2(OH)_x^{(2-x)+} \qquad (12)$$
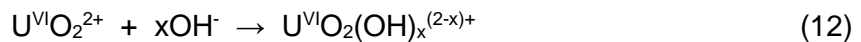
Chemical analyses under aerated conditions confirm this increase in corrosion rate (Pierce et al. 2005).

Since $U^{VI}O_2^{2+}$ is readily hydrolyzed (reaction 12), there is a possibility that acidic conditions could form in unbuffered groundwater within flaws and cracks in the spent fuel or in pores in corrosion product deposits, as illustrated schematically in Figure 21.
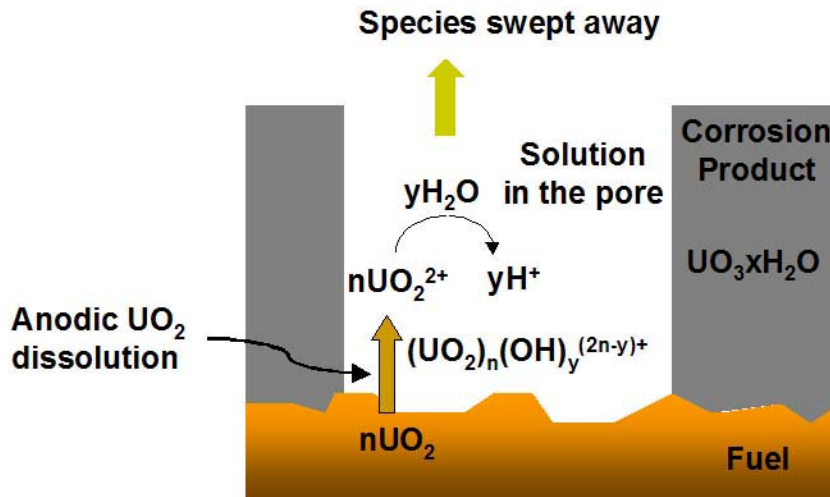
Figure 21: Illustration Showing the Electrochemical, Chemical and Transport Processes that Could Occur in Unbuffered Groundwater Either within the Pores in a Corrosion Product Deposit (Shown) or within Flaws and Cracks in the Spent Fuel Surface (Not Shown)

For such a situation to arise, anodes (shown in Figure 21) and cathodes (the site at which oxidant reduction occurs (not shown in Figure 22)) would have to be separated as discussed in detail elsewhere (Cheong et al. 2007; Qin et al. 2014). Such a separation is unlikely and model calculations (Cheong et al. 2007; Qin et al. 2014) show that even for deep pores or fractures, extremely oxidizing conditions beyond those achievable in a DGR would be required to suppress the pH leading to a local acceleration in corrosion rate.

The three dominant anions in anticipated groundwaters are Cl^-, SO_4^{2-} and HCO_3^-. Despite its anticipated high concentration, Cl^- has a negligible impact on either the solubility of $U^{VI}O_2^{2+}$ or the kinetics of fuel corrosion. This is consistent with the inability of Cl^- to complex the $U^{VI}O_2^{2+}$ cation (Grenthe et al. 1992; Guillamont et al. 2020; Lemire and Tremaine 1980; Lemire and Garisto 1989).

The effect of SO_4^{2-} has been shown, using electrochemical experiments (Nicol and Needes 1973; Ofori 2008) to be limited to pH ≤ 3 and to involve surface adsorbed U^V species $(U^VO_2HSO_4)_{ads}$. Since pH values this acidic do not appear achievable under DGR conditions, SO_4^{2-} is unlikely to exert any significant effect on fuel corrosion and radionuclide release.

While the HCO_3^- content of the groundwater is expected to be low and controlled by the solubility of carbonate minerals (e.g., calcite ($CaCO_3$)) in the clay surrounding the container (King et al. 2017) and in the host rock, its ability to complex $U^{VI}O_2^{2+}$ (Grenthe et al. 1992; Guillamont et al. 2020; Lemire and Tremaine 1980; Lemire and Garisto 1989) makes it the most likely anion to influence the fuel corrosion process. As a consequence, its influence has been extensively studied (Nicol and Needes 1973; Ofori 2008; Shoesmith et al. 1983, 1984; de Pablo et al. 1996, 1999; Hossain et al. 2006; Goldik et al. 2006a; Luht 1998; Sunder et al. 1992; Ilin et al. 2001; Cobos et al. 2003; Keech et al. 2011).

Figure 22 (Liu et al. 2017a) shows a series of voltammograms recorded on Dy-doped UO_2. A number of features are instructive. The potential at which anodic dissolution commences is -0.2 V (vs SCE) when tetragonal lattice distortions first occur (Section 5.2). This onset is independent of $[CO_3]_{tot}$ indicating the lattice is destabilized by the strength of oxidation not the presence of HCO_3^-. For more positive applied potentials, the current becomes dependent on $[CO_3]_{tot}$ consistent with the acceleration of dissolution by HCO_3^-. The two small reduction peaks observed on the reverse scan show that a small amount of the anodic current is consumed in the formation of surface films with current peak 1 attributed to reduction of the $U^{IV}_{1-2x}U^V_{2x}O_{2+x}$ layer and peak 2 to the reduction of $U^{VI}O_3 \cdot yH_2O$ or $U^{VI}O_2CO_3$ formed at the oxide/solution interface (Liu et al. 2017a). The charge associated with these films is reduced as the $[CO_3]_{tot}$ is increased confirming that, when a sufficient concentration of HCO_3^- is present, deposition of U^{VI} as $U^{VI}O_3 \cdot yH_2O$ or $U^{VI}O_2CO_3$ is prevented and the $U^{IV}_{1-2x}U^V_{2x}O_{2+x}$ surface layer is thinned.

The results of a more extensive study on SIMFUELs are shown in Figure 23 and Figure 24 (Keech et al. 2011). The slopes of the Tafel plots (log j vs E) in the potential range 150 mV to 250 mV are ~ 120 mV per decade change in current indicating the rate of the anodic dissolution reaction is controlled by the rate of the first electron transfer step; i.e., the oxidation of U^{IV} to U^V. The significantly larger Tafel slopes and lower dissolution currents at low $[CO_3]_{tot}$ are consistent with the presence of a surface U^{VI} layer which partially inhibits dissolution, as is the tendency of the current to become independent of potential at more positive potential values.
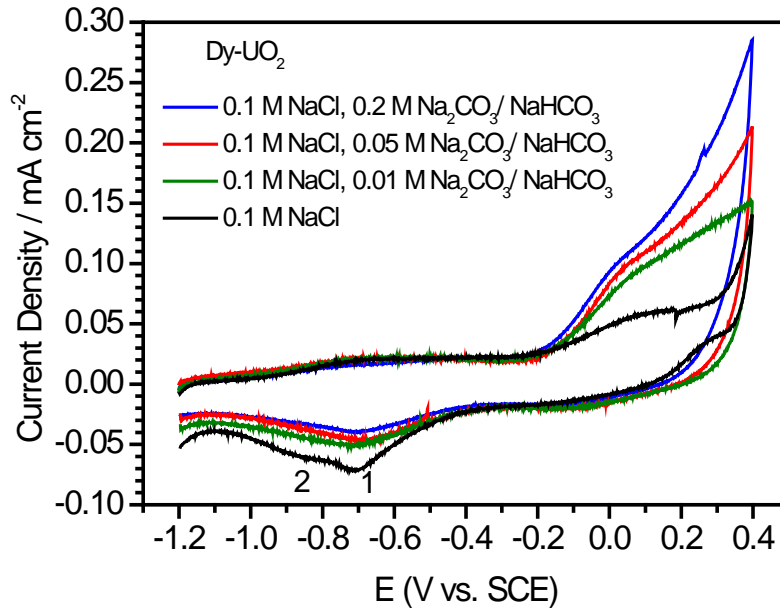
Figure 22: Cyclic Voltammograms Recorded on a Rotating (16.7 Hz) Dy-UO₂ (12.9 wt%) Electrode in Ar-purged 0.1 mol/L NaCl Solution Containing Various [CO₃]ₜₒₜ at a Scan Rate of 10 mV/s

Figure 24 shows the reaction order (m) with respect to $[CO_3]_{tot}$ confirming that, at low applied potentials which approach natural corrosion conditions, HCO_3^- is not involved in determining the kinetics consistent with the Tafel behaviour and confirming that the initial oxidation step is rate-determining. Electrochemical impedance spectroscopy (EIS) measurements confirm the overall reaction proceeds via adsorbed U^V and U^{VI} intermediates,

$$U^{IV}O_2 + HCO_3^- \rightarrow (U^VO_2HCO_3)_{ads} + e^- \qquad (13)$$

$$(U^VO_2HCO_3)_{ads} + OH^- \rightarrow (U^{VI}O_2CO_3)_{ads} + H_2O + e^- \qquad (14)$$

$$(U^{VI}O_2CO_3)_{ads} + HCO_3^- \rightarrow U^{VI}O_2(CO_3)_2^{2-} + H^+ \qquad (15)$$
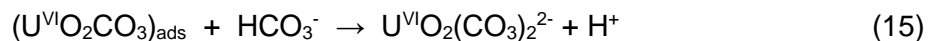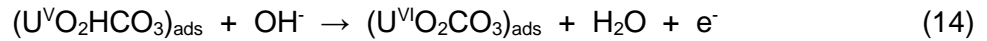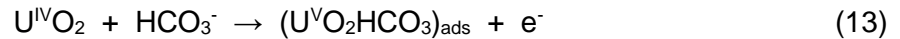
with the first electron transfer step (reaction 13) controlling the corrosion rate at low potentials and the chemical dissolution step (reaction 15) controlling the rate at high potentials. A similar switch from control by electron transfer to control by chemical dissolution depending on the $[H_2O_2]$ and $[CO_3]_{tot}$ has been observed in chemical (open circuit) experiments (Hossain et al. 2006; Sundin et al. 2013), although the kinetics were complicated by studtite formation (discussed below in Section 5.11). Under DGR conditions, when oxidant concentrations will be low, reaction 13 will be the slow anodic step with the corrosion rate dictated by the kinetics of the oxidant reduction reaction.
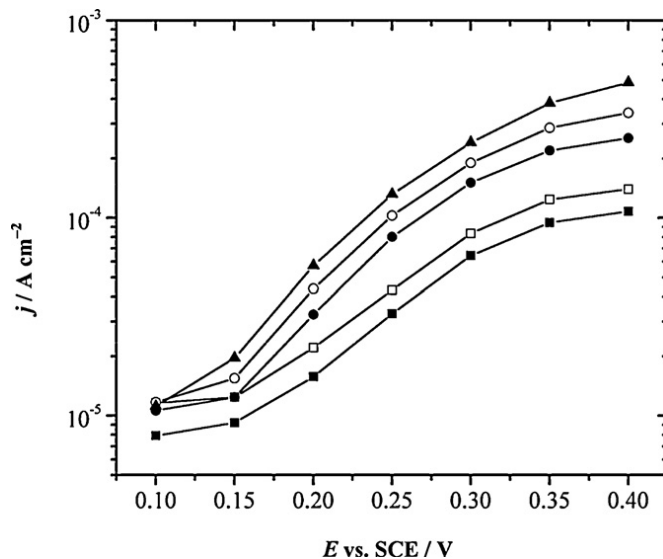
Figure 23: Tafel Plots for the Oxidation/Dissolution of 1.5 at% SIMFUEL in 0.1 mol/L NaCl Solution Containing Various [CO$_3$]$_{tot}$ (pH = 9.7). The Current (j) Increases As the [CO$_3$]$_{tot}$ Increases Through the Sequence 0.005 (■), 0.01 (□), 0.05 (●), 0.1 (○), 0.2 (▲) mol/L
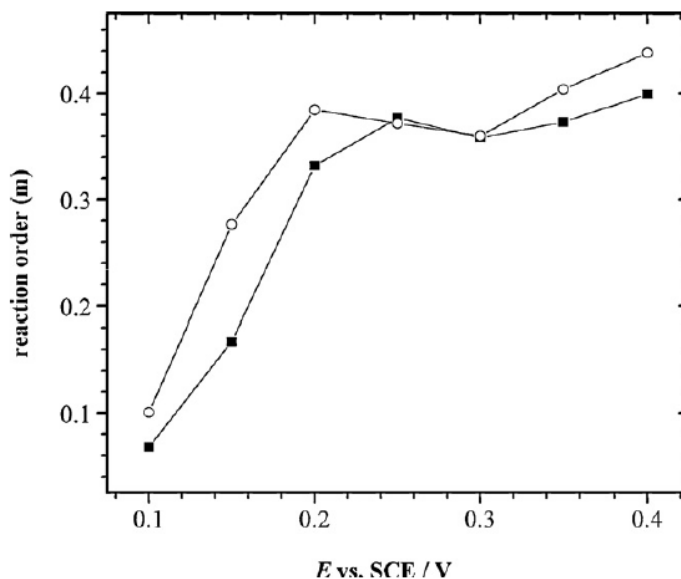
Figure 24: Reaction Orders with Respect to [CO$_3$]$_{tot}$ As a Function of Applied Potential (Calculated from the Currents in Figure 23): The second Set of Data (○) Shows Values Calculated from Electrochemical Impedance Spectroscopy Measurements

When present at a sufficiently high concentration, HCO$_3^-$ can also influence the kinetics of oxidant reduction reactions, as illustrated by the polarization curves shown in Figure 25. This makes its overall influence on the kinetics of UO$_2$ corrosion difficult to quantify. Irrespective of whether O$_2$ or H$_2$O$_2$ is the oxidant, HCO$_3^-$ can suppress the oxidant reduction rate by adsorbing and stabilizing U^V surface states thereby denying O$_2$/H$_2$O$_2$ access to the DAR (Donor-Acceptor Relay) sites which catalyze their reduction (Hocking et al. 1991, 1994; Shoesmith et al. 1996; Zhu 2018) (Section 5.9) (these sites are surface U atoms which switch oxidation state between

U^{IV} to U^V as they either accept or donate an electron). At sufficiently high [HCO$_3^-$] and [H$_2$O$_2$], it has also been proposed, but not analytically demonstrated, that U^V-peroxycarbonate species ($U^VO_2(HCO_3)(H_2O_2)$) are involved in catalyzing both the anodic and cathodic reactions (Goldik et al. 2006a).

More detailed studies (Zhu et al. 2019) also claimed dissolution was accelerated by the formation of soluble peroxycarbonate species, ($U^{VI}O_2(O_2)_x(CO_3)_y^{2-2x-2y}$). Such species have been shown to accelerate $U^{IV}O_2$ dissolution when [H$_2$O$_2$] and [CO$_3$]$_{tot}$ were higher than those commonly employed in UO$_2$/spent fuel studies (Peper et al. 2004; Goff et al. 2008).
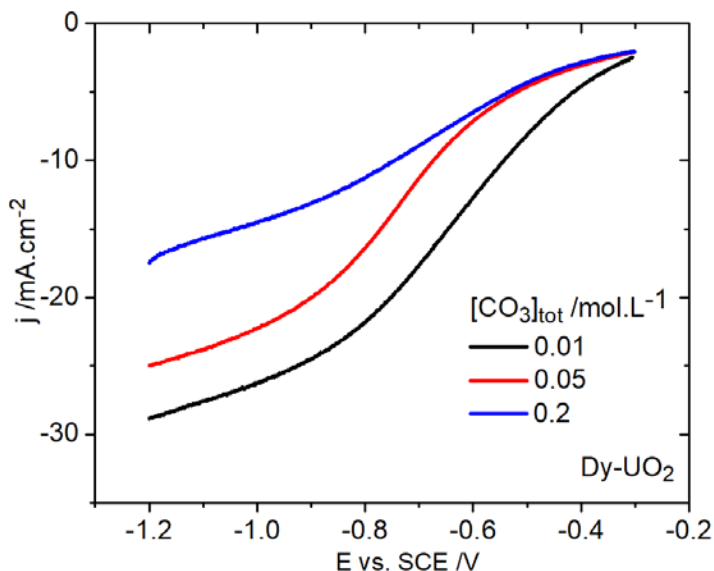
Figure 25: H$_2$O$_2$ Reduction Currents Recorded on a Dy-UO$_2$ (12.8 wt%) Electrode in Polarization Scans Recorded from -1.2 V to -0.3 V in 0.1 mol/L NaCl Solution Containing 0.02 mol/L H$_2$O$_2$ and Various [CO$_3$]$_{tot}$

Of the groundwater cations, the most likely to influence fuel dissolution is Ca^{2+} which can either inhibit corrosion by the formation of surface adsorption/secondary phase formation or enhance dissolution by the formation of ternary Ca-U^{VI}-carbonate aqueous complexes (Dong and Brooks 2006; Maia et al. 2021; Mühr-Ebert et al. 2019),

$$Ca^{2+} + U^{VI}O_2(CO_3)_3^{4-} \rightarrow CaU^{VI}O_2(CO_3)_3^{2-} \tag{16}$$

$$2Ca^{2+} + U^{VI}O_2(CO_3)_3^{4-} \rightarrow Ca_2U^{VI}O_2(CO_3)_3 \tag{17}$$
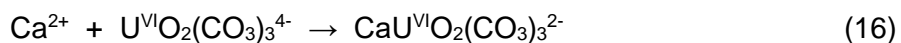
Experiments on UO$_2$ and spent fuel under oxidizing conditions in the presence of limited amounts of water (Wronkiewicz et al. 1992, 1996, 1997), and measurements of dissolution rates in single-pass flow-through experiments (Wilson and Gray 1990; Tait and Luht 1997) show a significant influence of Ca^{2+} and silicate on fuel dissolution behaviour. The effect of adding these species during an experiment was immediate (Figure 26), indicating a direct effect on the kinetics of dissolution.
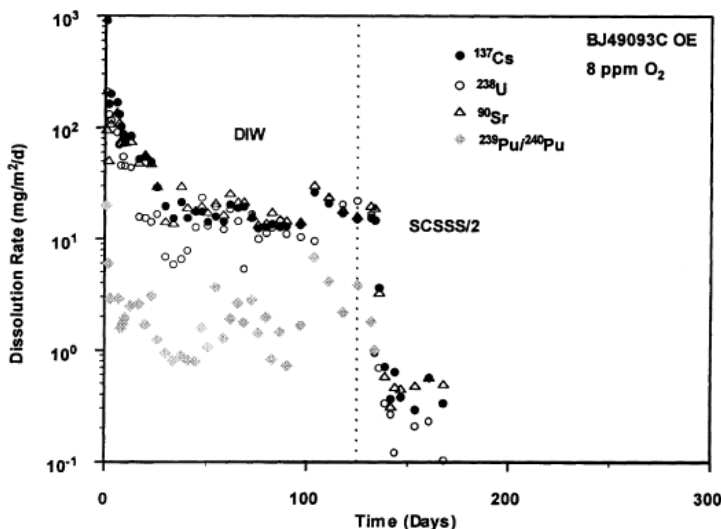
Figure 26: Corrosion Rate of Spent CANDU Fuel and Specific Radionuclide Release Rates at 25 °C in O_2-containing Distilled Deionized Water (DIW) and O_2-containing Simulated Saline Groundwater (SCSSS) Before and After the Addition of 0.185 mol/L Ca^{2+} and 0.00027 mol/L SiO_4^{4-}

U concentrations measured in flow-through experiments using UO_2 pellet fragments showed the corrosion rate was suppressed by a factor of 200 with the larger influence exerted by the silicate (Wilson and Gray 1990; Tait and Luht 1997).

Electrochemical experiments show that the replacement in solution of Na^+ by Ca^{2+} leads to a significant suppression of the anodic dissolution of UO_2 under strongly oxidizing conditions (0.25 V vs SCE) (Figure 27)(Santos et al. 2006a). Since acidification within locally occluded sites is likely at this potential, this suggests Ca^{2+} is directly involved in the displacement of protons from the anion (O^{2-}) interfacial transfer sites, which require their neutralization by H^+,

$$(O^{2-})_{lattice} + 2H^+ \rightarrow H_2O \tag{18}$$

This would be consistent with the results of an earlier study by Scott et al. (1977), who observed a significant inhibition of β-$U^{VI}O_3$ dissolution by cations, and with charge transfer theory (Vermilyea 1966, as summarized by Segall et al. 1988). For less oxidizing conditions (0.1 V vs SCE) (Santos et al. 2006a), more closely approaching those anticipated in a DGR, XPS measurements showed the dominant surface state to be U^V indicating that Ca^{2+} did not interfere with the conversion of the $U^{IV}O_2$ surface to $U^{IV}_{1-2x}U^V_{2x}O_{2+x}$. This is not surprising since the nature of the groundwater cation would not be expected to influence the injection of O^{2-} into interstitial sites in the fluorite lattice, a process accompanied by the oxidation of U^{IV} to U^V within the surface (Figure 1).

These results demonstrate that the dominant influence of Ca^{2+} is to directly suppress the ion transfer processes required for oxide dissolution to occur and are consistent with the studies of Cerrato et al. (2012). In the absence of significant concentrations of HCO_3^- in anticipated

groundwaters, the possibility of forming Ca-U^{VI}-carbonate complexes, which would accelerate dissolution, is remote.

As observed in flow-through experiments (Wilson and Gray 1990; Tait and Luht 1997), silicate was observed to suppress the anodic dissolution of $U^{IV}O_2$ in electrochemical experiments with the correlation between the amounts of U^{VI} and silicate on the $U^{IV}O_2$ surface, and the observation that H_2O is co-adsorbed, indicating silicate is incorporated into a hydrated silicate surface deposit (Santos et al. 2006b). EDS analyses of deposits formed on a SIMFUEL surface after a long period of slow electrochemical oxidation (i.e., the application of a 20 nA current for 600 h) confirm the formation of a U^{VI} silicate deposit (Figure 28) (Ofori et al. 2010). Since silicate concentrations are expected to be low in Canadian groundwaters (NWMO 2017, 2018: Hall et al. 2021) and the production of dissolved U slow, inhibition of corrosion by the formation of a U^{VI}-silicate deposit is unlikely under DGR conditions.
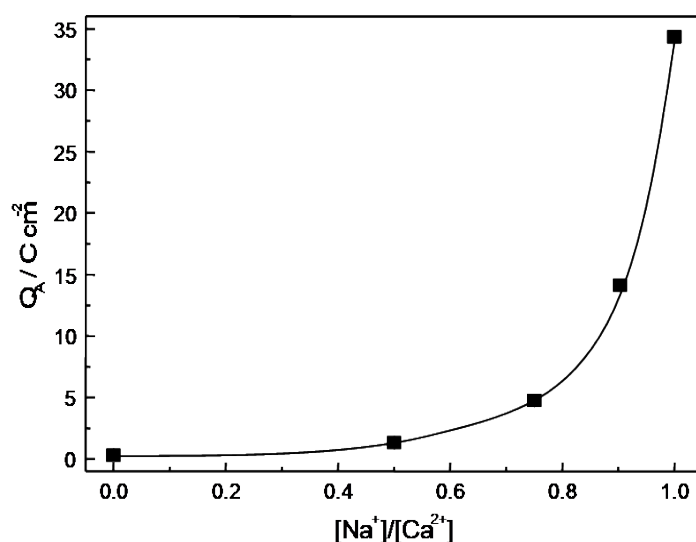
Figure 27: Anodic Dissolution Charges Measured on a 1.5 wt% SIMFUEL in a 0.1 mol/L solution (pH = 9.5) Containing Different Ratios of CaCl₂ and NaCl. The Charges Were Measured After 100 Hours of Anodic Oxidation at 0.25 V (vs SCE) and are Directly Proportional to the Number of Moles of Dissolved U

The possibility that minor groundwater species arising by contact of the fuel with the clays compacted around the container could influence fuel corrosion have also been investigated. While SH^- is expected to be the key oxidant leading to failure of the Cu container (Hall et al. 2021), its concentration will be very low and rendered insignificant by reaction with iron minerals in the environment surrounding the container vessel and by corrosion of both the steel container vessel and its Cu coating (King et al. 2020). This makes contact of the fuel with SH^- unlikely to be significant. In the unlikely chance it does, Yang et al. (2013) showed that SH^- would retard radiation-induced corrosion by scavenging radiolytic oxidants and acting as a reductant for U^{VI} species,

$$U^{VI}O_2^{2+} + SH^- \rightarrow U^{IV}O_2 + S + H^+ \tag{19}$$
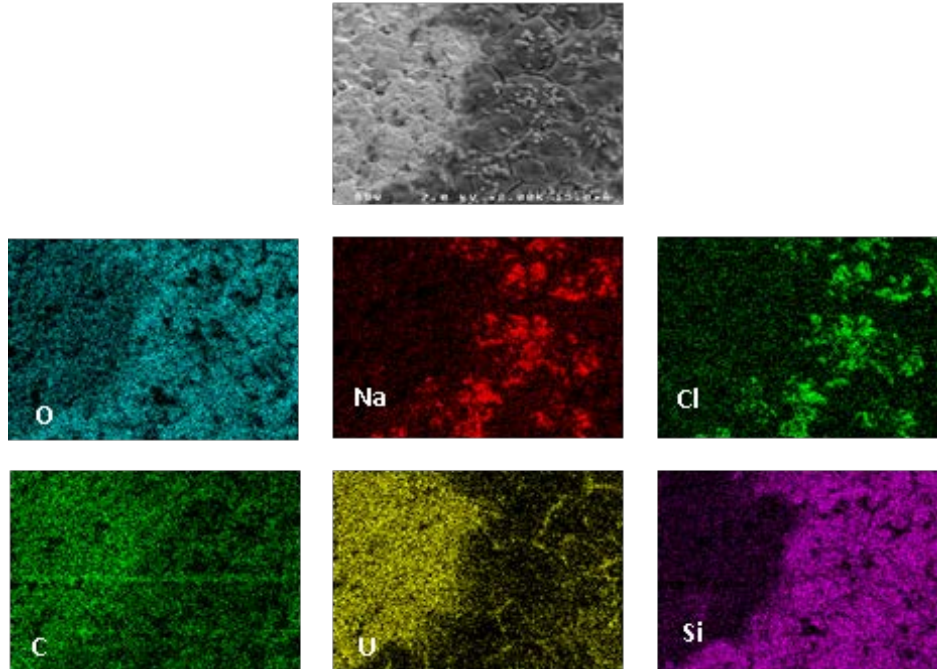
Figure 28: SEM Image and Energy Dispersive X-ray (EDS) Maps of a 1.5 at% SIMFUEL Surface Slowly Electrochemically Oxidized (at A Current of 20nA) for 600 Hours in 0.1 mol/L NaCl Solution Containing 0.1 mol/L NaSiO₃ (pH = 9.5). (The Localized Signals for Na and Cl Can be Attributed to the Presence of NaCl in the Wet Porous Deposit When the Electrode Was in the Electrochemical Cell. When the Specimen Was Removed and Placed in the Microscope, the Water Evaporated Leaving Behind NaCl)

Also, even at concentrations well in excess of those anticipated in DGR groundwaters, SH⁻ has been shown not to interfere with the ability of noble metal particles to act as catalysts for reactions involving H_2 (Section 6.2). These conclusions are consistent with studies which overwhelmingly show SH⁻ is a strong reductant for U^{VI} (Hua et al. 2006; Moyes et al. 2000; Wersin et al. 1994; Livens et al. 2004) and that U is reduced and immobilized (as $U^{IV}O_2$) by reaction with sulphate reducing bacteria (Beyenal et al. 2004).

Similarly, the radiolytic production of low molecular weight organic acids, such as formic/oxalic acids, by reactions involving the $CO_2^{\bullet -}$ radical formed by the radiolysis of HCO_3^-/CO_3^{2-}, have been shown to inhibit, not promote, fuel dissolution. This was confirmed using phthalic acid which was shown to scavenge oxidizing radicals (Barreiro-Fidalgo et al. 2014). A similar scavenging was demonstrated to occur with oxidants in bentonite clay (Sundin et al. 2013).

5.9 Potential Oxidants (Oxygen, Hydrogen Peroxide)

If container failure occurs while γ/β radiation fields are significant, fuel corrosion could be driven by both radical and molecular oxidants (Shoesmith 2000; Shoesmith et al. 1996; Sunder et al. 1992). However, while the rate constants for the reaction of radiolytic radicals with the fuel surface have been shown to be large (Ekeroth and Jonsson 2003), the steady-state radical concentrations are low and fuel corrosion would be expected to be dominated by reaction with H_2O_2 which would be present in substantially larger concentrations. If container failure is

delayed until γ/β fields are insignificant (after a few hundreds of years, Figure 10) and only α-radiolysis of H_2O is important, H_2O_2 would be the dominant oxidant. However, H_2O_2 decomposition occurs readily on oxides (Wren et al. 2005; Lin and Gurol 1998; Fu et al. 2010; Hiroki and LaVerne 2005; Lousada et al. 2012, 2013a, 2013b; 2013c; Zigah et al. 2012; Lousada and Jonsson 2010; Barreiro-Fidalgo et al. 2016) (Section 4.10) to produce the additional oxidant O_2,

$$2H_2O_2 \rightarrow O_2 + 2H_2O \tag{20}$$

which reacts over 2 orders of magnitude more slowly with UO_2 than H_2O_2 (Wren et al. 2005) and fuel corrosion could correspondingly be much slower.

The reduction of O_2 is notoriously slow due to the need to break the strong O-O bond (Hocking et al. 1991; 1994; Shoesmith et al. 1996). On UO_2, the kinetics are accelerated by oxidizing the surface to $U^{IV}_{1-2x}U^V_{2x}O_{2+x}$ (Hocking et al. 1991, 1994) which enables catalysis by mixed oxidation states (donor/acceptor relay (DAR) sites) on the oxide surface as illustrated schematically in Figure 29 (Liu et al. 2018).
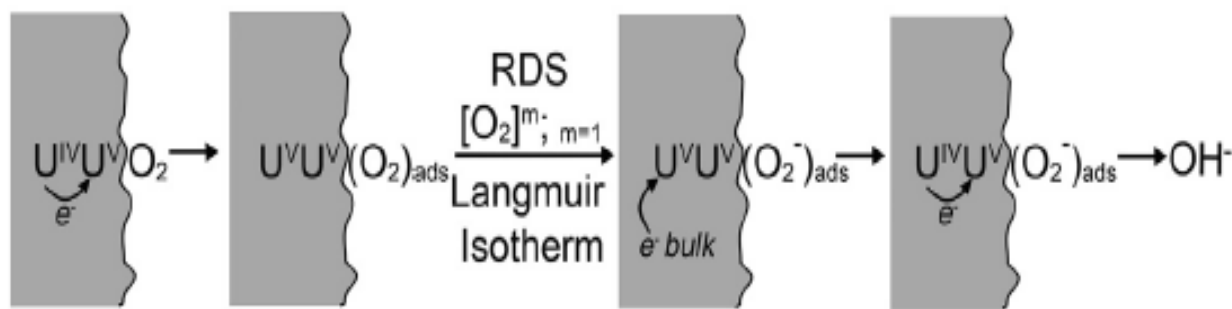
Figure 29: Reduction of O_2 at Donor-Acceptor Relay (DAR) Sites on a $U^{IV}_{1-2x}U^V_{2x}O_{2+x}$ Surface

Corrosion experiments in aerated solutions confirm that an increase in the number density of DAR sites does occur leading to a corresponding increase in O_2 reduction current in electrochemical experiments. This increased surface conductivity would be expected to lead to an enhanced corrosion rate providing the formation of insulating U^{VI} surface species is avoided. This was verified by varying the $[O_2]$ and determining the variation in corrosion rate as a function of surface composition (Shoesmith et al. 1989).

The reaction is first order with respect to $[O_2]$ and appears to initiate by O_2 adsorption under Langmuir isotherm conditions involving the interaction of the π and/or sp^3 orbitals of O_2 with partially filled U5f orbitals present in $U^{IV}_{1-2x}U^V_{2x}O_{2+x}$. For highly non-stoichiometric $U^{IV}_{1-2x}U^V_{2x}O_{2+x}$, O_2 reduction currents are suppressed with a square root dependence on $[O_2]$ and exhibit large Tafel slopes (a shallow current dependence on applied electrochemical potential) suggesting partial chemical control of the first electron transfer step. Although unproven, it is possible that the tendency of O_I to form cuboctahedral clusters may deactivate some DAR sites for O_2 reduction by isolating them from the matrix conductive network.

The O_2 reduction current is also suppressed by competition for U^V surface locations in HCO_3^-/CO_3^{2-} solutions. Since the O_2 reaction order and the Tafel slope (potential dependence of the logarithm of the reduction current) are apparently unaffected by the presence of HCO_3^-/CO_3^{2-}, the overall reduction reaction mechanism appears to be unaltered, although some H_2O_2 (a 2 electron as opposed to 4 electron O_2 reduction product) is released to solution, indicating its partial desorption from, rather than reduction on, the DAR sites (Hocking et al. 1991, 1994).

Two possible effects of in-reactor burn-up on O_2 reduction can be identified: (i) fission product doping with RE^{III} ions which will increase the number density of U^{IV}/U^V DAR sites by creating additional U^V sites; (ii) the creation of noble metal (ε) particles which contain Ru, Rh, and Pd all of which have been shown to catalyze O_2 reduction (Betteridge et al. 1997; Anastasijevic et al. 1986; Vracar et al. 1986, 1987; Martinovic et al. 1988; Kim et al. 1995). Figure 30 shows O_2 reduction currents recorded on a series of SIMFUEL electrodes in air-saturated solutions. RE^{III}-doping alone has only a marginal effect on the kinetics, but an increase in number density of ε-particles (over the simulated burn-up range 1.5 at% to 6 at%) systematically increases the rate of O_2 reduction. Thus, O_2 reduction in support of UO_2 corrosion would occur preferentially on ε-particles rather than on the UO_2 surface.

The cathodic reduction of H_2O_2 is considerably faster on UO_2 than that of O_2 (Hiskey 1980; Shoesmith 2000; Shoesmith et al. 1998) with the factor of ~ 200 consistent with the chemical evaluation of Ekeroth and Jonsson (2003). The effect of H_2O_2 on UO_2 corrosion has been extensively studied using both chemical and electrochemical methods (Sunder et al. 2004; Gimenez et al. 1996; de Pablo et al. 1996, 2001; Corbel et al. 2006; Wren et al. 2005; Hossain et al. 2006; Eary and Cathles 1983; Brown 1980; Diaz-Arocas et al. 1995; Amme 2002; Amme et al. 2002; Christensen et al. 1990; Jonsson et al. 2004; Goldik et al. 2004, 2005, 2006a, 2006b; Keech et al. 2008; Broczkowski et al. 2010; Razdan et al. 2012; Razdan and Shoesmith 2015).

This higher rate for H_2O_2 reduction can be attributed to the ability of H_2O_2 to create its own U^{IV}/U^V catalytic DAR surface sites, a reaction driven by the initial formation of surface $OH^\bullet$ radicals (Barreiro-Fidalgo et al. 2018; Maier et al. 2020; Kumagai and Jonsson 2020),

$$H_2O_2 \rightarrow 2(OH^\bullet)_{ads} \tag{21}$$

$$U^{IV} + (OH^\bullet)_{ads} \rightarrow U^V + OH^- \tag{22}$$
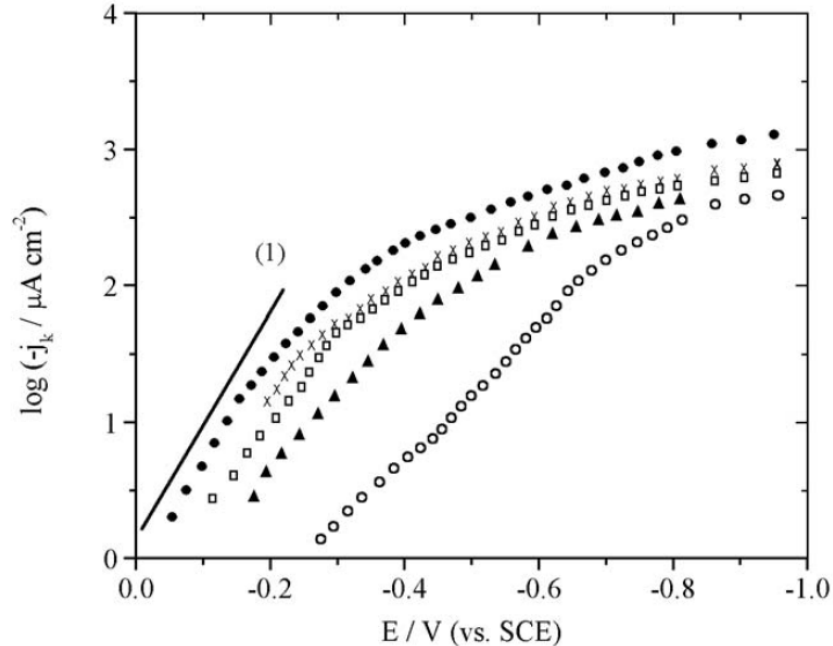
Figure 30: O₂ Reduction Currents Recorded on Various SIMFUEL Electrodes in a 0.1 mol/L NaCl (pH = 9.5) Solution Purged with Air ([O₂] = 2.5 x 10⁻⁴ mol/L): (○) Fission Product-doped UO₂ Containing No ε-particles; (▲) 1.5 wt% SIMFUEL; (□) 3 at% SIMFUEL; (●) 6 at% SIMFUEL; (x) 3 at% SIMFUEL Containing ε-particles but No Fission Products. Line (1) Is Drawn with a Slope of 90 mV/decade of Current, the Slope Expected on Noble Metals

rather than rely on the number of such sites pre-existing in the fuel surface, as is the case with O₂ (Figure 30). These sites are subsequently reduced by electrons liberated by the anodic reaction under open circuit corrosion conditions,

$$U^{V} + e^{-} \rightarrow U^{IV} \tag{23}$$

Under electrochemical conditions this chemical formation of DAR sites leads to a weak dependence of the cathodic current for reaction 23 on applied potential (i.e., large Tafel slopes of 200-400 mV⁻¹) and fractional reaction orders with respect to [H₂O₂] as a consequence of the potential dependent surface coverage by DAR sites (Goldik et al. 2004, 2005, 2006a, 2006b). Since the first reaction (reaction 22) is a chemical reaction dependent on [H₂O₂] and the second reaction (reaction 23) an electrochemical reaction dependent on potential, the rate controlling reaction changes from electrochemical at high [H₂O₂], when the chemical reaction is rapid, to chemical when [H₂O₂] is lower and the potential sufficiently negative. This transition with [H₂O₂] is illustrated in Figure 31 for data recorded on a SIMFUEL with no ε-particles.

For DGR conditions, when radiolytically-produced H₂O₂ will be many orders of magnitude lower than those used in laboratory experiments, the chemical reaction step would be expected to be rate controlling. As for O₂ reduction, there is a possibility that H₂O₂ reduction could be catalyzed on an RE^III-doped surface, which would introduce DAR sites, and possibly on ε-particles in SIMFUELs. However, electrochemical studies detected no discernible influence of RE^III-doping and only a minor influence of ε-particles at the high degrees of simulated burn-up anticipated in

LWR fuel (Shoesmith 2007; Goldik 2005). Thus, at the burn-ups achieved in CANDU fuel (~ 1.5 at%), when the number of ε-particles will be lower, the influence of these particles on H_2O_2 reduction would be marginal. This is a direct consequence of the ability of H_2O_2 to rapidly create U^{IV}/U^{V} DAR sites (reaction 22) making reduction on the oxidized $U^{IV}_{1-2x}U^{V}_{2x}O_{2+x}$ surface and on the ε-particles only marginally, if at all, different in rate, as opposed to the case with O_2, when these rates are very different. This difference in behaviour for O_2 and H_2O_2 is illustrated in Figure 32.
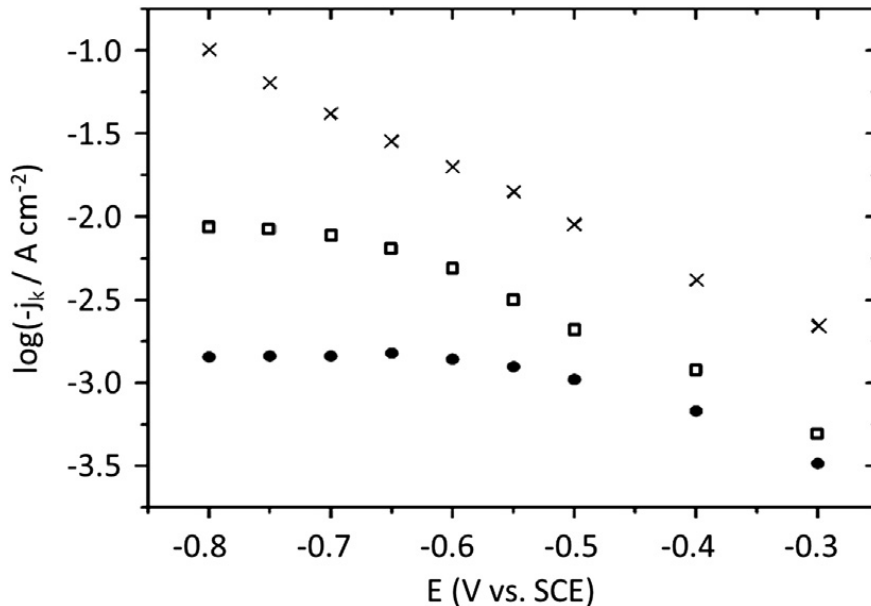
Figure 31: Tafel Plots Recorded on SIMFUEL (with No ε-particles) in 0.1 mol/L NaCl (pH = 9.7) Solution Containing Various [H_2O_2]: (●) 1.3 x 10^{-4} mol/L; (□) 4.0 x 10^{-4} mol/L; (x) 4.3 x 10^{-3} mol/L
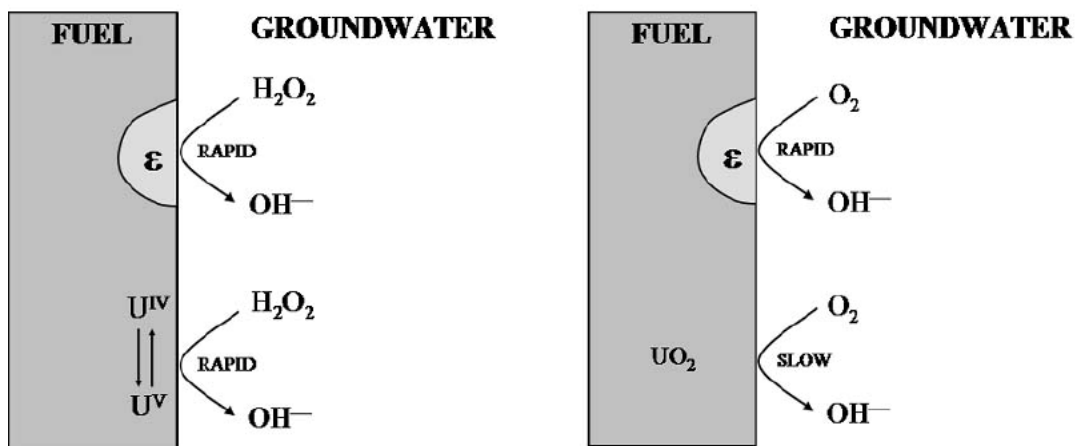
Figure 32: Illustrations Showing that H_2O_2 Reduction Is Rapid on Both the Fuel (UO$_2$) and ε-particles, While the Reduction of O_2 Is Only Rapid When Catalyzed on ε-Particles

5.10   The Consequences of Hydrogen Peroxide Decomposition

The kinetics of H_2O_2 reactions on UO_2 surfaces are complicated by the ability of H_2O_2 to participate in both the anodic and cathodic reactions. The influence of H_2O_2 on the anodic dissolution of UO_2 will be discussed below. Here, the emphasis is on the decomposition of H_2O_2 on the UO_2 surface. Besides causing corrosion by acting as a cathodic reagent,

$$H_2O_2 + 2e^- \rightarrow 2OH^- \tag{24}$$

H_2O_2 can also undergo oxidation,

$$H_2O_2 \rightarrow O_2 + 2H^+ + 2e^- \tag{25}$$

leading to its overall decomposition, as illustrated in Figure 33.
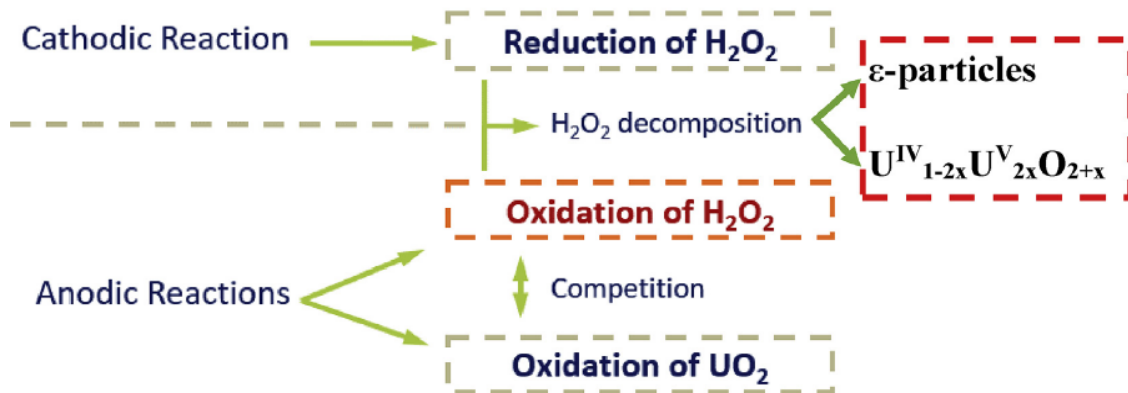
Figure 33: Schematic Illustration Showing That the Reduction of H_2O_2 Can Occur on Either the Catalytic $U^{IV}_{1-2x}U^{V}_{2x}O_{2+x}$ Surface or on ε-particles and Couple to Either UO_2 or H_2O_2 Oxidation

The decomposition of H_2O_2 has been studied on various metal oxides with recent studies showing the reaction proceeds via a radical mechanism (Lousada et al. 2013a; Barreiro-Fidalgo et al. 2018; Lin and Gurol 1998; Fu et al. 2010; Hiroki and LaVerne 2005; Zigah et al. 2012; Lousada et al 2013b),

$$(H_2O_2)_{ads} \rightarrow 2(OH^\bullet)_{ads} \tag{26}$$

$$(H_2O_2)_{ads} + (OH^\bullet)_{ads} \rightarrow H_2O + (HO_2^\bullet)_{ads} \tag{27}$$

$$2(HO_2^\bullet)_{ads} \rightarrow H_2O_2 + O_2 \tag{28}$$
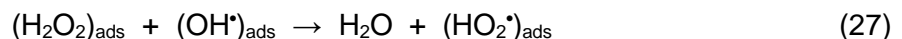
with the first electron transfer from adsorbed $OH^\bullet$ being the rate-determining step (Ekeroth and Jonsson 2003). The role of surface bound $OH^\bullet$ in both decomposition and dissolution reactions

has been demonstrated by monitoring the dynamics of OH$^\bullet$ scavenging using tris(hydroxymethyl)aminomethane (Lousada et al. 2013a, 2013b; Pehrman et al. 2012; Barreiro-Fidalgo et al. 2018).

The balance between corrosion and decomposition has been studied in some detail and shown to be a complex function of [H_2O_2] and [CO_3]$_{tot}$, the composition of the oxidized surface, and whether or not the oxide is RE^{III}-doped. The role of ε-particles in SIMFUELs on H_2O_2 reduction remains ambiguous. In chemical (as opposed to electrochemical) experiments (Maier et al. 2020), it was observed that consecutive exposures to H_2O_2 led to a decrease in U^{VI} release to solution but no decrease in the amount of H_2O_2 consumed (Figure 34). This was taken as evidence of alterations to the chemical state of the surface which continued to support decomposition but not dissolution. That this was the case was demonstrated in a series of experiments in which both the [CO_3]$_{tot}$ and [H_2O_2] were changed and the evolution of the surface condition was followed by measuring E$_{CORR}$, the changes in polarization resistance (R$_P$), and the surface composition using XPS (Zhu et al. 2020). The polarization resistance is inversely proportional to the total interfacial charge transfer rate but cannot distinguish between the anodic dissolution and H_2O_2 oxidation reactions. In both series of experiments the dominant reaction consuming H_2O_2 was shown to be decomposition, although the balance between corrosion and decomposition was different since one set of experiments was performed on undoped UO_2 and the other on 3 at% SIMFUEL. As noted in Section 5.6, RE^{III} doping of the matrix (present in SIMFUEL) stabilizes the matrix against corrosion which shifts the balance in favour of decomposition (Nilsson and Jonsson 2011).

Figure 35 shows an example of an electrochemical experiment in a 0.1 mol/L NaCl (pH = 9.7) solution containing H_2O_2 and HCO$_3^-$/CO$_3^{2-}$ (Zhu et al. 2020).
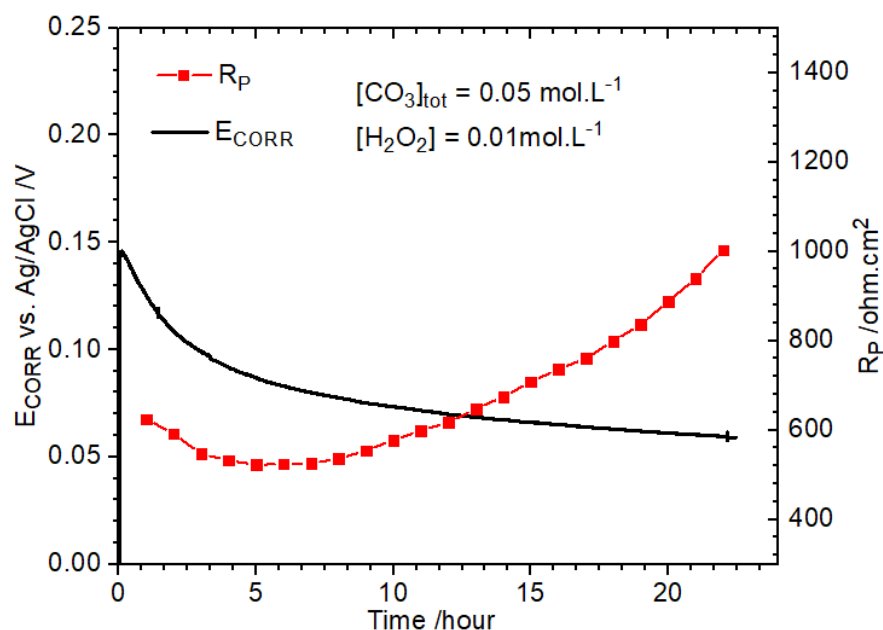
Figure 34: Corrosion Potential (E$_{CORR}$) and Polarization Resistance (R$_P$) Values as a Function of Time in a 0.1 mol/L NaCl (pH = 9.7) Solution Containing Carbonate and H$_2$O$_2$
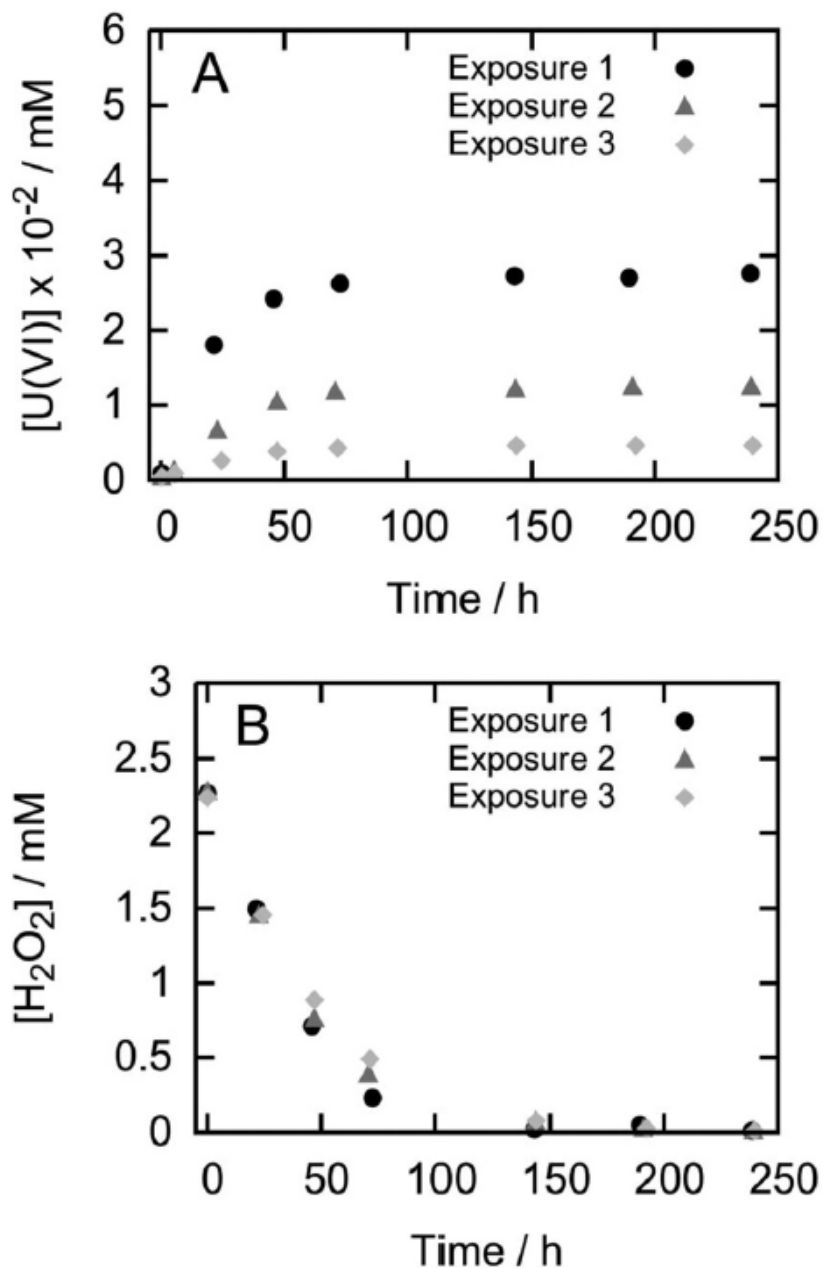
Figure 35: Uranium Release to Solution (A) and H₂O₂ Consumption on UO₂ (B) During Three Consecutive Exposures to a Deaerated 1 x 10⁻³ mol/L HCO₃⁻ Solution

The interfacial charge transfer rate (R_P^{-1}) initially increases accompanied by a decrease in E_{CORR}, a combination indicating an increase in the rate of the anodic reaction(s). At longer times, E_{CORR} continues to decrease while the interfacial charge transfer rate decreases (i.e., R_P increases) steadily, a combination indicating a decrease in the cathodic reaction rate consistent with the analytically determined consumption of H_2O_2. Since the fraction of H_2O_2 consumed by corrosion (over a 24 h period) is ≤ 4% and generally < 1% (depending on the $[CO_3]_{tot}$ (Zhu et al. 2020), the dominant reaction is H_2O_2 decomposition.

XPS analyses, Figure 36, show this initial acceleration (over ~4 h) is accompanied by an increase in the U^V content of the surface indicating catalysis of decomposition by a reversible redox transformation occurring on a $U^{IV}_{1-2x}U^V_{2x}O_{2+x}$ surface. At the high $[CO_3]_{tot}$ (0.05 mol/L), accumulation of U^{VI} species on the surface is avoided. This increase in U^V content continues into the later stages of the experiment (16 h), Figure 36.
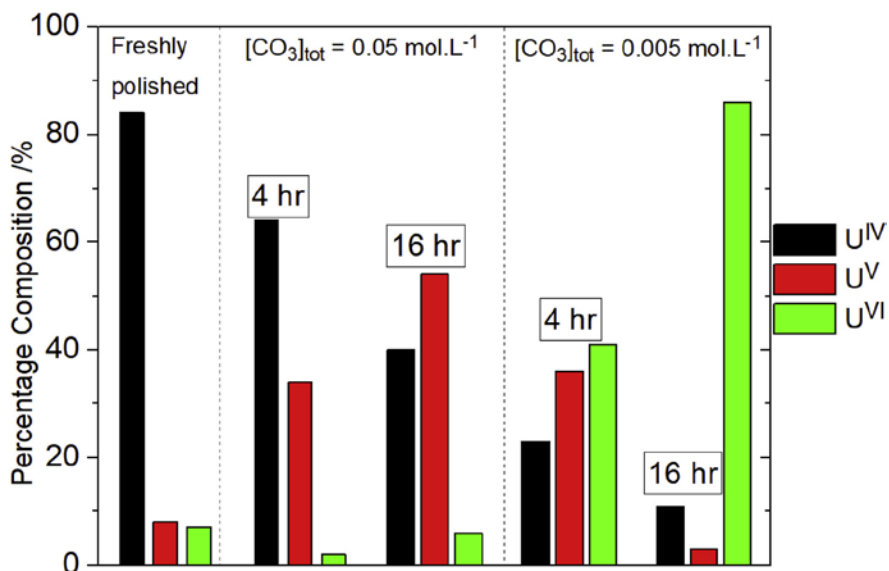
Figure 36: Percentage of U Oxidation States in a 3 at% SIMFUEL Surface after Exposure to a 10^{-2} mol/L H_2O_2 Solution Obtained by Deconvolution of the U $4f_{7/2}$ Peaks in XPS Spectra
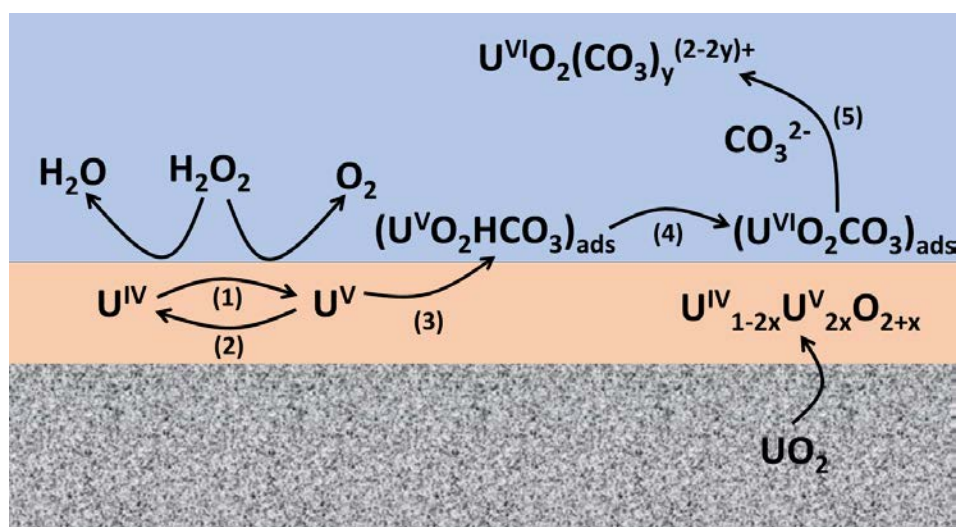
Figure 37: Illustration of the H_2O_2 Decomposition (Steps 1,2) and UO_2 Corrosion Reaction (Steps 3, 4, 5) Occurring on A $U^{IV}_{1-2x}U^V_{2x}O_{2+x}$ Surface Layer on UO_2

This catalyzed decomposition process is illustrated schematically by reactions 1 and 2 in Figure 37. Although not shown in the figure, this process proceeds via OH• radical species (reactions 26-28). For short immersion periods (~5 h), the changes in E_{CORR} and R_P with [H_2O_2] demonstrate that both the rate of formation of the $U^{IV}_{1-2x}U_{2x}O_{2+x}$ layer and the rate of decomposition on it increased as [H_2O_2] increased.

Figure 38 shows that, over the longer exposure period of 16 h (after which the initial acceleration in rate is complete, but before H_2O_2 depletion is extensive, Figure 35) the decomposition rate increased markedly without an accompanying change in E_{CORR}, a condition described as redox buffering (Sunder et al. 2004).

Under these conditions, the equilibrium potentials (E^e) for the two half reactions involved in decomposition exhibit dependencies on [H_2O_2] which are similar but opposite in sign,

$$(E^e)_{X3} = 1.54 - 0.059 \text{ pH} + 0.0295 \log [H_2O_2] \tag{29}$$

$$(E^e)_{X4} = 0.44 + 0.059 \text{ pH} - 0.0295 \log [H_2O_2] + 0.029 \log p_{O2} \tag{30}$$

Provided both reactions are rapid and equally influenced by [H_2O_2], the rate, but not E_{CORR} would change with [H_2O_2] as observed.
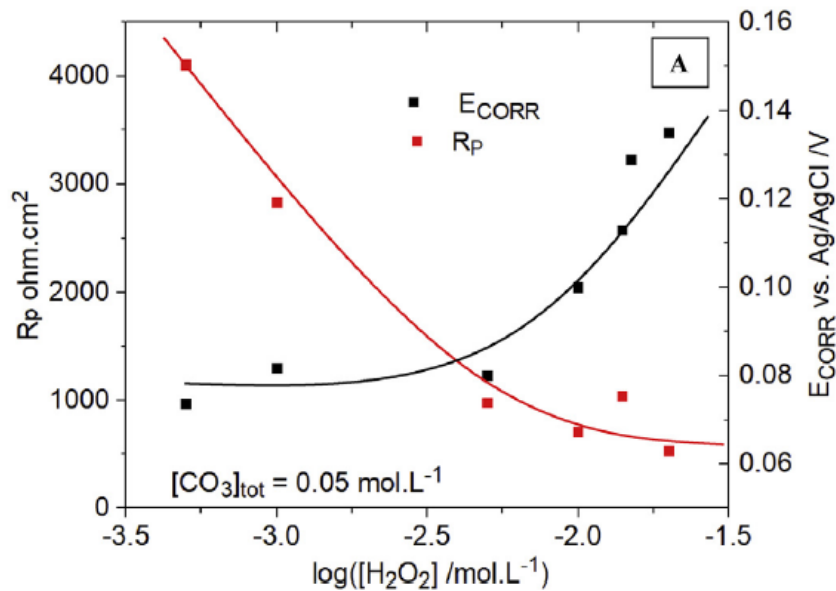
Figure 38: Polarization Resistance (R_P) and Corrosion Potential (E_{CORR}) Values as a Function of [H_2O_2] Recorded After 16 Hours Exposure to a 0.1 mol/L NaCl Solution Containing [CO_3]$_{tot}$ = 5 x 10^{-2} mol/L

If the surface is to remain catalytic for decomposition, the rate of reduction of U^V (reaction 2 in Figure 37) must exceed its rate of extraction from the lattice (reaction 3 in Figure 37) which destroys reversibility and leads eventually, via the reaction sequence 3 to 5 in Figure 37, to

dissolution as $U^{VI}O_2(CO_3)_y^{(2-2y)+}$. When both $[H_2O_2]$ and $[CO_3]_{tot}$ are high, this is the case. However, for a high $[H_2O_2]$ and low $[CO_3]_{tot}$ (Figure 36) the formation of an insulating U^{VI} layer, as either $U^{VI}O_3.2H_2O$ or $U^{VI}O_4.4H_2O$, blocks, at least partially, both decomposition and dissolution. Accelerating the reaction pathway 3/4/5 in Figure 37 by increasing $[CO_3]_{tot}$ also eventually leads to insulation of the surface as the rate of the chemical dissolution of the $(U^{VI}O_2CO_3)$ intermediate becomes rate determining. Complications due to the formation of uranyl peroxycarbonates are also possible.

The E_{CORR} values recorded in the presence of H_2O_2 (Sunder et al. 2004; Zhu et al. 2020; Wu et al. 2014a, Wu and Shoesmith 2014) are well above the value, established electrochemically, at which the onset of tetragonal distortions in the cubic UO_2 lattice can initiate dissolution (sections 5.6 and 5.7). Despite these high values the surface remains catalytic for H_2O_2 decomposition since the catalytic interconversion of U^{IV} and U^V is reversible which prevents the irreversible transition involving breakdown of the cubic structure which would lead to dissolution. A positive shift in E_{CORR}, which could disturb reversibility, requires $[H_2O_2]$ approaching 10^{-2} mol/L (Sunder et al. 2004; Zhu et al. 2019, 2020), a concentration many orders of magnitude beyond achievable $[H_2O_2]$ under DGR conditions. This suggests radiolytically-produced H_2O_2 should predominantly undergo decomposition rather than drive corrosion of the fuel matrix leading to radionuclide release. Additionally, the surface of the fuel is likely to remain in the catalytic state able to support radical reactions capable of scavenging radiolytic oxidants such as those induced in the presence of H_2 (Section 6.2).

5.11 Corrosion Product Deposits

If radiolytically-driven fuel corrosion was to persist with the limited transport of U^{VI} away from the fuel surface, then the accumulation of corrosion product deposits would be expected. This accumulation could have a number of effects:

(1) It could suppress corrosion by blocking the fuel surface to an extent determined by the porosity of the deposit.

(2) It could restrict the diffusive transport of species to and from the reacting surface. Since the primary oxidant driving corrosion (H_2O_2) is produced by α-radiolysis in a thin layer of solution at the fuel surface, a sufficiently thick, low porosity deposit could prevent diffusive loss of H_2O_2 from corrodible surface sites. Such a deposit could also hinder access of redox scavengers (Fe^{2+}, H_2) (Section 6) thereby reducing the efficiency of scavenging.

(3) Deposits could incorporate radionuclides released during fuel corrosion, thereby preventing, at least partially, their release to groundwater and modifying the yield and distribution of α-radiolysis products at the fuel surface.

(4) By restricting the diffusion of dissolved $U^{VI}O_2^{2+}$ away from the fuel surface, deposits could lead to local acidification via hydrolysis (reaction 6 (Section 5.8)) within pores in the deposit or defects in the fuel surface (fractures, locations of missing grains, fission-induced porosity). This issue was addressed in Section 5.8 and found not to lead to a significant increase in fuel corrosion rate. In the absence of acidification, pores and defects would be expected to seal by precipitation, since the concentration of dissolved U^{VI} would be highest

at the fuel surface making precipitation most likely at this location if a uranyl phase solubility limit is exceeded.

The physical and chemical properties of deposits will be determined by a combination of redox conditions, temperature, and groundwater composition. As discussed in Section 5.8, the key groundwater constituents are HCO_3^-/CO_3^{2-}, which increases the complexation of $U^{VI}O_2^{2+}$ and would hinder the formation of deposits, and Ca^{2+} and silicate which stabilize U^{VI} deposits.

The influence of the formation of corrosion product deposits has been investigated in detail under the permanently oxidizing conditions in the presence of limited amounts of H_2O anticipated in a Yucca Mountain (Nevada, USA) repository. The composition of the deposits (alteration phases) observed in laboratory drip tests using a Ca/silicate dominated H_2O were found to be similar to those observed in the geological alteration of natural uraninite (Wronkiewicz et al. 1992, 1996; Finch and Ewing 1991, 1992; Finch et al. 1999; Buck et al. 1997; Baker 2014). A summary of the phases expected, depending on the oxidizing conditions, is shown in Figure 39. The mineralogy of uranium is complex (Wronkiewicz 1999) and the phases shown represent general observations and not an exhaustive list of possibilities (Amme et al. 2005a; Turner and Wronkiewicz 2002; Finn et al. 1994a, 1994b; Kleykamp et al. 1985; Buck et al. 1997).

Whether or not the formation of alteration phases leads to the incorporation and retention of radionuclides released as the fuel corrodes will depend on many factors. Crystal structure considerations (Burns et al. 1997a, 1997b; Loida et al. 1995) suggest a wide range of phases are potential hosts for elements such as Np, Pu and Am including schoepite ($U^{VI}O_3.2H_2O$), ianthinite ($[U^{IV}_2(U^{VI}O_2)_4O_6(OH)_4(H_2O)_4](H_2O)_5$), becquerelite ($Ca[(U^{VI}O_2)_3O_2(OH)_3]_2(H_2O)_8$), compreignacite ($K_2[(U^{VI}O_2(OH)_3](H_2O)_8$, uranophane ($[Ca(U^{VI}O_2)_2(SiO_2OH)_2](H_2O)_5$) and boltwoodite ($K(H_3O)(U^{VI}O_2)(SiO_4)$, all potential alteration products in oxidizing Si-rich groundwaters (Wronkiewicz et al. 1992). The importance of radionuclide incorporation tends to disappear as redox conditions become less oxidizing and the formation of $U^{VI}O_2^{2+}$ decreases. This was clearly demonstrated for ^{237}Np (and ^{90}Sr, ^{99}Tc, ^{125}Sb) which were released in proportion to their fractional inventory (i.e., congruently) under anaerobic saline conditions but significantly retained in alteration phases under oxidizing conditions at 90°C (Buck et al. 1998).

Since oxidizing conditions within a failed waste container will be established by the α-radiolysis of groundwater at relatively low dose rates (Section 5.2), the deposition of the copious amounts of corrosion products formed in constantly aerated conditions will not occur. As discussed in Section 5.9, the corrosion behaviour of UO_2 in H_2O_2, the dominant oxidant produced by α-radiolysis (Eriksen et al. 2012), is complicated since H_2O_2 is not simply an oxidant but can participate in both the anodic and cathodic reactions involved in corrosion (Section 5.9). It can also be incorporated into uranyl peroxide phases such as studtite ($[(UO_2)O_2(H_2O)_2](H_2O)_2$), which tends to form at low temperatures (< 50°C), and dehydrated metastudtite ($(UO_2)O_2(H_2O)_2$), which forms at higher temperatures (Spano et al. 2020).
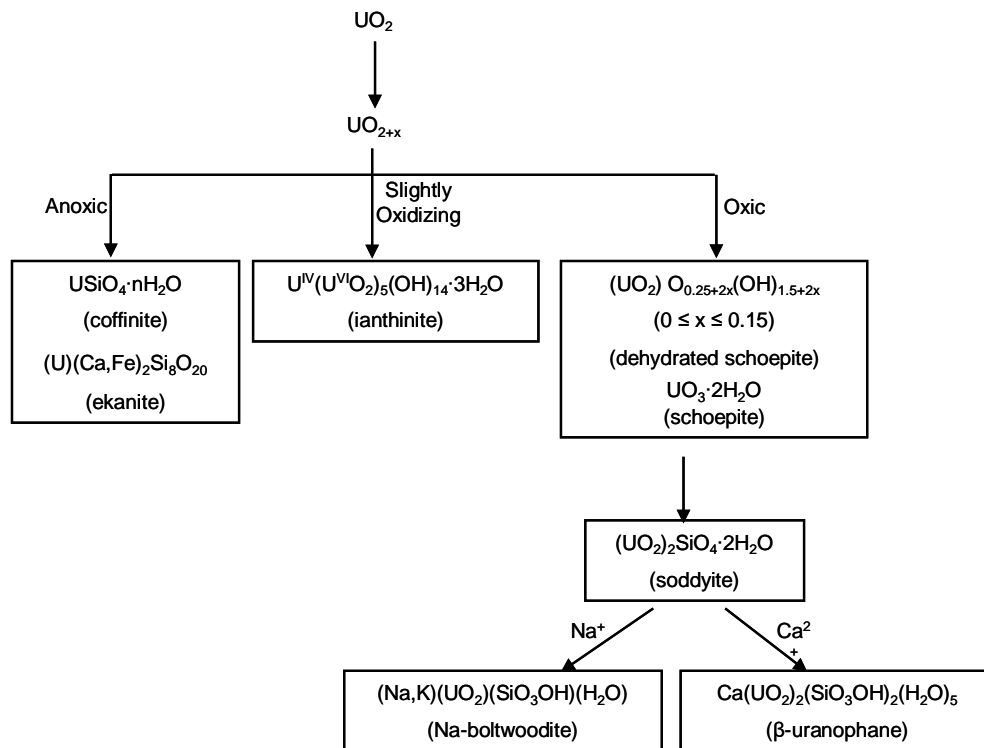
Figure 39: Reaction Scheme Showing the Possible Secondary Phases that Could Form on a Corroded UO₂ Surface for Different Redox Conditions

Studtite and metastudtite are the only two known uranyl peroxide minerals (Walenta 1974; Deliens and Piret 1983; Cejka et al. 1996; Burns and Hughes 2003; Kubatko et al. 2003; Weck et al. 2012), and since studtite is most commonly observed in close association with minerals such as uraninite (the natural analog for UO_2 fuel), it is likely formed by H_2O radiolysis to produce H_2O_2. Calorimetry and solubility measurements have established that studtite/metastudtite are stable in peroxide-bearing environments even at low $[H_2O_2]$ but unstable in the absence of H_2O_2 (Kubatko et al. 2003). Not surprisingly, they have been identified on spent nuclear fuel (McNamara et al. 2002; Hanson et al. 2005). Both phases were identified on spent nuclear fuel after immersion in deionized H_2O for 2 years, and X-ray diffraction demonstrated their presence on spent nuclear fuel after 37 years of aqueous leaching under aerated conditions (Roth et al. 2021). In the latter analysis, secondary phases were detected to a greater extent on fuel exposed to deionized H_2O than on fuel exposed to carbonate-containing synthetic groundwater. Both studtite and metastudtite were found to be the dominant phases in coexistence with metaschoepite $((UO_2)_8O_2(OH)_{12}\cdot10H_2O)$ and, on one sample with the mixed U^{IV}/U^{VI} phase ianthinite $(U^{IV}(U^{VI}O_2)_5O_7\cdot10H_2O)$. All surface phases were found to be subsequently dissolved in a carbonate-containing solution.

These observations are consistent with those of McNamara et al. (2002) and Hanson et al. (2005) who found that schoepite formed after short term exposure but was replaced in the longer term by studtite/metastudtite, and with studies showing that U^{VI} phases such as schoepite, soddyite (Forbes et al. 2011) and becquerelite (Kubatko et al. 2006) converted to studtite in the presence of H_2O_2 at millimolar concentrations. Studtite and metastudtite have

also been observed in analyzed lavas at Chernobyl (Ukraine) (Andersen et al. 1993) when extreme radiation fields, present under reactor accident conditions, can maintain the continued radiolytic production of H_2O_2 and sustain fuel corrosion (Armstrong et al. 2012). These phases have also been observed on fuel element cladding on spent nuclear fuel in storage areas (Abrafah et al. 1998) and areas associated with storage sites (Welsh et al. 1996) with other studies showing they are inevitably formed when radiation is present irrespective of whether it is alpha (Sattonay et al. 2001), beta (Clarens et al. 2005) or gamma (Jegou et al. 2005a). By contrast, examination of fuel from the Windscale advanced gas-cooled reactor showed no fuel oxidation after recovery from over four decades of pond storage during which flooding of the containers occurred. The observation of significant amounts of Fe^{II}/Fe^{III} corrosion products suggest scavenging of the radiolytically-produced H_2O_2 by Fe corrosion products (Section 6) (Woodall et al. 2021) as demonstrated by Amme et al. (2005b). Redox scavenging is discussed below in Section 6.

Based on experiments conducted predominantly in solutions containing significant concentrations of added H_2O_2, the deposition of studtite/metastudtite was observed for $[H_2O_2] \geq 5 \times 10^{-4}$ mol/L (Clarens et al. 2004; Corbel et al. 2006; Diaz-Arocas et al. 1995; Amme et al. 2002; Sundin et al. 2013) with its formation thought to involve a redeposition of dissolved $U^{VI}O_2^{2+}$

$$U^{VI}O_2^{2+} + H_2O_2 + 4H_2O \rightarrow [(UO_2)O_2(H_2O)_2]H_2O)_2 + 2H^+ \qquad (31)$$
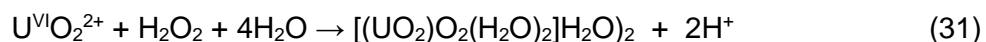
In the study by Corbel et al. (2006), H_2O_2 was produced by irradiating the UO_2/H_2O interface with a He^{2+} beam emerging through a UO_2 disc into the solution with an interfacial energy of ~ 6.5 ± 1 MeV typical of α-particles emitted by spent nuclear fuel. This led to a more rapid release of U than that observed when H_2O_2 was added to the solution chemically in the absence of irradiation suggesting a physical influence of α-particles on the corrosion process, although this was not confirmed. This possibility is discussed below in Sections 5.12 and 6.2.4. Also, the thickening of the studtite layer on the UO_2 surface slowed but did not prevent fuel dissolution indicating a meaningful porosity allowing corrosion to continue.

While the formation of studtite/metastudtite was not experimentally confirmed to occur at low $[H_2O_2]$, calorimetric calculations indicate these phases can form in the presence of $[H_2O_2]$ as low as 10^{-14} mol/L, suggesting they could play a role on aged fuel surfaces inside a failed waste container. However, their kinetic role, if one exists, in the overall corrosion process has not been elucidated. Dissolution studies (Kim et al. 2018; Li et al. 2020) show that the solubility, and hence the dissolution rate, of studtite is increased in HCO_3^- solutions (10^{-3} mol/L). This has been attributed to the formation of uranyl-peroxy-carbonate complexes such as $(UO_2)O_2(CO_3)_2^{4-}$ (Zanonato et al. 2012 and Section 5.9) detected by ^{13}C NMR analyses (Li et al. 2021). This dissolution process is accelerated in the presence of gamma radiation (Li et al. 2020; Rey et al. 2009), a feature attributed to the radiolytic decomposition of peroxides coupled with soluble complex formation (Li et al. 2020, 2021).

Both H_2O_2 decomposition when uranyl carbonates are present (Li et al. 2020, 2021) and scavenging by the Fenton reaction involving Fe^{2+} (Amme 2002; Amme et al. 2005b), which will be produced by container corrosion (Section 6), will suppress the formation of studtite/metastudtite. These observations, and the demonstration in electrochemical studies that surface peroxy carbonate species are involved in both anodic and cathodic corrosion reactions suggest studtite/metastudtite will play only a transitory role in the early stages of fuel corrosion.

5.12   Alpha Radiolysis Studies

As discussed in Section 5.2 (Figure 11), the majority of γ-emitting radionuclides will decay within the first few 100 years beyond which radioactive decay will be dominated by α-particle emission (Figure 10). If it is reasonably presumed that container failure will not occur before γ-radiation fields have become insignificant, then the dominant source of radiolytic oxidants will be the α-radiolysis of H_2O. The many studies on the influence of γ-radiolysis, which have contributed substantially in determining the mechanistic details of radiation-induced corrosion (Eriksen et al. 2012) are discussed throughout various sections in this report. Here, the emphasis is on the influence of α-radiolysis on UO_2, SIMFUEL, and spent fuel corrosion.

Since α-radiation is a high linear energy transfer (HET) form of radiation, it forms radiolysis products within a narrow radiation zone close to the UO_2/H_2O interface (Nielsen and Jonsson 2006), but with a non-uniform distribution since the α-particles lose energy along a penetration pathway in the H_2O. The dose rate distribution in H_2O in contact with used fuel has been calculated using a number of approaches described elsewhere (Nielsen and Jonsson 2006; Garisto et al. 2009; Sunder 1998; Garisto et al. 2004; Poulesquen et al. 2006). Since the maximum distance α-particles can travel in UO_2 is ~13 μm, only emitters located near the fuel surface contribute to solution radiolysis, and due to the rapid deposition of energy in H_2O, radiolysis products are produced within an ~ 30 μm layer at the fuel surface.

Many studies have been conducted with the aim of relating the fuel corrosion rate to the α-radiation field. Both static and dynamic leaching experiments have been carried out with ^{238}Pu- and ^{233}U-doped UO_2 as well as ^{225}Ac-doped UO_2 colloids. Different doping levels simulating fuels after various "cooling" times, from fuel freshly discharged from reactor to fuel with the anticipated radiation fields expected 10^6 years after discharge from reactor, have been employed. In these specimens the α-emitter is homogeneously mixed in the UO_2 matrix in the quantities necessary to produce the required α-dose rate. The results of the European program have been reported in detail (Poinssot et al. 2005).

Early experiments by Gray (Gray 1988) performed in brine at 90 °C on ^{238}Pu- and ^{239}Pu-doped UO_2 (with specific activities of 1.06 and 172.6 MBq/g(UO_2)) showed the extent of corrosion for the doped fuel with the higher specific activity was approximately one order of magnitude higher than that for undoped UO_2, but no direct correlation to α-activity was established. Similar experiments (Rondinella et al. 2000; Rondinella et al. 2011) conducted in distilled H_2O with monoliths and crushed samples of UO_2 doped with ^{238}Pu (0.1 and 10% ^{238}Pu) also showed a radiation accelerated corrosion rate compared to undoped UO_2, but again a clear correlation between rate and α-activity was not observed. In the absence of HCO_3^- to complex $U^{VI}O_2^{2+}$, the accumulation of U^{VI} deposits on the surface was observed (Cobos et al. 2002). That the rate increased with α-activity was confirmed in experiments using ^{225}Ac-doped UO_2 nanoparticles under controlled reducing conditions in 1 M NaCl at pH 6. The influence of accumulated corrosion product deposits in suppressing corrosion was observed in electrochemical experiments on ^{238}Pu-doped UO_2, the rate being lower when HCO_3^- was not present (Stroes-Gascoyne et al. 2002, 2005). In HCO_3^--containing solutions, when U^{VI} deposits were avoided, a surface enrichment of ^{238}Pu was observed. Additional experiments (Jegou et al. 2005b; Carbol et al. 2005; Muzeau et al. 2009) produced similar correlations despite the wide range of experimental conditions employed.

Irradiation with α-sources placed in H_2O at various distances from the UO_2/H_2O interface have been used in electrochemical studies (Sunder et al. 1997) to demonstrate a clear influence of α-source strength on the surface oxidation rate of UO_2, but attempts to demonstrate a clear dependence of rate on source strength was again complicated by the accumulation of corrosion product deposits (Wren et al. 2005) at high source strengths. In the study by Wren et al. (2005), a comparison of the rate of increase in E_{CORR} (taken to be indicative of a combination of surface oxidation ($U^{IV}O_2 \rightarrow U^{IV}_{1-2x}U^{V}_{2x}O_{2+x}$) and dissolution ($U^{IV}_{1-2x}U^{V}_{2x}O_{2+x} \rightarrow U^{VI}O_2^{2+}$)) to the rate of radiolytic production of oxidants (predicted by a finite element model based on α-radiolysis reactions) showed surface reactions were proceeding much slower than expected based on the predicted surface concentrations of H_2O_2.

One possibility for this discrepancy is that surface oxidation is being driven by O_2 produced by the catalyzed decomposition of H_2O_2 on the $U^{IV}_{1-2x}U^{V}_{2x}O_{2+x}$ surface, as discussed in Section 5.10. However, this was insufficient to explain the discrepancy leading to the claim that $OH^{\bullet}$ radicals produced by the surface catalyzed decomposition of H_2O_2 (Section 5.10)

$$H_2O_2 + e^- \rightarrow OH^{\bullet} + OH^- \qquad (32)$$

$$U^{IV} \rightarrow U^{V} + e^- \qquad (33)$$

were consumed by reaction with radiolytically produced H_2, confined at the surface in the thin layer electrochemical cell. The coupling of this reaction to the regeneration of the U^{IV} surface

$$H_2 + OH^{\bullet} \rightarrow H_2O + H^+ + e^- \qquad (34)$$

$$U^{V} + e^- \rightarrow U^{IV} \qquad (35)$$
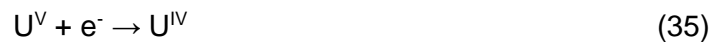
resulted in the overall recombination of the radiolytic oxidant (H_2O_2) and reductant (H_2). In these experiments, the combined influence of decomposition and recombination is to retard but not stop the oxidation/corrosion of the surface which eventually accumulates $U^{VI}O_3 \cdot yH_2O$ in the absence of HCO_3^-.

In an attempt to more closely simulate the influence of α-irradiation emitted by the UO_2 rather than that of externally-produced radiolysis products, Sattonay et al. (2001) used a cyclotron to irradiate the UO_2/H_2O interface with a high energy (45 MeV) beam of $^4He^{2+}$ ions (α-particles). The α-particles passed through a thin (~300 μm) UO_2 disk into aerated deionized H_2O with an energy of ~ 5 MeV which is comparable to the maximum energy of α-particles emitted by spent fuel. Comparison to rates measured at zero flux showed the corrosion rate was increased by 4 orders of magnitude for the highest flux used (3.3×10^{11} particles·cm^{-2}s^{-1}). Since the fluxes used are so large, the results are not immediately relevant to DGR conditions, but demonstrated that, at least for these fluxes, metastudtite ($U^{VI}O_4 \cdot 2H_2O$) was formed as a secondary phase.

Corrosion rates measured as a function of α-activity have been discussed in detail (Poinssot et al. 2005) and are plotted in Figure 40.
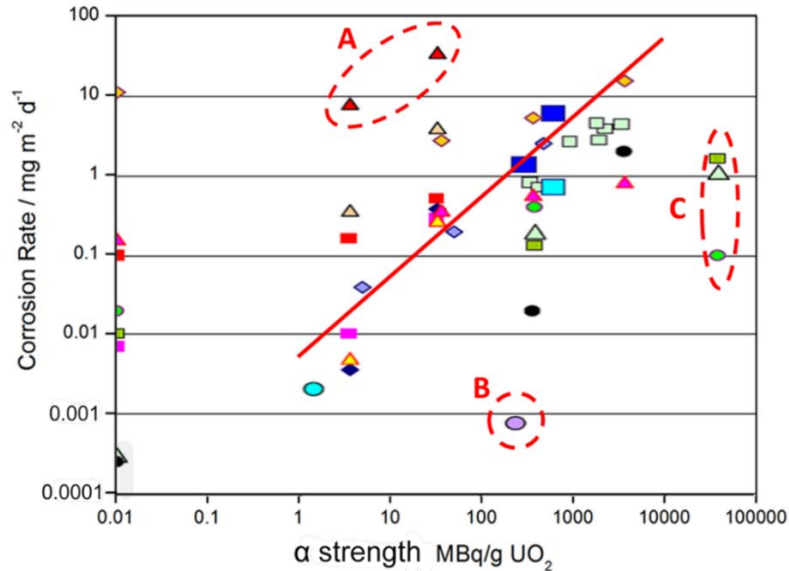
Figure 40: Corrosion Rates (Poinssot et al. 2005) of α-emitter Doped UO₂, Non-doped UO₂ (0.01 MBq/g), SIMFUEL, and Some Spent Fuel. The Line Shows a Linear Least Squares Fit to the Data. The Values Marked A, B and C Are Not Included in the Fit for Reasons Discussed in the Text

These measurements were conducted on a wide range of specimens including ^{233}U-doped UO$_2$, ^{239}Pu-doped UO$_2$, ^{225}Ac-doped UO$_2$, UO$_2$ fuel pellets, SIMFUEL and used fuel. While significant variability exists, a clear trend of increasing corrosion rate with increasing α-activity was established. It was suggested that for α-source strengths below the range ~1 to 3 MBq/g(UO$_2$), the influence of α-radiolysis becomes insignificant, as illustrated schematically in Figure 41. The rates measured for undoped UO$_2$ (i.e., at 10^{-2} MBq/g(UO$_2$)) are widely scattered reflecting the variations in experimental exposure conditions, the possibility of a presence of trace oxidants, and the rapid dissolution of pre-oxidized layers.

It was claimed that above the "threshold" in Figure 41, fuel dissolution was radiolytically-controlled (i.e., a corrosion process) while below it dissolution could be considered solubility controlled (i.e., a chemical dissolution reaction). Solubility control was assumed to be established for dissolved U concentrations < 10^{-9} mol/L (comparable to the OECD-NEA recommended value of 10$^{-8.5}$ mol/L for the solubility of UO$_2$ (Section 2)), E$_h$ values < -0.01 V (-0.25 V vs SCE), and the observation in long term experiments that the [U] did not increase with time. More recent studies suggest this threshold could be approximately an order of magnitude higher (between 18 and 33 MBq/g(UO$_2$)) (Muzeau et al. 2009).
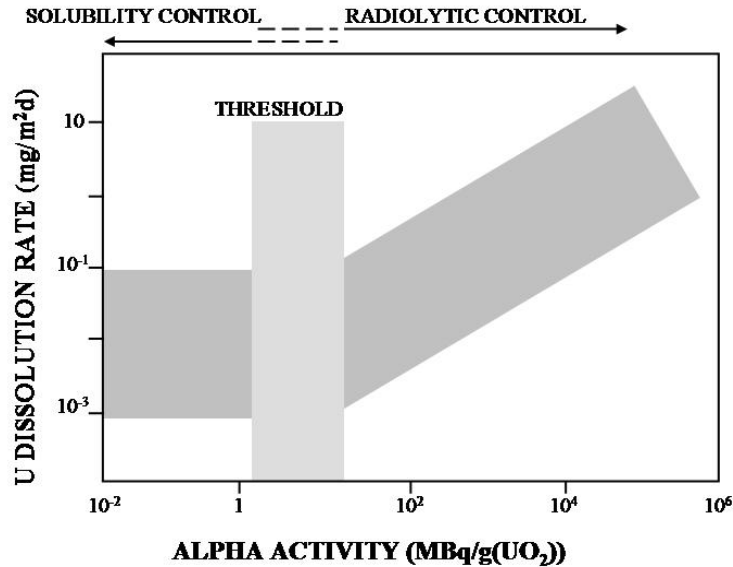
Figure 41: Illustration Showing the Concept of an α-activity Threshold for the Onset of Radiolytically-controlled Fuel Corrosion. The Darker Shaded Areas Illustrate the Spread in Measured Rates Shown in Figure 40 Excluding Those in the Areas Marked A, B and C

Within this compilation, three sets of data (marked A, B and C) appear as outliers. The details for these data sets are described in Poinssot et al. (2005). Corrosion rates marked A were calculated from electrochemical impedance spectroscopy measurements which required the compensation of large resistances in low conductivity material. This led to large errors and an overestimation of the rates. The value labelled B was measured in a clay environment known to contain reducing species such as humic acids. The values labelled C were measured on highly [239]Pu-doped specimens, and it has been suggested (Poinssot et al. 2005; Stroes-Gascoyne et al. 2002, 2005), but not proven, that the lower rates than expected indicate a stabilized UO_2 matrix due to the presence of Pu. The line drawn in Figure 40 is a fit to the data (excluding A, B, and C) confirming a linear relationship between corrosion rate and α-source strength). A similar fit to experimental data was also established by Eriksen et al. (2012).

The vertical light shaded area in Figure 41 shows the threshold for an observable influence of α-radiolysis on fuel dissolution will be somewhere in the region 1 to 33 MBq/g(UO_2). A comparison of the dose rates to solution for the upper and lower limits of this threshold to those calculated for a CANDU fuel bundle with a burn-up of 220 MWh/kg(U) shows the dose rates for CANDU fuel only marginally exceed the upper limit and only at short times (≤ 300 to 400 years) when container failure and exposure of the fuel to groundwater would not be expected. Two observations can be made: (i) the corrosion rate measured for the upper limit of this threshold can be considered the maximum sustainable by α-radiolysis for CANDU fuel; and (ii) no radiolytic corrosion should be possible for CANDU fuel beyond ~10,000 to 20,00 years, when the alpha dose rate falls below the lower threshold. For typical burnup BWR/LWR fuels, alpha dose rates would be several times higher. It should be noted at this juncture that these calculations do not include the influence of H_2 in suppressing corrosion which is discussed in Section 6.

55555555555555

6. THE INFLUENCE OF REDOX SCAVENGERS ON FUEL CORROSION

As illustrated in Figure 42, two corrosion fronts interconnected by groundwater diffusion processes will exist within a failed groundwater-containing container. Since the separation in corrosion potentials (E_{CORR}) between the two surfaces is large (Figure 11), this introduces the possibility that the products of steel corrosion (Fe^{2+} and H_2) will scavenge the radiolytic oxidants (dominantly H_2O_2) responsible for UO_2 corrosion.
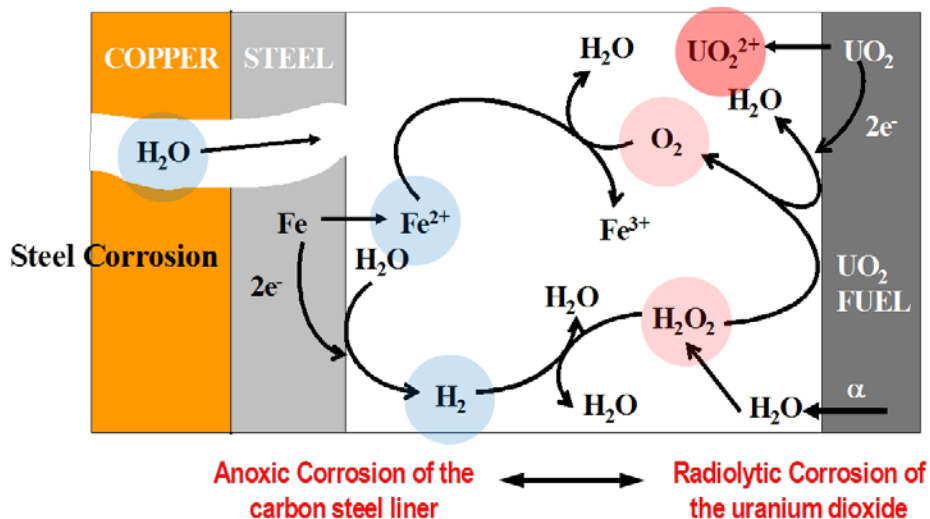
Figure 42: Illustration Showing the Two Corrosion Fronts that Will Exist Within a Groundwater-containing Failed Container. Since the Cladding on the Fuel is Expected to be Inert, it Will be Only a Physical Barrier and Not Involved in the Redox Chemistry.

6.1 Ferrous Ions

Ferrous ions (Fe^{2+}) are well known regulators of redox conditions in natural waters and their reaction with oxidants, in particular O_2, has been extensively studied (Stumm 1990). The overall reaction can be written,

$$O_2 + 2H_2O + 4Fe^{2+} \rightarrow 4Fe^{3+} + 4OH^- \tag{36}$$

where the exact speciation of Fe^{II} and Fe^{III} is determined by groundwater composition, redox conditions, and pH. The reaction is highly pH-dependent, with a rate that increases markedly with pH and, in neutral solutions, leads to the precipitation of $Fe(OH)_3$ and other Fe^{III} solids (Tamura et al. 1976). The redox chemistry of the steel/iron oxide/soluble Fe system and its likely impact on fuel corrosion have been reviewed in detail (Johnson and Smith 2000; King and Stroes-Gascoyne 2000).

The radiolytic oxidant, H_2O_2, will also be consumed by the Fenton reaction (Barb et al. 1951; Sutton and Winterbourn 1989; Zepp et al. 1992),

$$Fe^{2+} + H_2O_2 \rightarrow Fe^{3+} + OH^\bullet + OH^- \tag{37}$$

$$Fe^{2+} + OH^\bullet \rightarrow Fe^{3+} + OH^- \tag{38}$$
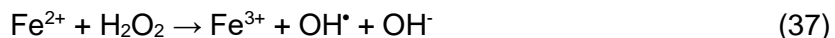
An effective G-value for H_2O_2 as low as 0.001 has been claimed for the Fe^{II}/Fe^{III} system (Christensen and Bjergbakke 1982), and calculations based on α-radiolysis models show that concentrations of Fe^{2+} in the expected groundwater range within a failed container ($\sim 10^{-5}$ mol/L) can significantly arrest the rate of H_2O_2 production (Tait and Johnson 1986). Studies on the influence of Fe and Fe corrosion products have been published (Loida et al. 1996, 2001a, 2006; Grambow et al. 1996b; El Aamrani et al. 1998; Albinsson et al. 2003; Cui et al. 2003; Quinones et al. 2001; Ollila et al. 2003; Stroes-Gascoyne et al. 2001; Amme et al. 2005b; Puranen et al. 2016), and inevitably show that fuel corrosion and radionuclide release are suppressed in the presence of Fe. Measurements over a period of 4.5 years demonstrated a reduction in the release rate of ^{90}Sr by a factor of 460 due to the presence of Fe (Ollila et al. 2003), where ^{90}Sr release is taken as an indicator of the matrix corrosion rate. In experiments with [233]U-doped UO_2, dissolved U concentrations were lower than the solubility limit when active Fe was present.

Separating the effects of the two possible redox scavengers (Fe^{2+}, H_2) on fuel corrosion is difficult in experiments conducted in the presence of Fe. That H_2 is the dominant steel corrosion product suppressing the corrosion of UO_2 was clearly demonstrated by Puranen et al. (2020) in experiments in which the release of radionuclides from spent fuel (in particular, [85]Rb, ^{90}Sr and [135]Cs) was measured over exposure intervals up to 3 years in an anoxic simplified groundwater (10^{-3} mol/L NaCl + 2 x 10^{-3} mol/L HCO_3^-) at room temperature. When fuel leaching was measured in the presence of only magnetite (Fe_3O_4), the demonstrated corrosion product for anoxic steel corrosion ($3Fe + 4H_2O \rightarrow Fe_3O_4 + 4H_2$), released radionuclide concentrations reached values up to 2 orders of magnitude higher than when a similar experiment was conducted in the presence of corroding Fe. Since only Fe^{2+} was present in the magnetite experiment, but both Fe^{2+} and H_2 were produced in the second experiment, these results confirm a much greater role for H_2 than for Fe^{2+} in the suppression of fuel corrosion.

Direct attempts have been made to determine the influence of Fe^{2+} on UO_2 corrosion (Loida et al. 2006; Quinones et al. 2001; Cui and Spahiu 2002, Cui et al. 2011; Odorowski et al. 2017). Addition of Fe^{2+} to experiments with Pu-doped electrodes (Stroes-Gascoyne et al. 2001) suppressed E_{CORR} by 140 mV indicating a direct influence on the concentration of alpha radiolytically-produced oxidants at the UO_2 surface. Calculations based on the Fenton reaction and experimentally determined rate constants showed a substantial suppression of UO_2 dissolution (by a factor of 40) (Nielsen et al. 2017). More recent model calculations show that, as the $[Fe^{2+}]$ increases towards its solubility limit for groundwaters in the expected repository pH range, the radiolytically-produced H_2O_2 is scavenged by the Fenton reaction at locations progressively closer to the fuel surface (Wu et al. 2012) (Figure 43). At the fuel surface itself, where the influence of Fe^{2+} is determined by the relative rates of the Fenton reaction and the interfacial corrosion rate, the influence is relatively minor (Figure 43). When the accumulation of corrosion product deposits is included in model calculations and access of Fe^{2+} to the UO_2 surface controlled by limited porosity in the deposit, the influence of Fe^{2+} becomes marginal (King and Kolar 2002).
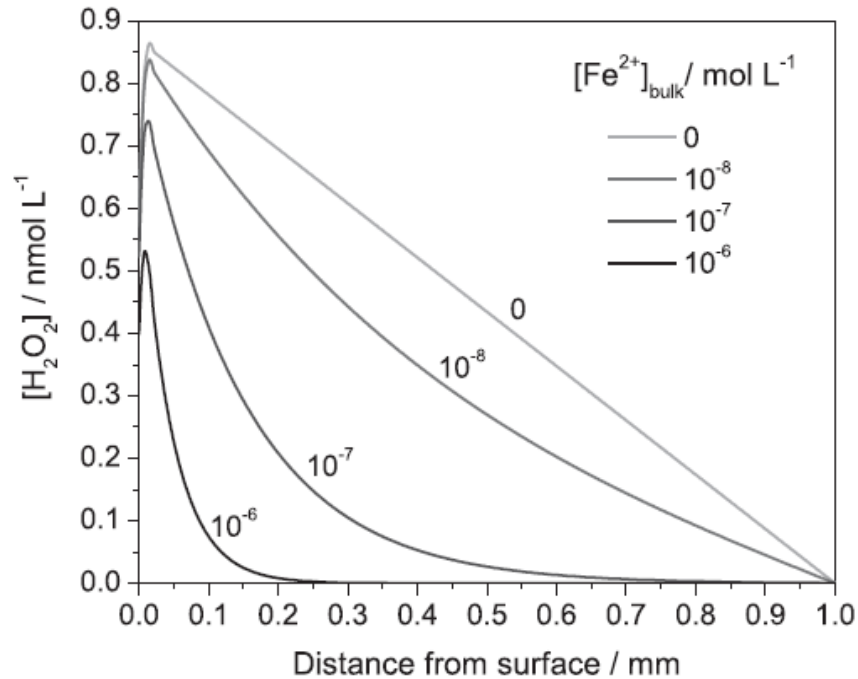
Figure 43: Calculated [H₂O₂] Profiles As a Function of Distance from the Fuel Surface at Various [Fe²⁺] with the Largest Concentration Approaching the Solubility Limit for Fe²⁺. Calculations Were Performed Using the Model of Wu et al. (2012)

6.2   Hydrogen (H₂)

Within a failed container there are two sources of H_2: (i) radiolytic production; and (ii) formation by the anoxic corrosion of the iron/steel inner containment vessel with groundwater which will be the major source,

$$3Fe + H_2O \rightarrow Fe_3O_4 + 4H_2 \tag{39}$$

Assuming a significant volume of groundwater has entered the container, the rate of H_2 production will exceed its diffusive escape through the compacted clay surrounding the container and the dissolved [H_2] will rapidly exceed its solubility (Liu and Nerenieks 2002; Sellin 2002). Given the hydrostatic pressure at a DGR depth of 500 m (~ 5 MPa, or 50 bar) this would lead to a dissolved [H_2] of ~ 40 mmol/L.

A considerable database of information on the influence of H_2 has been accumulated on a wide range of materials:

(a) Spent nuclear fuels, in particular PWR and MOX fuels. Since these fuels have been recently discharged from the reactor (on the time scale of the radiation fields associated with the fuel (Figure 10)), they have significant γ/β/α radiation fields.

(b) Alpha-doped UO_2 to which various actinides (either ^{238}Pu, ^{239}Pu or ^{233}U) have been added to simulate the much lower α-radiation dose rates expected in spent fuel once γ/β fields have become insignificant after extended disposal times.

(c) SIMFUELS (described in 5.3) which contain key fission products to simulate the chemical properties of the fuel without the associated radiation fields.

(d) UO_2, as pellets or powder, which exhibit only the basic matrix properties.

6.2.1 Spent Fuels

The influence of H_2 on the leaching of radionuclides from spent fuel has been extensively studied (Spahiu et al. 2000, 2002, 2004; Loida et al. 1996, 2001b, 2005; Grambow et al. 1996a, 2000; Poinssot et al. 2005; Carbol et al. 2005, 2009a; Fors et al. 2009; Puranen et al. 2020; Röllin et al. 2001; Ollila et al. 2003; Ekeroth et al. 2020) with the results from large European projects comprehensively discussed in summary reports (Grambow et al. 1996a, 2000; Poinssot et al. 2005). Early studies (Grambow et al. 1996a) conducted on high burn-up spent fuel in the presence of powdered Fe and its corrosion products showed that the release of the important radionuclides (^{90}Sr, ^{137}Cs, ^{239}Pu) decreased as the H_2 pressure (from Fe corrosion) in the experimental vessel increased up to 2.8 bar over 1,049 days. To avoid the ambiguity introduced by the presence of Fe^{2+} from Fe corrosion, a static corrosion experiment was conducted in the absence of Fe in 5.0 mol/L NaCl solution with an overpressure of 3.2 bar of H_2 (Carbol et al. 2005). Initially, when the vessel was Ar-purged, the matrix dissolution rate (using ^{90}Sr release as an indicator) was ~ 14 times higher than when H_2 was subsequently introduced. The influence of H_2 persisted for the duration of the experiment.

The measured U concentrations were compared to calculated solubilities for UO_2 and U^{VI} solids using available thermodynamic data sets for U^{IV}/U^{VI} aqueous species and solids (Fanhagel and Neck 2002; Neck and Kim 2001). When H_2 was present, the measured U concentrations were essentially coincident with the calculated UO_2 solubility demonstrating equilibration with the unoxidized fuel. Despite its radiolytic production, O_2 was analytically below the detection limit indicating efficient oxidant scavenging.

In the absence of Fe, scavenging by the formation of Fe^{III} corrosion products was not possible leaving H_2 as the only possible reductant. A leaching experiment with MOX fuel (average burn-up of 48 MWd/kgU) showed that the dissolution of even highly α-active fuel could be completely suppressed with a sufficiently high H_2 pressure (53 bar; equivalent to a dissolved [H_2] of 4.3 x 10^{-2} mol/L) (Carbol et al. 2005). In this last experiment, a dissolution rate could not be calculated since once the pre-oxidized layer on the fuel surface, present when the experiment was started, had dissolved, no further release of U could be detected, with the final U concentration being close to that expected for the unoxidized UO_2 matrix.

Although commonly used, high [H_2] are not required to suppress spent fuel corrosion rates, a decrease of 3 to 4 orders of magnitude being achieved with 8 x 10^{-4} mol/L (equivalent to a pressure of ~ 1 bar) compared to rates measured under oxidizing conditions (Figure 44).
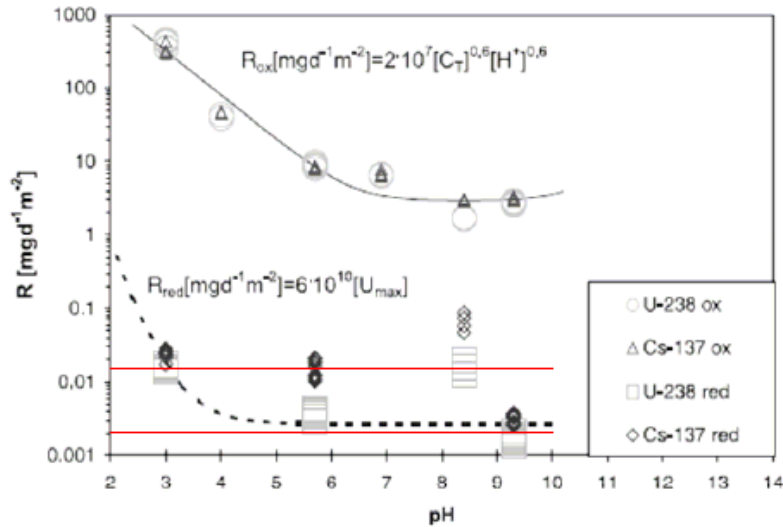
Figure 44: Used Fuel Dissolution Rates As a Function of pH for Oxidizing and Reducing Conditions. Oxidizing Conditions - Solution Purged with 20% O_2/0.03% CO_2/80% Ar; Reducing Conditions – Solution Bubbled with H_2 Containing 0.03% CO_2 in the Presence of a Pt Foil (Rollin et al. 2001). The Horizontal Red Lines Bracket the Corrosion Rates Derived by Extrapolating Experimental Electrochemical Data to the Potential Threshold -0.4 V vs SCE (-0.35 V to -0.45 V vs SCE) for Oxidative Dissolution (Corrosion) of UO_2 Using the Model Described in Shoesmith et al. (2003)

In a series of experiments performed over the pH range 3 to ~9.5, rates measured under oxidizing conditions exhibited the expected pH dependence for pH < 6 (Torrero et al. 1997; de Pablo et al. 1996) whereas under reducing conditions the absence of a pH dependence in the presence of H_2 (Figure 46) was consistent with a chemical (anoxic) dissolution process (Figure 3).

Studies on high burn-up fuel (59.1 GWd/tHM) in the presence of 4.1 MPa (0.033 mol/L) of H_2 showed similar behaviour confirming that the high burn-up structure present in the outer rim of the fuel did not enhance the corrosion/dissolution rate (Fors et al. 2009) despite the increased actinide and fission product content. The measured dissolved U concentrations were in the range 1.5×10^{-10} mol/L, despite in-leakage of air leading to temporary increases to 2×10^{-8} mol/L. This regulation of temporary U releases suggests U is reduced and redeposited, a process which appears to be accompanied by the coprecipitation of initially released redox sensitive radionuclides (Tc, Np, Pu). The [U] were significantly lower than those expected for UO_2 redeposited in the amorphous form (~ 10^{-9} mol/L) (Parks and Pohl 1988; Guillamont et al. 2020; Rai et al. 2003), possibly indicating an α-radiation induced H_2 annealing or crystallization process.

More recent analyses (Ekeroth et al. 2020) support the overall conclusion that, in spite of unavoidable air incursions, H_2 pressures ≥ 1 bar effectively suppress fuel corrosion. That U was present only in the reduced (U^{IV}) form was confirmed by comparing XPS spectra recorded on samples not exposed to the H_2-containing solution, samples exposed in the leaching experiment, and the fractured surface of a certified UO_2 pellet not exposed to air.

6.2.2 Alpha-doped UO_2

To study the combination of α-radiation and H_2 without the interference from γ/β-radiation fields, which are expected to be insignificant by the time container failure occurs (Figure 10), UO_2 specimens doped with different fractions of α-emitters ([238]Pu, [239]Pu, [233]U) have been used to simulate (a) the levels of α-activity that will prevail in spent fuel after various periods of containment (Poinssot et al. 2005; Carbol et al. 2005, 2009b; Muzeau et al. 2009) as well as (b) the exposure of UO_2 specimens to external α-sources brought within 30 μm of their surfaces (Wren et al 2005; Sunder et al. 1990; Hansson et al. 2021).

In experiments using 10% [233]U-doped UO_2 in a solution containing 2 x 10^{-2} mol/L NaCl and 2 x 10^{-3} mol/L HCO_3^-, in which the H_2 pressure was varied from an initial value of 16 bar ([H_2] = 10^{-2} mol/L) to a final value of 0.01 bar ([H_2] = 10^{-5} mol/L), all measured indicators demonstrated complete suppression of corrosion (Figure 45).

- The dissolved [U] was extremely low (≤ 10^{-10} mol/L) indicating U release was under solubility control over the full 2 years of the experiment.

- The initial E_h (~ -0.1 V (vs SHE)) decreased to ≤ -0.3 V (vs SHE) over the first 50 days, and only rose again when [H_2] was reduced to its lowest value. Despite this increase in E_h, the [U] did not increase indicating maintenance of non-oxidizing conditions at the fuel surface.

- Measured [O_2] were at the detection limit (~ 10^{-8} mol/L) confirming that the radiolytically produced O_2 was effectively scavenged.

- XPS analyses of the exposed UO_2 surface indicated no surface oxidation.

Since no change in [U] occurred over the full 2 years of the experiment, it could be concluded that complete suppression of α-radiolytic corrosion had been achieved.

A similar study conducted over a much shorter period (14 to 32 days) compared the release of U from UO_2 doped with [238]Pu/[239]Pu to reproduce the α-activity of spent fuel with a burn-up of 47 GWd·tHM after 50 and 10,000 years of decay (385 and 18 MBq/g(UO_2), respectively) (Muzeau et al. 2009). Experiments were conducted in a 10^{-3} mol/L HCO_3^- solution pressurized to 3.5 bar with either Ar or Ar + 30% H_2 (Figure 46).

The early equality in [U] in the three experiments can be attributed to the rapid chemical dissolution of an oxidized (U^{VI}) layer on the UO_2 surface on first immersion. In the absence of H_2, U release continues for the duration of the experiment. By contrast, once the initially present U^{VI} oxide layer has dissolved, the [U] decreased to a low value consistent with U release controlled by the solubility of the UO_2 matrix for both α-activity levels. A similar suppression of corrosion was achieved with 1 bar ([H_2] = 7.8 x 10^{-4} mol/L).
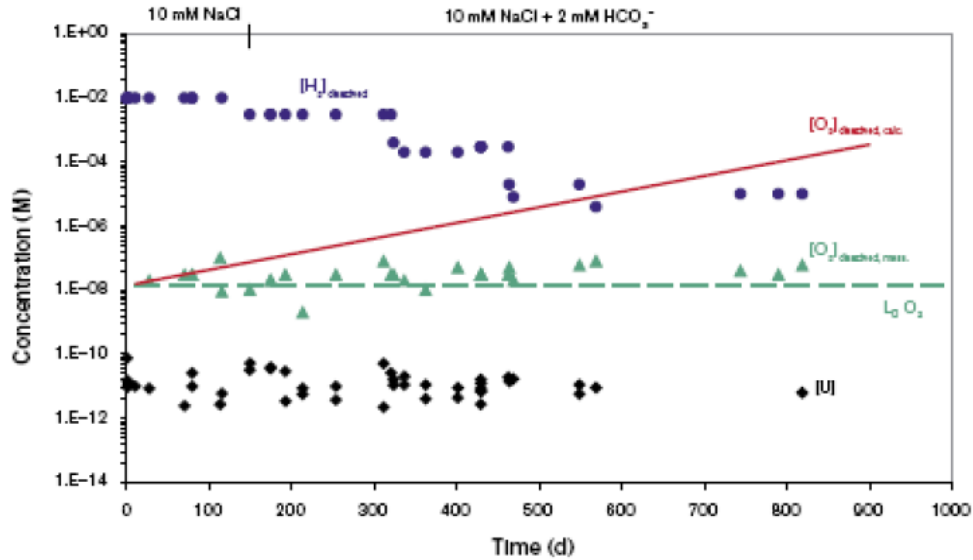
Figure 45: Measured H$_2$, O$_2$ and Total U Concentrations, As A Function of Time, in a Pressure Vessel Leaching Experiment Using A 10% ^{233}U-doped UO$_2$ in 10^{-2} mol/L NaCl (0 to 114 Days) and 10^{-2} mol/L NaCl + 10^{-2} mol/L HCO$_3^-$ (114 Days Onwards) As the H$_2$ Overpressure Was Periodically Reduced. The Red Line Shows the Calculated Radiolytic O$_2$ Concentrations Assuming it was not consumed (Carbol et al. 2005)

If the experimental system was sealed and the H$_2$ pressure not maintained, allowing H$_2$ to be depleted by the oxidant scavenging process, the initial suppression of U release was overcome by the re-establishment of α-radiolytic corrosion.

In experiments conducted using UO$_2$ containing a 10% fraction of ^{233}U (simulating the α-activity expected after 3000 years) (Carbol et al. 2009b) in 10^{-2} mol/L NaCl + 2 x 10^{-2} mol/L HCO$_3^-$ solution (pH = 8.4) pressurized with 16 bars of H$_2$ ([H$_2$] = 10^{-2} mol/L), the [U] decreased over the 328 day exposure period to < 10^{-11} mol/L, which is well below the levels achieved in the shorter experiments described above (Muzeau et al. 2009). When the [H$_2$] was periodically reduced (from 10^{-2} mol/L to 10^{-5} mol/L), no increase in U release rate was observed despite E$_h$ measurements indicating the re-establishment of solution oxidizing conditions. That the surface was in the fully reduced state (U^{IV}O$_2$) was demonstrated by XPS.

While consistent with the earlier results of Carbol et al. (2005), these observations (Carbol et al. 2009b) appear inconsistent with those of Muzeau et al. (2009) who did observe a revival of α-radiolytic oxidation when the [H$_2$] was decreased. A possible explanation is offered by SEM observations (Carbol et al. 2009b) which show a minor but clear restructuring of the UO$_2$ surface. It was suggested this could be an indication of an H$^\bullet$ radical-induced recrystallization of the UO$_2$ surface, a feature which could account for the extremely low [U] observed in long term experiments (Figure 45) which are 30 times lower than the solubility measured for amorphous UO$_2$ (Guillamont 2020; Rai et al. 2003; Parks and Pohl 1988). As noted in Section 6.2.1 on spent fuel, this process has the potential to reduce the UO$_2$ matrix solubility leading to the consumption of initially released U as a lower solubility equilibrium is established.
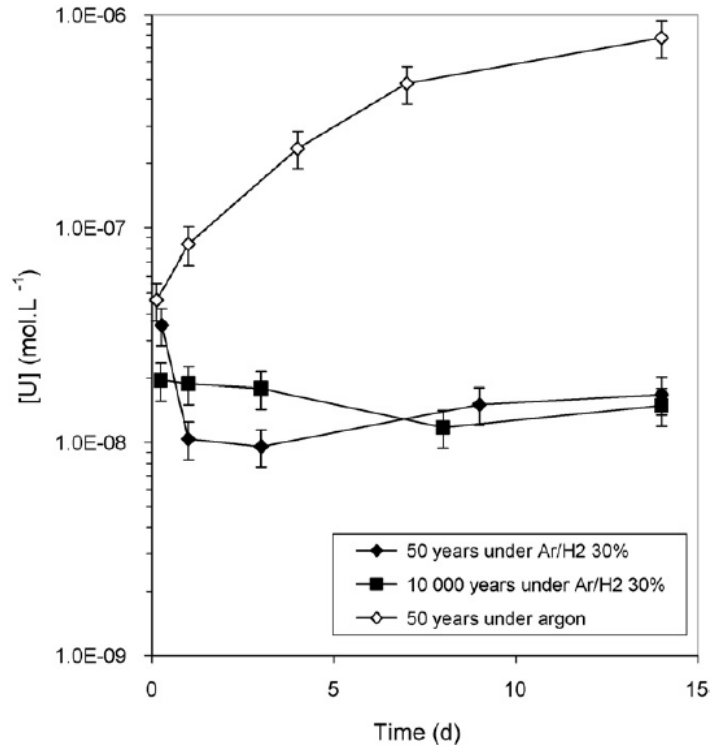
Figure 46: Uranium Release during Leaching of "50 Year Old" and "10,000 Year Old" $^{238/239}$Pu-doped UO_2 in a 10^{-3} mol/L HCO_3^- Solution Purged with Ar/30% H_2 (P_{tot} = 3.5 Bar) Compared to Uranium Releases for "50 Year Old" Doped UO_2 in the Same Solution Purged with Ar

6.2.3   External Alpha Sources

Experiments using external α-sources have also been performed. Wren et al. (2005) and Sunder et al. (1990) studied α-radiolysis on UO_2 using a ^{241}Am source in H_2O at room temperature and 100 ºC, respectively. In these experiments the α-sources irradiated a 30 μm thick layer of H_2O (Sunder et al. 1990) or 0.1 mol/L $NaClO_4$ solution between the α-source and a UO_2 disc. A slower than expected increase in E_{CORR} (Wren 2005) was attributed to a retarding effect of radiolytically-produced H_2 on the corrosion process, but no supporting analytical evidence was offered. In the study at 100 ºC (Sunder et al. 1990), XPS was used to demonstrate a clear reduction of the extent of surface oxidation (as U^{VI}) compared to that observed in the absence of H_2. In a more thorough study employing a similar experimental arrangement with sources with α-activities of 1.85 and 3.30 MBq, Hansson et al. (2021) demonstrated that the oxidation sequence, $U^{IV}O_2 \rightarrow U^{IV}_{1-2x}U^{V}_{2x}O_{2+x} \rightarrow U^{VI}O_2^{2+}$, was significantly retarded in the presence of H_2 with XPS measurements indicating only minor to negligible U^V content in the UO_2 surfaces. Inductively coupled plasma mass spectrometry (ICP-MS) showed an order of magnitude decrease in the release of U to solution compared to measurements conducted in the absence of H_2.

6.2.4 The Activation of Hydrogen by Radiation

It is clear from the studies described in Sections 6.2.1 and 6.2.2 that dissolved H_2 can reduce the concentrations of radiolytic oxidants to levels below their analytical detection limit, even though molecular H_2 is well known to be unreactive at the low temperatures employed. To act as a reductant, H_2 must be activated by dissociation into reactive $H^\bullet$.

$$OH^\bullet + H_2 \rightarrow H_2O + H^\bullet \tag{40}$$
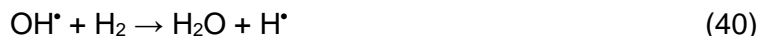
The homogeneous activation of H_2 by γ-radiation has been demonstrated experimentally by Pastina et al. (1999) and Pastina and LaVerne (2001), and a $[H_2]$ in the range found to suppress fuel corrosion (10^{-4} to 10^{-5} mol/L) has been shown to scavenge molecular radiolytic oxidants to below detection limits as well as consume small amounts of added H_2O_2. It has also been shown that H_2 influences the α-radiolytic production of oxidants, to a degree dependent on the α-dose rate and the components of the solution, but cannot completely eliminate oxidant production (Trummer and Jonsson 2010) and, hence, cannot explain the complete suppression of radiolytic corrosion. Since α-radiation will be the dominant radiation source within a failed container, no argument can be made that the homogeneous solution scavenging of oxidants alone can completely suppress radiolytic corrosion.

Given the ability of H_2 to scavenge $OH^\bullet$ radicals in bulk solution, the scavenging of surface $OH^\bullet$ created by the dominant radiolytic oxidant, H_2O_2, would be the expected first reaction step preventing the onset of UO_2 oxidation leading eventually to the release of $U^{VI}O_2^{2+}$ to solution or the decomposition of H_2O_2 to O_2 and H_2O (reactions 26-28). Since U release is completely suppressed and no O_2 is detected in reactions in the presence of γ- or α-radiation, reaction 41 would be the dominant reaction pathway.

$$(OH^\bullet)_{ads} + (H^\bullet)_{ads} \rightarrow H_2O \tag{41}$$

Measurements of the influence of H_2 on UO_2 corrosion under anoxic conditions in the presence of a γ-radiation field (15.9 to 11.3 Gy/h over the duration of the sequence of experiments) and a 5 MPa pressure of H_2 ($[H_2] \sim 4 \times 10^{-3}$ mol/L) have been conducted (King et al. 1999; King and Shoesmith 2004; Liu et al. 2021). A comparison of E_{CORR} values obtained in the presence of Ar or H_2 alone (unirradiated) to those measured in Ar with γ-radiation (Ar + γ) and H_2 with γ-radiation (H_2 + γ) shows significant effects of irradiation in the presence of H_2 (Figure 47). In this figure, only representative values are shown with the range of repeated measurements indicated by the coloured bars. In these experiments, any air-formed oxides were removed electrochemically, and E_{CORR} measurements subsequently recorded under controlled anoxic conditions. In unirradiated solutions, E_{CORR} values recorded under either Ar or H_2-sparged conditions were effectively identical and clustered around the thermodynamic threshold for the oxidation of the $U^{IV}O_2$ matrix in carbonate-free solution indicating minimal oxidation (Liu et al. 2021). In the presence of radiation (Ar + γ), E_{CORR} achieved steady-state in the range -0.35 V to -0.27 V (vs SCE) confirming the occurrence of radiolytic oxidation of the surface. Within this potential range, H_2O_2 decomposition catalyzed by the reversible interconversion of U^{IV}/U^V surface sites would be expected, as discussed in Section 5.10.

When H_2 and radiation were both present (H_2 + γ), the initial increase in E_{CORR} (after switching off the negative applied potential required to reduce the air-formed surface oxide) and the form of the E_{CORR} transient suggests an initially rapid oxidation, as radiolytic $OH^\bullet$ species oxidize the

UO_2 surface followed by a decrease in E_{CORR} as surface oxidation was suppressed and the surface reduced. The very low values, well below the thermodynamic threshold for UO_2 oxidation, suggest the UO_2 surface was reduced to sub-stoichiometric levels. In experiments in which the purge gas was switched between Ar and H_2 (in the presence of radiation), this process was demonstrated to be reversible as shown in Figure 48. However, E_{CORR} did not recover to the potential defined by the thermodynamic threshold suggesting an irreversible H_2-γ induced change in surface properties as apparently observed in spent fuel (Section 6.2.1) and α-doped UO_2 experiments (Section 6.2.2).
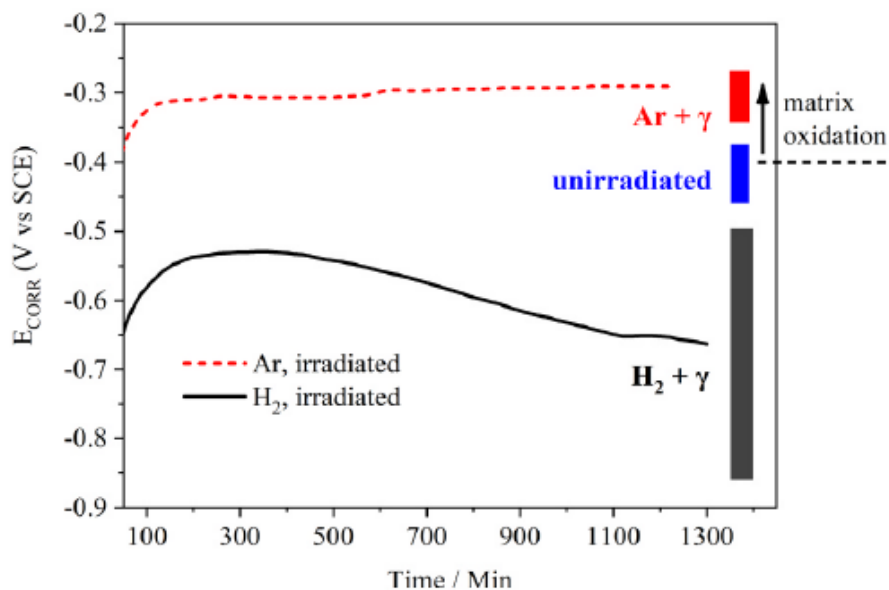
Figure 47: Corrosion Potentials (E_{CORR}) Measured on UO_2 (from A CANDU Pellet) in the Absence and Presence of γ-radiation in a 0.1 mol/L NaCl Solution at Room Temperature in the Presence of Either Ar or 5.2 MPa H_2. The Range of Final E_{CORR} Values in Repeated Experiments Are Shown as Black, Red, and Blue Vertical Bars

Based on these results, experiments in which electrochemically formed H$^{\bullet}$ radicals were shown to reduce U^V states in $U^{IV}_{1-2x}U^V_{2x}O_{2+x}$, and photoelectrochemical experiments demonstrating the H-doping of UO_2 by H atoms (Shoesmith et al. 1994), it was claimed that the combination of H_2 + γ leads to the transport of radiolytically-formed H$^{\bullet}$ into the UO_2 matrix leading to the reduction of U^V and the conversion of H$^{\bullet}$ to H$^+$ (Figure 49). It is also possible, though not indicated in the figure, that further reduction to U^{III} occurred. The reduction of U^V species would suppress formation of the catalytic $U^{IV}_{1-2x}U^V_{2x}O_{2+x}$ surface layer which would inhibit the decomposition of H_2O_2 (reactions 26-28) and the formation of U^{VI} leading to dissolution. The transport of H$^{\bullet}$/H$^+$ to subsurface levels suggests a possible irreversible effect on the UO_2 matrix rendering it less reactive when H_2 is subsequently removed, as observed in long-term spent fuel and α-doped UO_2 experiments (Section 6.2). No convincing explanation for this effect presently exists.
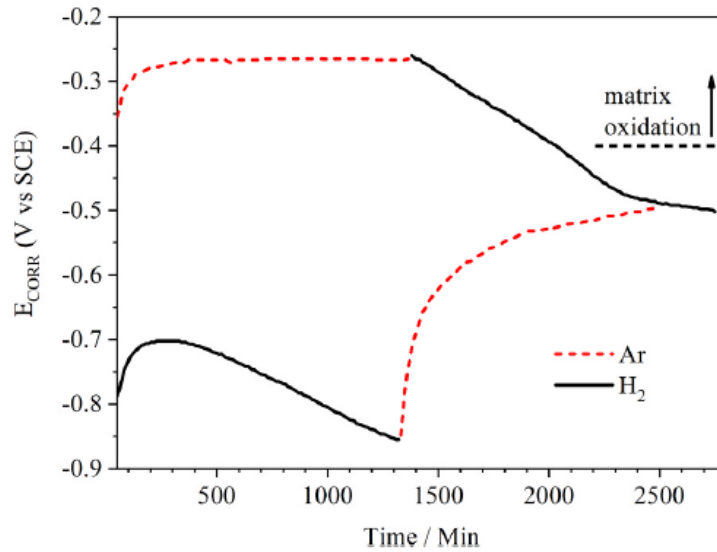
Figure 48: The Evolution in E_{CORR} on UO$_2$ (from A CANDU Pellet) When the Pressurizing Gas Was Changed Between Ar and H$_2$ in γ-irradiated 0.1 mol/L NaCl Solution at Room Temperature
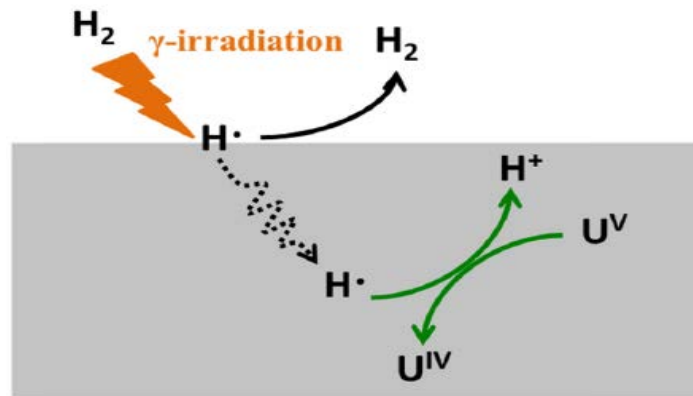
Figure 49: Schematic Illustration Showing A Possible Mechanism for the Activation of H$_2$ by γ-radiation Leading to the Reduction of U^V States Within the UO$_2$ Matrix

While these studies (King et al. 1999; King and Shoesmith 2004; Liu et al. 2021) demonstrate the direct chemical influence of γ-radiation in the presence of H$_2$, it does not address the physical effects of ionizing radiation on the properties of UO$_2$ which have been recently described and discussed by Pastina and LaVerne (2021). Ionizing radiation is known to create electronic defects by promoting electrons to the conduction band and excited states such as polarons or excitons (bound excited states of electrons and holes) and phonons (vibrating atoms in a crystalline structure). In the case of α-particle emission, a significant density of Frenkel defects is created by the displacement of O atoms to form interstitial-vacancy pairs

within the matrix. Mohun et al. (2018) have proposed that such α-induced irradiation defects could be involved in surface chemical reactions.

As discussed by Pastina and LaVerne (2021), physical defects of this nature, most commonly O_V, can lead to "excess" H_2 production on UO_2 surfaces due to the decomposition of H_2O when limited amounts of surface H_2O are available, a feasible situation on spent fuel surfaces within a failed container partially filled with groundwater. First principles studies (Wang et al. 2019) confirm the formation of H_2 is energetically favourable with the OH^- released eliminating the vacancy. It is also possible that the recoil atom produced by α-emission from the fuel surface, like Ar and heavy ion sputtering of UO_2 surfaces (Senanayake et al. 2007; Stultz et al. 2004, Bruno and Spahiu 2014), will produce surface defects by the preferential ejection of the much lighter O atom, a process which would create an O_V. The subsequent neutralization of such a defect would lead to the surface catalyzed dissociation of H_2O to yield $OH^•$ and $H^•$ and the formation of an additional $H^•$ when $OH^•$ is scavenged by available H_2 via reaction 40. This cycle of radiation-induced defect generation - elimination could continue as long as α-radiation fields remained meaningful.

That α-active surfaces can induce surface redox chemical effects has been demonstrated in studies showing the recombination of H_2 and O_2 on $^{239}PuO_2$ surfaces at 25 ^oC (Haschke et al. 1996). In addition, radiolytic H_2 generation via the decomposition of H_2O on NpO_2 (doped with the α-emitter ^{244}Cm) achieves a steady-state indicative of a balance between H_2O decomposition and the reverse H_2/O_2 recombination process. Presently, the influence of these physical effects on the formation of O_I during oxidation and the injection of $H^•$ during reduction remains unquantified.

6.2.5   The Activation of Hydrogen by Noble Metal (ε) Particles

A second pathway exists for the activation of H_2 on spent nuclear fuel surfaces. The wide range of fission products generated during in-reactor operation leads to two key features which influence fuel reactivity as discussed in Section 3: (i) the rare earths (e.g., Nd, Eu, Gd) dope the UO_2 lattice as RE^{III} cations leading to an increase in both matrix stability and electrical conductivity; and (ii) the separation of noble metals (Mo, Ru, Pd, Rh, Tc) into alloy particles known as ε-particles.

Noble metals are well known catalysts for oxidation/reduction reactions, especially the $H_2/H^•/H^+$ reaction, with 3 of the 5 dominant components of ε-particles (Pd, Rh, Ru) possessing high exchange currents (Pd – 10^{-3} A·cm^{-2}: Rh – $10^{-3.6}$ A·cm^{-2}: Ru – $10^{-3.3}$ A·cm^{-2}) for the interconversion of H^+ and H_2 (Norskov et al. 2005). This leads to a conductive matrix of reduced reactivity within which exists a network of potential catalysts for surface redox reactions. Thus, it would be expected that ε-particles (despite their low surface coverage) could act as galvanically-coupled anodes (for H_2 oxidation) and cathodes (for H_2O_2/O_2 reduction). As discussed in Section 5.9, neither RE^{III} lattice doping nor the presence of ε-particles leads to a significant acceleration of H_2O_2 reduction which can create its own U^{IV}/U^V catalytic sites on UO_2 surfaces. However, H_2 activation on ε-particles will produce $H^•$ which would be expected to drive the recombination of H_2O_2 and H_2 on ε-particle surfaces by reaction with surface $OH^•$ species, reaction 41.

The influence of these particles on fuel behaviour in the presence of H_2 has been studied on SIMFUELs (Broczkowski et al. 2005, 2006, 2007, 2010, 2011; Razdan and Shoesmith 2015), on UO_2 in the presence of noble metals (Nilsson and Jonsson 2007, 2008; Nilsson 2008) and on

particles extracted from actual spent fuel specimens (Cui et al. 2010). Figure 50 shows the distribution of ε-particles for three SIMFUELs with various degrees of simulated burn-up covering the range from the level expected in CANDU fuel (1.5 at%) to that expected for a low burn-up enriched fuel (6 at%).
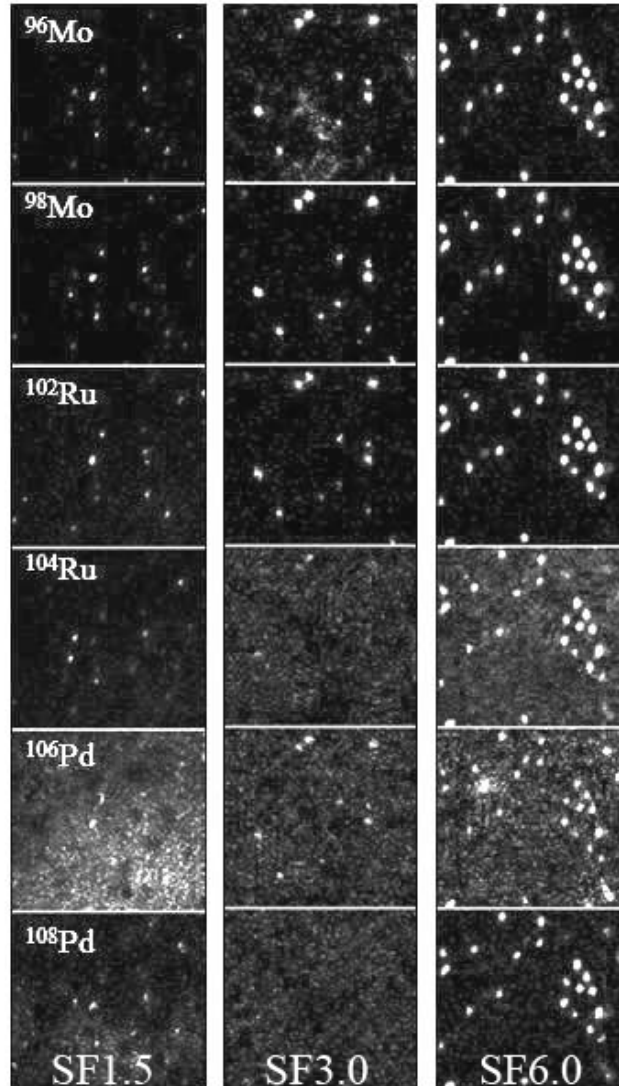
Figure 50: SIMS Images Showing the Elements ^{96,98}Mo, ^{102,104}Ru and ^{106,108}Pd in Three SIMFUELs with Different Degrees of Simulated Burnup (Expressed As at%). The Particles Also Contain Small Amounts of Rh. Each Individual Analyzed Area Is 50 x 50 μm

This distribution was obtained from SIMS analyses for the individual elements in the particles. The increase in size and number density of particles with the increase in degree of simulated burn-up is clear. In general, the particles are larger than those observed in actual spent fuel (Cui et al. 2010). Figure 51 shows the E_{CORR} measured on 1.5 at% SIMFUEL is very sensitive to

the solution redox condition with both O_2 and H_2 causing distinct changes compared to the value recorded under anoxic conditions (Ar).
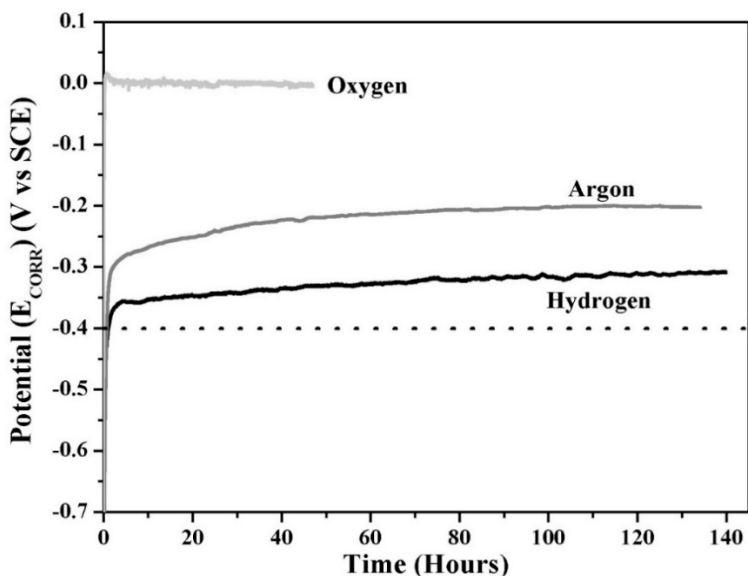
Figure 51: Corrosion Potential (E_{CORR}) Measurements on A SIMFUEL (1.5 at%) in A 0.1 mol/L KCL Solution (pH = 9.5) Purged with Either O_2, Ar or 5%H_2/Ar at 60 $^{\circ}$C. The Electrode Was Electrochemically-cleaned Prior to the Start of Each Experiment. The Dashed Line Shows the Potential Threshold Below Which the Corrosion of UO$_2$ Should Not Occur

As noted in Section 5.9, O_2 reduction is catalyzed on ε-particles. Even in the presence of small amounts of dissolved H_2 ([H_2] $\sim$ 10^{-4} mol/L: purge gas 5% H_2 / 95% Ar), E_{CORR} is suppressed well below the value measured in anoxic conditions (Ar) even for a low density of ε-particles. When a similar measurement was conducted on a SIMFUEL containing no ε-particles, E_{CORR} was the same for both Ar/H_2 and Ar purged conditions.

The value of E_{CORR} decreased with the number density of ε-particles with the value for 6 at% SIMFUEL reaching the thermodynamic threshold ($\sim$ -0.4 V vs SCE) below which corrosion of UO$_2$ should not occur. The ability of H_2 oxidation on ε-particles to suppress oxidation of the UO$_2$ matrix has been demonstrated by XPS as shown in Figure 52. This figure compares the compositions of surfaces exposed to either O_2, Ar or H_2 purged solutions, expressed as the fractions of U^{IV}/U^{V}/U^{VI} as a function of E_{CORR} for all 3 SIMFUELs and a SIMFUEL containing no ε-particles, to compositional calibration plots determined in electrochemical experiments (Santos et al. 2004). As the number of ε-particles increases (Figure 53, A $\rightarrow$ B $\rightarrow$ C) and E_{CORR} measured with Ar/H_2 purging decreases, the extent of surface oxidation decreases achieving the thermodynamic threshold for 6 at% SIMFUEL. Also noteworthy is the inability of H_2 to suppress the surface oxidation state in the absence of ε-particles.

When the H_2 pressure was increased towards the values anticipated under DGR conditions, E_{CORR} was suppressed to values well below the thermodynamic threshold (Figure 53), with the potential achieved under these conditions approaching the reversible potential for the H_2/H^+

reaction (-0.86 V vs SCE (King and Shoesmith 2004)) as observed on UO₂ containing no ε-particles in the presence of γ-radiation (Figure 54) (Liu et al. 2021).
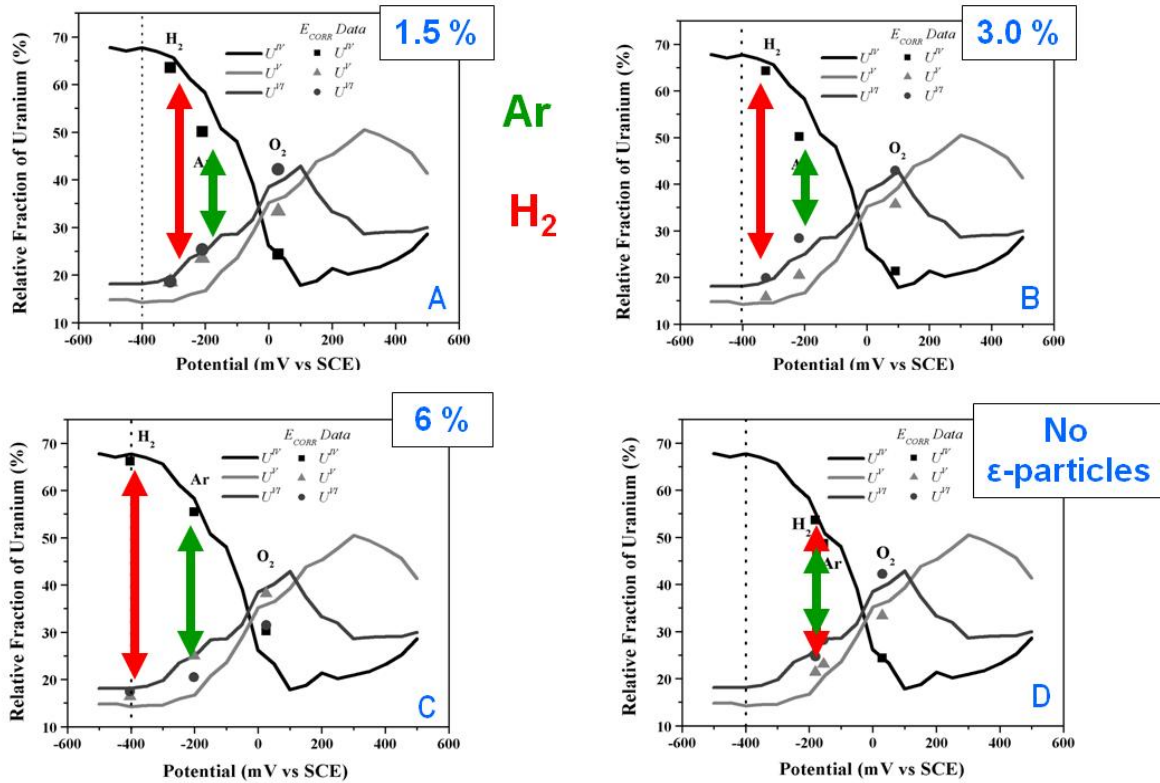
Figure 52: Relative Surface Fractions of U^{IV}, U^{V}, U^{VI} Obtained by XPS As a Function of the Steady-state E$_{CORR}$ Achieved in 0.1 mol/L KCl (pH = 9.5) Solution Purged with Either O₂, Ar, or 5% H₂/Ar for SIMFUELS with Different Degrees of Simulated Burn-up. A Set of Data Recorded on a SIMFUEL Containing No ε-particles is Also Shown. The Values Are Superimposed on a Plot Showing the Surface Composition of a 1.5 at% SIMFUEL Electrochemically Oxidized at Individual Potentials (from Figure 12). The Vertical Arrows Indicate the Differences in U^{IV}/U^{V} Percentages at the E$_{CORR}$ Values Measured in the Presence of Ar and H₂, Respectively. Their Separation on the Potential Scale is a Measure of the Influence of H₂. The Vertical Dashed Line Indicates the Threshold for UO₂ Oxidation
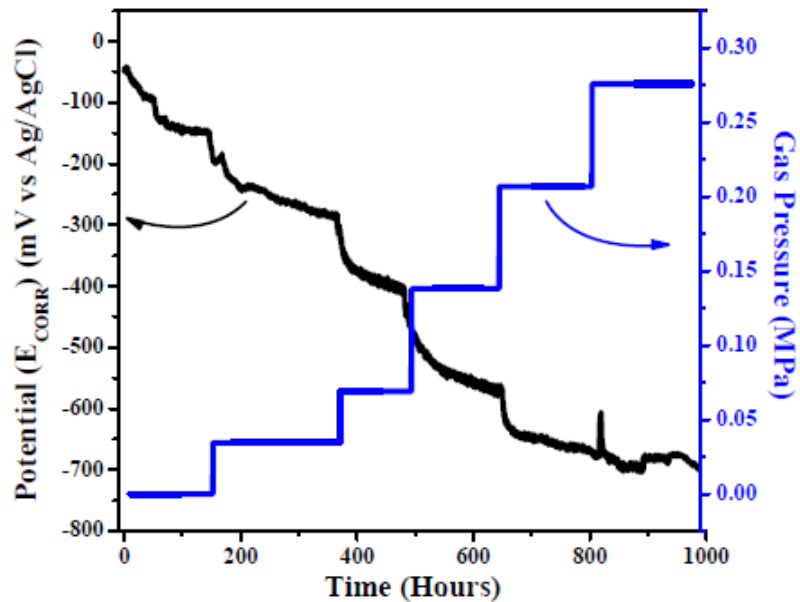
Figure 53: The Influence of H$_2$ Solution Overpressure on the E$_{CORR}$ of a 1.5 at% SIMFUEL Measured in 0.1 mol/L KCl Solution (pH = 9.5) at 60 °C. The System Was Initially Purged with Ar Only at Atmospheric Pressure and Then a Series of Increasing 5% H$_2$/Ar Pressures
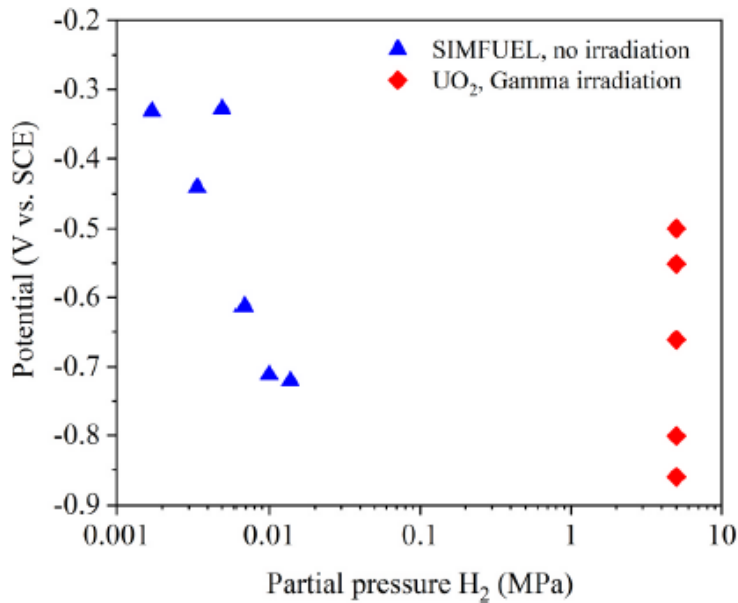
Figure 54: The Influence of the Partial Pressure of H$_2$ on Corrosion Potential (E$_{CORR}$) Values Recorded on SIMFUEL (from Figure 53) Compared to the Range of E$_{CORR}$ Values Measured on UO$_2$ in the Presence of γ-irradiation (the Range of H$_2$ + γ Values in Figure 47)

On both SIMFUEL and UO_2, the $H_2/H^•/H^+$ reaction would be reversible, and the UO_2 matrix should be inert as appears to be the case for spent fuels and α-doped UO_2 (Sections 6.2.1 and 6.2.2). Whether the UO_2 surface becomes reduced to include U^{III} states, as suggested above for the influence of γ-radiation (Section 6.2.4) remains unresolved. That H_2 cannot be activated, or activated only to a minor degree, on SIMFUEL not containing ε-particles is confirmed in a similar experiment which yields much more positive values of E_{CORR} which decrease only slightly as the H_2 pressure is increased (Broczkowski 2008).

Since ε-particles (noble metal alloys) are catalytic for both the reduction of oxidants, such as H_2O_2, as well as the oxidation of the potential reductant H_2, it is not surprising that these particles also catalyze the recombination reaction between H_2O_2 and H_2 to produce H_2O. Nilsson and Jonsson (2008) showed that the noble metal Pd, present as a powder, acted as a catalyst for this reaction, which was shown to be diffusion controlled as expected for this metal. These observations are consistent with electrochemical results (Figure 55 and Figure 56), recorded on 1.5 at% SIMFUEL (Broczkowski et al. 2010; Razdan and Shoesmith 2015) in the presence of [H_2O_2] in the range expected from model calculations (10^{-10}-10^{-11} mol/L) (Wu et al. 2012) under DGR conditions and at relatively low [H_2].
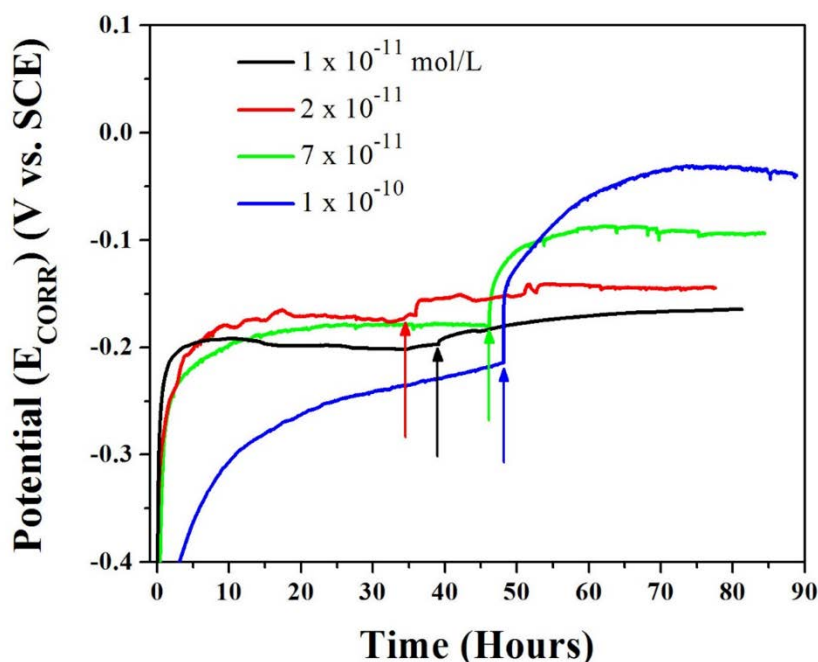
Figure 55: Corrosion Potentials (E_{CORR}) Recorded on 1.5 at% SIMFUEL in a 0.1 mol/L KCl Solution (pH = 9.5) Purged with Ar at 60 °C. The Arrows Indicate the Times at Which the Specified [H_2O_2] Was Added in the Individual Experiments.

In the absence of H_2, E_{CORR} established steady-state values which increased with [H_2O_2] (Figure 55), and XPS analyses confirmed that the extent of oxidation of the surface increased accordingly (Broczkowski et al. 2010). Similar [H_2O_2] added in the presence of H_2 initially stimulated an increase but eventually a decrease in E_{CORR} for a low enough [H_2O_2] (Figure 56).

The transient nature of the E_{CORR} response suggests a possible rapid oxidation on adding H_2O_2 followed by a slightly slower reduction process, the latter confirmed by XPS analyses.

Two pathways for protection against oxidation are possible as illustrated in Figure 57: either recombination by reaction on the ε-particles (Figure 57(a)), or H_2O_2 reduction on UO_2 driven by galvanic coupling to H_2 oxidation on ε-particles (Figure 57(b)). Since the reaction of H_2O_2 with UO_2 is rapid, the second pathway appears more likely given the much larger available UO_2 surface area. Similar experiments in which H_2O_2 was added to an Ar/H_2 purged solution containing a SIMFUEL with no ε-particles (Broczkowski et al. 2011) also generated E_{CORR} transients indicating the same oxidation (by H_2O_2)/reduction (by H_2) coupled reaction. Again, XPS analyses confirmed the reduced state of the surface when the transient was complete. These observations suggest that, while the recombination process may be accelerated by $H^•$ formation on ε-particles it can also occur on the UO_2 surface via the H_2 scavenging of the surface $OH^•$ radicals which would otherwise lead to UO_2 oxidation.
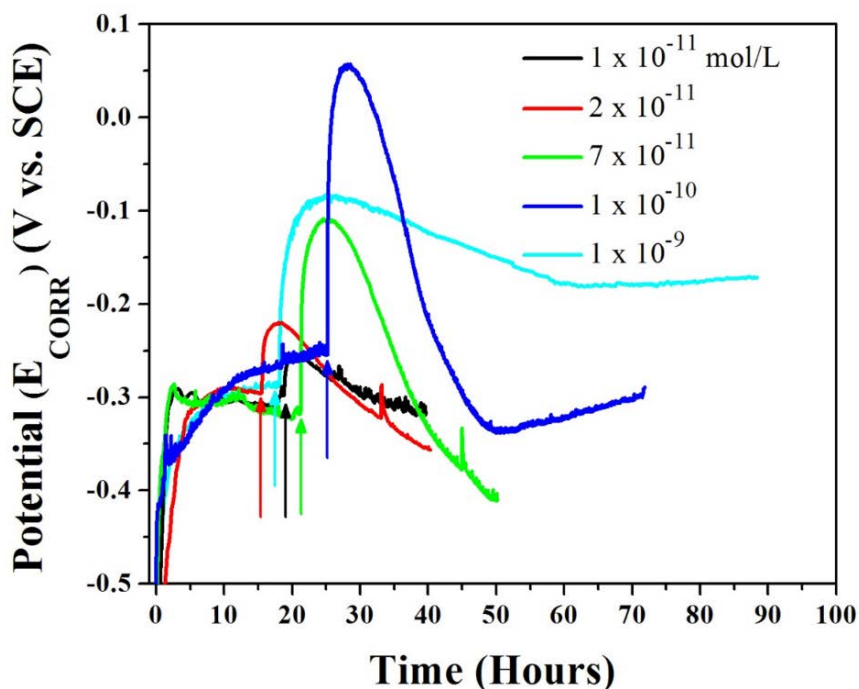
Figure 56: Corrosion Potential (E_{CORR}) Values Recorded on 1.5 at% SIMFUEL in a 0.1 mol/L KCl Solution (pH = 9.5) Purged with 5%H_2/Ar at 60 °C. The Arrows Indicate the Times the Specified [H_2O_2] Was Added in the Individual Experiments
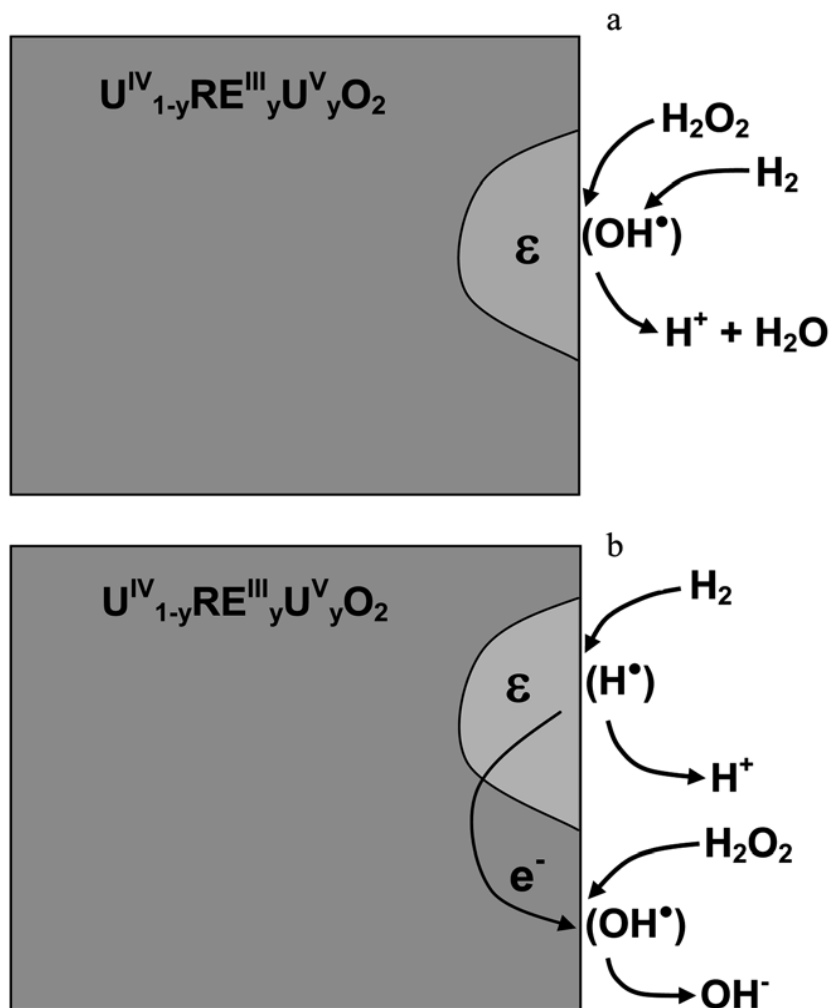
Figure 57: Schematic Illustrating the Possible Reaction Pathways for the Scavenging of H_2O_2 by Reaction with H_2 on a 1.5 at% SIMFUEL Surface: (a) by Reaction on ε-particles; (b) by H_2 Oxidation on ε-particles Galvanically Coupled to the Reduction of H_2O_2 on the Oxide Surface

That the reactions of H_2O_2 with UO_2 and with H_2 on UO_2 (and on other metal oxides) proceed via surface radical states (OH•) has been well established (Section 5.9). This was recently confirmed on SIMFUEL in D isotope studies (Bauhn et al. 2018) in NaCl/HCO$_3^-$ solutions in which the reaction of surface OH• on SIMFUEL surfaces with dissolved D_2 was demonstrated by detection of HDO.

$$D_2 + 2(OH•)_{surf} \rightarrow 2HDO \qquad (42)$$

By simultaneously measuring the amounts of U dissolved and H_2O_2 consumed, it was demonstrated that the majority of the H_2O_2 (53-79%) was consumed by D_2 scavenging (reaction 42) with the majority of the remainder consumed by H_2O_2 decomposition and only 0.02% causing corrosion. Since the experiments were performed on SIMFUEL, the role of ε-particles is unclear, but, since OH• radicals are readily formed on UO_2 surfaces, their role is likely minor.

7. MODELLING FUEL CORROSION

In the absence of kinetic information on heterogeneous reactions involved in the UO_2 corrosion process, early attempts to model fuel corrosion either relied on rate constants and reaction schemes developed for homogeneous H_2O radiolysis (Christensen et al. 1994) or on the extrapolation of electrochemically measured dissolution currents to E_{CORR} values measured in various solutions (Shoesmith and Sunder 1991, 1992; Shoesmith 2000). The limitations and associated errors of adopting rate constants for homogeneous reactions to represent surface reaction rates have been pointed out by Eriksen et al. (2012), and the electrochemical approach has been extended in the development of more comprehensive and representative models as described below.

Models were developed in the European Spent Fuel Stability (Poissot et al. 2001) and MICADO (Grambow et al. 2010) projects, and the associated uncertainties have been discussed (Grambow et al. 2011). The models described are based generally on established H_2O radiolysis models coupled with interfacial reactions on the fuel surface and solution diffusive transport processes, with any attempt to incorporate the influence of H_2 limited to considerations of its influence on the H_2O radiolysis process.

Of these models, the Matrix Alteration Model (MAM) has been the most extensively developed (de Pablo et al. 1996, 1999, 2004; Merino et al. 2005) and tested against experiments conducted in O_2 and H_2O_2-containing solutions. The corrosion process was assumed to be controlled by surface adsorption kinetics in the case of O_2. The H_2O_2 reaction was taken to involve $OH^\bullet$ radicals and surface-catalyzed decomposition with rate constants determined by Ekeroth and Jonsson (2003) adopted in calculations based on the mechanism,

$$>UO_2 + H_2O_2 \rightarrow >UO_2 + 2(OH^\bullet)_{ads} \tag{43}$$

$$>UO_2 \ + \ OH^\bullet \rightarrow UO_2OH \tag{44}$$

$$>UO_2OH + OH^\bullet \rightarrow >UO_3 + H_2O \tag{45}$$
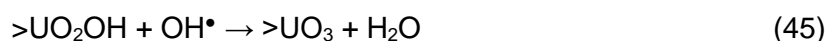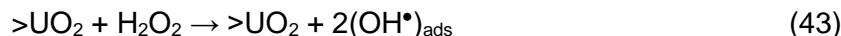
with reaction 45 being slow. The subsequent dissolution of the oxidized surface involved two reaction steps; surface coordination of U^{VI} by aqueous ligands (H^+, HCO_3^-, H_2O) followed by release of U^{VI}. In the presence of HCO_3^- the overall mechanism was assumed to proceed via the following steps,

$$>UO_3 + H^+ \rightarrow UO_2(OH)^+ \tag{46}$$

$$>UO_3 + H_2O \rightarrow UO_2(OH)_{2(aq)} \tag{47}$$

$$>UO_3 + HCO_3^- \rightarrow UO_2CO_{3(aq)} \tag{48}$$

This mechanism was found capable of predicting radiolytic dissolution rates.

Calculations by Nielsen et al. (2008) and Nielsen and Jonsson (2008) based on a model including (a) radiolytic production of H_2O_2, its consumption by homogeneous and heterogeneous reactions, and (b) diffusive transport showed that the steady-state surface concentration profiles were rapidly achieved at a value dictated by the radiation dose rate. This

indicates the corrosion rate will be controlled by the radiolytic production of H_2O_2 (the radiation dose rate) not by the interfacial kinetics of the reactions involved. When tested against experimental data, calculated and measured corrosion rates were in good agreement.

Based on these early models and the databases accumulated for the possible interfacial reactions, two different approaches were adopted to model fuel corrosion within a failed waste container (Eriksen et al. 2012). Both approaches involve the development of reaction-diffusion models interlinking the two corrosion fronts that will exist within a failed container (Figure 11 and Figure 42). In the first approach, the interfacial boundary conditions are expressed in chemical kinetic terms involving reactant concentrations, rate constants and reaction orders, with the rate corrected for the surface area to solution volume ratio for reactions involving the surface and soluble species. In the second approach involving electrochemical boundary conditions, electrochemical kinetic equations were used with the current for the anodic reactions (UO_2, H_2O_2, H_2 oxidation) equal and opposite in sign to the current for the cathodic oxidant reactions (O_2, H_2O_2, H_2O) at the E_{CORR}. The rate constants for electrochemical reactions are exponentially dependent on potential and commonly expressed as exchange currents, as discussed in more detail in Eriksen et al. (2012). If necessary, the rate of an electrochemical reaction, determined as a current, can be expressed in chemical terms using Faradays law.

The initial electrochemical model, the mixed potential model (MPM), was developed by Shoesmith et al. (1998, 2003) and King and Kolar (1999, 2002, 2003) based on the reaction scheme illustrated in Figure 58. A range of different processes are included in the model: diffusive transport, adsorption/desorption, precipitation/dissolution, homogeneous redox reactions between various oxidants and reductants, and the interfacial reactions on the UO_2 and steel surfaces which define the boundaries of the physical model. The Zircaloy fuel cladding is assumed to provide no barrier to fuel corrosion and to be chemically inert. Corrosion on the fuel surface is described by anodic dissolution processes (as UO_2^{2+} and $UO_2(CO_3)_2^{2-}$) supported by cathodic reduction of O_2 and H_2O_2, where H_2O_2 is the primary product of α-radiolysis and, O_2 is formed by H_2O_2 decomposition catalyzed by the fuel surface.

The rate of formation of H_2O_2 is calculated from the α-dose rate as a function of time using a similar, but earlier, calculated profile to that shown in Figure 10. It is assumed that any corrosion product deposit formed on the fuel surface can retain, by precipitation, α-emitters released by corrosion of the fuel matrix. This makes it necessary to account for irradiation along the length of the pores as well as at the exposed fuel surface at the base of the pores. A schematic of this situation is shown in Figure 59. The source of the parameters used in the model, and the approximations and accommodations required in the use of available kinetic data, are discussed in Shoesmith and King (1998). Since the model does not include the influence of H_2, corrosion is predicted to proceed for ~ 9000 years, the period corresponding to the highest α-dose rate at the fuel surface. According to the model, ~ 25% of the fuel would react over 10^6 years. For the aggressive conditions considered, H_2O_2 decomposition is predicted to be negligible, a conclusion at odds with more recent experiments and analyses (Section 5.10).
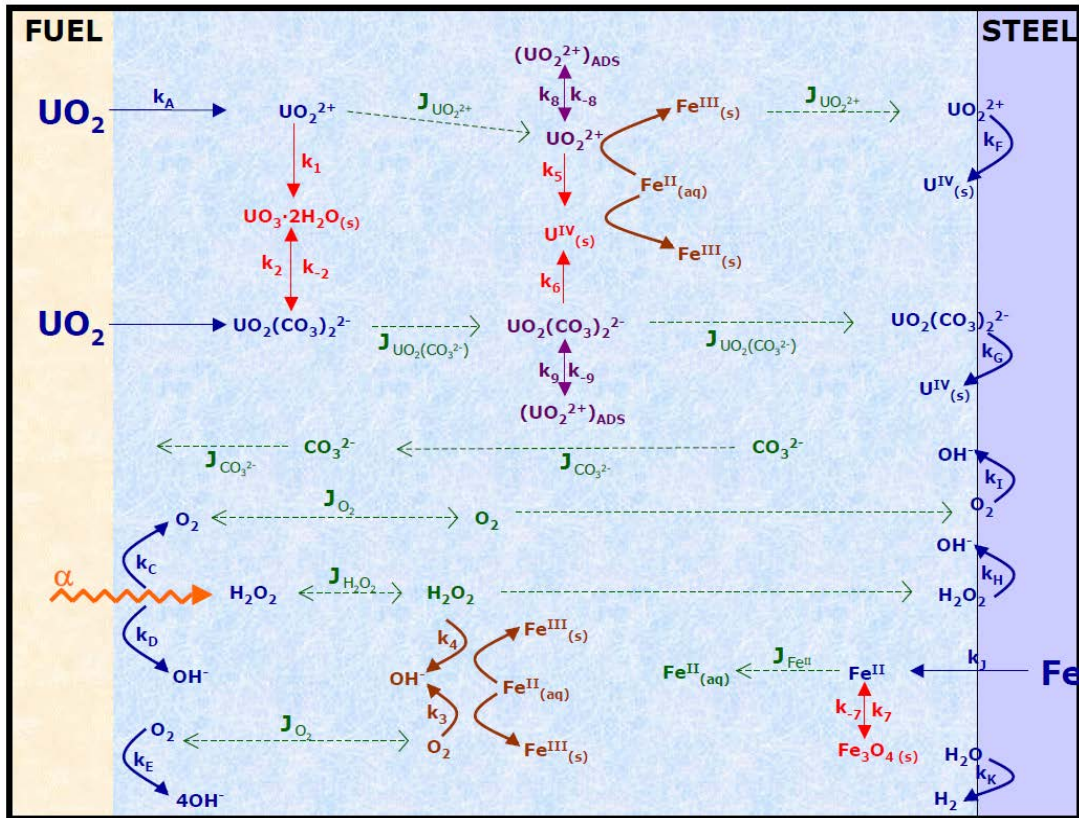
Figure 58: The Reaction Scheme Used in the Mixed Potential Model (MPM), Showing the Interfacial Electrochemical, Diffusive Transport, Adsorption/Desorption, Precipitation/Dissolution, and Homogeneous Solution Reactions Incorporated in the Model

An updated mixed potential model, the Fuel Matrix Dissolution Model (FMDM) based on a similar but extended database to that used in the MPM was developed by Jerden et al. (2015). The FMDM is a one dimensional, reaction-diffusion model incorporating a 10 cm diffusion path extending out from the spent fuel surface, with the opposite boundary defined by constant concentrations of species such as H_2 produced by steel corrosion. A similar approach to the accumulation of corrosion product deposits to that used in the MPM was adopted, but without the redistribution of the α-radiation due to the incorporation of α-emitters into the accumulating deposit. The reaction scheme and model lay out, indicating the current paths for coupled electrochemical reactions are shown in Figure 60.
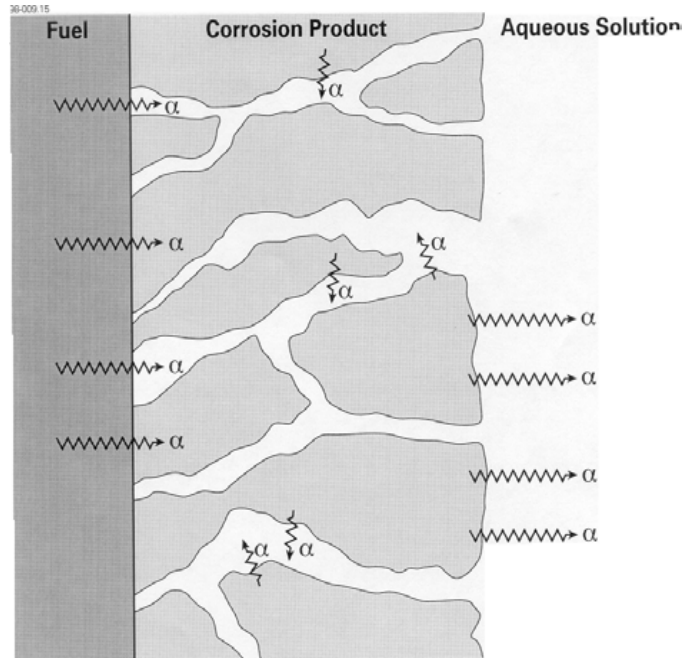
Figure 59: Schematic of the Corrosion Product Layer on the Corroding Fuel Surface Illustrating the Continuous Connected Pore Structure and the α-irradiation of H₂O Within the Pores by α-emitters in the Fuel and Incorporated into the Layer
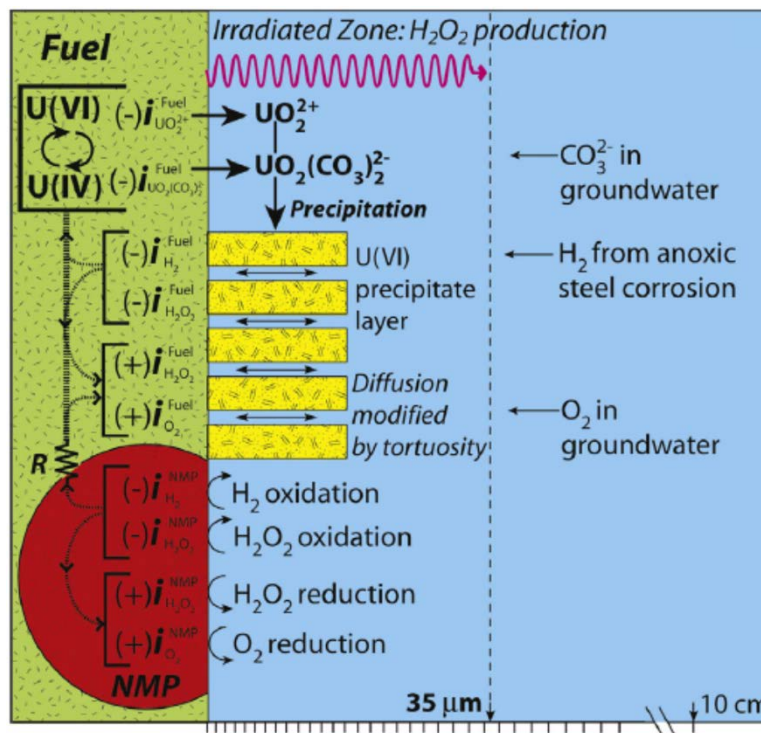
Figure 60: Summary of the Fuel Matrix Dissolution Model (FMDM) Reaction Current Paths and Model layout

The major advance over the MPM is the incorporation of the kinetics of reactions involving H_2 on both the UO_2 and ε-particle (NMP) surfaces and the inclusion of a chemical dissolution step for anoxic dissolution

$$UO_2 + 2H_2O \rightarrow U(OH)_4 \qquad (49)$$

with a rate constant for the latter reaction taken from Bruno et al. (1991). The reaction scheme is shown in Figure 61. Three mechanisms, consistent with those described in Section 5, are incorporated: (i) the homogeneous scavenging of radiolytically produced H_2O_2 in solution; (ii) the catalytic activation of H_2 (in the presence of α-radiation) by the OH$^\bullet$ radicals formed by H_2O_2 dissociation on the UO_2 surface (reaction 26); and (iii) similar radical interactions on the ε-particles (NMP). While a number of arbitrary assumptions are inevitably involved, the model reproduces the key trends observed experimentally, and predicts that the oxidation of H_2 at a $[H_2]$ of 10^{-3} mol/L on the UO_2 surface leads to a decrease in corrosion rate by 4 to 5 orders of magnitude compared to the rate expected if H_2 effects are ignored.

A similar model analyzing the influence of H_2 on fuel corrosion inside a failed container has been developed based on chemical, as opposed to electrochemical, boundary conditions (Wu et al. 2012, 2014b, 2014c; Liu et al. 2016, 2017c, 2019). The 1-dimensional form of the model is illustrated in Figure 62, and includes the following reactions: (i) the production of H_2O_2 and H_2 by radiolysis (reaction 1 in the Figure); (ii) corrosion supported by the reduction of H_2O_2 on the UO_2 surface (reaction 2a in the Figure) and on the ε-particles (reaction 2b in the Figure); (iii) the reduction of oxidized surface species (U^V and U^{VI}) by H_2 oxidation on ε-particles galvanically-coupled to the UO_2 matrix (reaction 3a in the Figure), dissolved UO_2^{2+} by H_2 in solution (reaction 3b in the Figure), and of adsorbed UO_2^{2+} by H_2 activated on ε-particles (reaction 3c in the Figure); (iv) the consumption of H_2O_2 by reaction with soluble Fe^{2+} (reaction 4 in the Figure); (v) surface reactions between H_2O_2 and H_2 catalyzed by ε-particles (reaction 5 in the Figure); and (vi) the decomposition of H_2O_2 to O_2 and H_2O at the $U^{IV}_{1-2x}U^V_{2x}O_{2+x}$ surface (reaction 6 in the Figure).
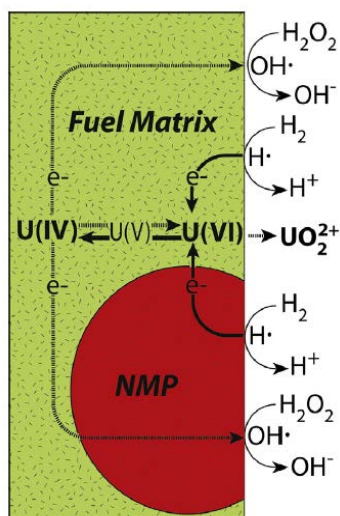
Figure 61: Schematic Illustration Summarizing the Flow of Electrons to and from Key Oxidation and Reduction Reactions Included in the Fuel Matrix Dissolution Model (FMDM). The ε-particle (NMP) is Shown as Galvanically-coupled to the Fuel Matrix
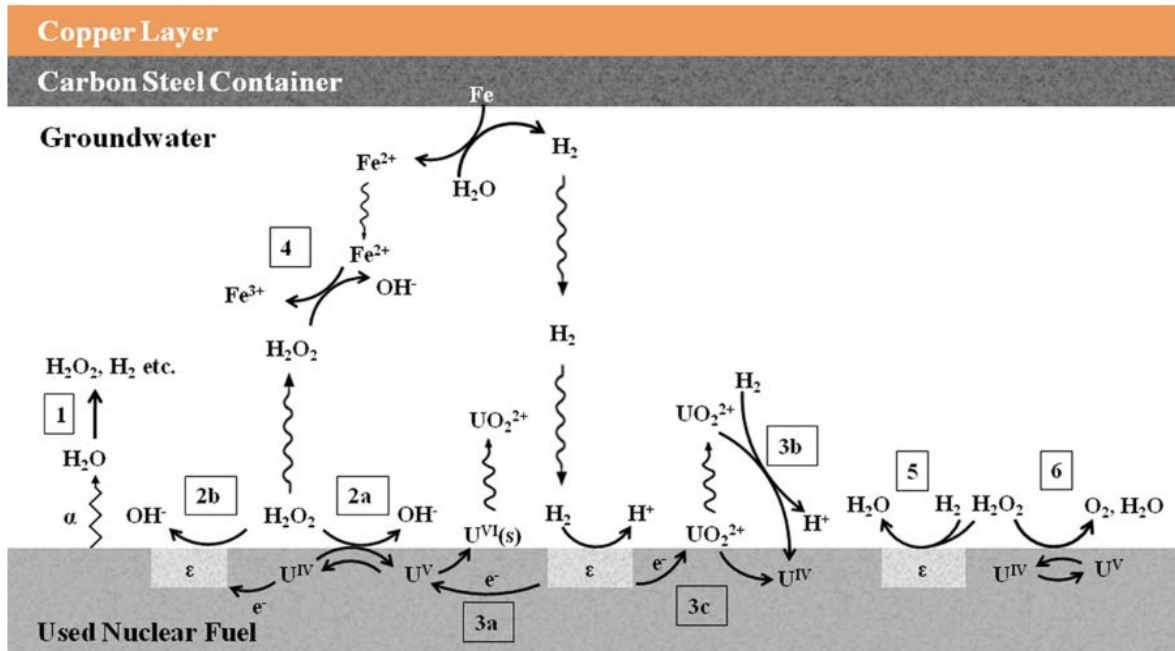
Figure 62: Schematic Illustration of the Reactions Included in the Model for the α-radiolytic Corrosion of Fuel Inside a Failed Waste Container (Liu et al. 2019)

Although not shown in Figure 62, these reactions proceed through radical species as illustrated in Figure 61. The values of the parameters used, and modelling assumptions made, are discussed in detail in Wu et al. (2012, 2014b). A model for steel corrosion is not included. Instead, the model adopts specific values of $[Fe^{2+}]$ and $[H_2]$ taken to be produced by steel corrosion at a boundary sufficiently distant from the fuel surface that concentration gradients are no longer feasible. This enables the model to test the concentrations of the two redox scavengers on fuel corrosion.

For the 1-D format it was demonstrated, as shown experimentally (Sections 6.1 and 6.2), that H_2 is the dominant scavenger, with Fe^{2+} exerting only a relatively minor role (Figure 43) consistent with the calculations using the FMDM model. Calculations show that the amount of H_2 required to completely suppress fuel corrosion is in the micromolar range even when the scavenging effect of Fe^{2+} is ignored. This point is emphasized in Figure 63 which shows the calculated $[H_2]_{crit}$ required to completely suppress fuel corrosion as a function of decay time for a reference CANDU fuel bundle. The required H_2 decreases markedly with time. The slight increase in H_2 required over the first 50 years reflects the accumulation of α-emitters as a consequence of the short-term γ/β decay of radionuclides within the fuel. At short times, when the demand is highest, the maximum amount of H_2 required for complete suppression, ignoring any influence of Fe^{2+}, is only ~ 0.4 µmol/L. Since groundwater $[H_2]$ in the range 800 to 4000 µmol/L (equivalent to an H_2 pressure range from 1 to 50 bar) are expected under DGR conditions, complete suppression of fuel corrosion is to be expected. This trend is consistent with that calculated by Jonsson et al. (2007), with their higher $[H_2]_{crit}$ reflecting the much higher burnup (~ 5 to 10 times) of Swedish LWR fuel compared to CANDU fuel.
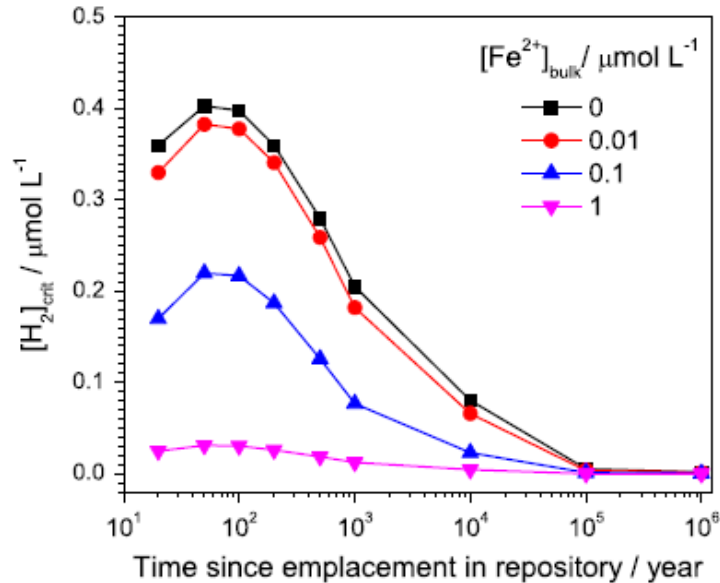
Figure 63: The Calculated [H₂]crit Required to Completely Suppress Fuel Corrosion as a Function of Time Since Emplacement in a DGR at Different [Fe²⁺]

Since spent fuel is heavily fractured and possesses a large number of fission gas bubbles/tunnels, especially along grain boundaries, there is a possibility that groundwater in a breached waste container will penetrate to locations within the fuel, a situation which could lead to the accumulation of radiolytic species at locations less accessible to the oxidant scavengers Fe^{2+} and H_2 from steel corrosion. To investigate the potential consequences of such a feature, the model was extended to 2-D as shown in Figure 64. Within the range of fracture geometries investigated, $[H_2]_{crit}$ (the amount of H_2 required for complete suppression of corrosion) never exceeds a maximum contribution from external H_2 (from steel corrosion as opposed to radiolytically-produced) of 2.4 µmol/L (Wu et al. 2014c; Liu et al. 2016). Calculations which separate the influences of external H_2 (from steel corrosion) and internal H_2 (produced radiolytically) show that the latter becomes more influential in suppressing corrosion in the narrower and deeper fractures when its escape by diffusive transport becomes more limited.

These calculations show that radiolytic H_2 produced by CANDU fuel (with the reference burn-up of 220 MWh/kgU) plays a key role in suppressing corrosion especially in tight locations where it can accumulate, and that, irrespective of the dimensions of fractures or faults in the fuel, complete suppression of corrosion can be achieved when only 5.7 µmol/L of H_2 is supplied by steel corrosion: i.e., only ~17 times as much H_2 from steel corrosion is required to completely suppress corrosion in fractures compared to the corrosion on the planar outer surface of the fuel (Liu et al. 2016). The effectiveness of such small $[H_2]$ is consistent with the results of experiments on spent fuel and α-doped UO_2 (Sections 6.2.1 and 6.2.2).

Figure 64: Model Arrangement Showing a Cross Section of the Fuel/Solution Interface for the Simulation of Radiolytic Corrosion Inside a Fracture in a Fuel Pellet. The Area in Blue Indicates the Diffusion Zone, and the Region at the Fuel Surface Within the Dashed Red Line Indicates the Radiation Zone

Figure 65: Comparison of Experimental Corrosion Rates to Model Calculations (Stars Connected by the Dashed Line) Using Rates Measured on α-doped UO_2 in Deaerated Solutions Containing Carbonate (Taken from Figure 40)

This model was tested against the corrosion rates compiled in Figure 40 (Liu et al. 2017c). Only rates measured on α-doped UO_2 were used and the model excluded reactions involving ε-particles which are not present in α-doped specimens. Also, in the model the concentrations of radiolytic oxidants (O_2, H_2O_2) and reductants (H_2) were set to zero at the outer boundary of the model to match the experimental conditions allowing the escape of gases from the solutions used. The comparison of model predictions to experimental values demonstrated a good correlation (Figure 65). Also, in agreement with the calculations and conclusions of Nielsen et al. (2008) and Nielsen and Jonsson (2008), this agreement and a series of sensitivity calculations for various model parameters, showed the corrosion rate to be dictated by the α-source strength not controlled by the kinetics of interfacial reactions.

8. CHEMICAL DISSOLUTION UNDER ANOXIC CONDITIONS

As discussed in Section 5.2, when oxidants are scavenged (i.e., E_h decreased) and E_{CORR} is lowered to a value $< (E^e)_{UO2/U4O9}$, the fuel will become immune to corrosion and any further degradation leading to radionuclide release can only proceed by chemical dissolution as U^{IV}. Under these conditions, the UO_2 matrix would be expected to achieve solubility equilibrium and any further dissolution would require disturbance of this equilibrium and a transition to chemically-controlled dissolution. This disturbance could occur by one of two processes; (i) the transport of U^{IV} away from the fuel surface and its adsorption on available surfaces in the vicinity of the fuel (e.g., container corrosion products or on clay in, or surrounding, the container); and (ii) conversion of UO_2 to the more stable U^{IV} phase coffinite ($USiO_4$).

Evidence exists in experiments in Boom clay (clay used in Belgium known to contain reductants which preempt corrosion) that irreversible dissolution can be induced by U^{IV} sorption on the clay. Salah et al. (2006) observed increased U release when clay was present compared to when it was not. Additionally, the dissolution rate of α-doped UO_2 was insensitive to the α-activity level counter to the expectations for corrosion (oxidative dissolution) for α-active materials (Section 5.2 and Figure 40). Sequential extractions of the clay exposed to UO_2 for extensive periods of time showed the vast majority of the released U was associated with the organic fraction of the clay.

Given the unlikelihood that solubility equilibrium can be maintained, a number of studies have been conducted to determine what features would control irreversible chemical dissolution. Popel et al. (2018) investigated the influence of fission fragment damage by bombarding plain UO_2 and samples doped with inactive fission products with $^{129}Xe^{23+}$ ions to a fluence of 4.8 x 10^{15} ions/cm^2. Except for an initial higher release of U from the irradiated specimen, attributed to irradiation induced surficial microstructural changes, measurements of dissolved U and XPS analyses of the surface showed no measurable effect of irradiation. In an earlier study, Popel et al. (2017) claimed the formation of a secondary phase which they attributed to dissolution as U^{IV} from defect sites leading to a redeposition of a less defective, but unidentified U^{IV} phase,

$$(UO_2)_{defective} + 2H_2O \rightarrow U(OH)_4 \rightarrow (UO_2)_{less\ defective} + 2H_2O \tag{50}$$
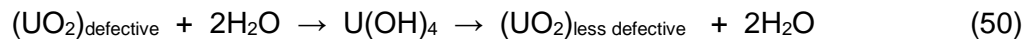
Such a mechanism would be consistent with the earlier results of Ollila et al. (2003) who claimed the solubility equilibrium was dynamic based on isotopic exchange ($^{238}U/^{239}U$) data, and by studies on similar oxides such as CeO_2 and ThO_2 (Corkhill et al. 2016).

That atomic scale changes to the UO_2 surface occurred under anoxic conditions has been shown using STEM (scanning transmission electron microscopy), STEM-EDS (Energy Dispersive Spectroscopy) and STEM-EELS (Electron Energy Loss Spectroscopy) (Popel et al. 2019, 2020). Mapping revealed O incorporation suggesting, in the absence of oxidants, a reaction with H_2O,

$$UO_2 + x(H_2O)_{ads} \rightarrow UO_{2+x} + 2xH_2 \tag{51}$$
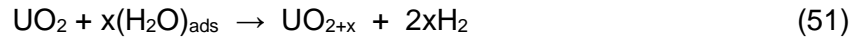
as proposed for PuO_2 (Haschke et al. 2000) in the presence of absorbed H_2O and consistent with the results of Idriss (2010) who claimed UO_2 was oxidized by H_2O vapour. However, this process appears to be limited to O substitution into octahedral interstitial sites leading to a thin surface oxidized layer which subsequently limits dissolution. Such a claim would not be inconsistent with the formation of a thin $U^{IV}_{1-2x}U^{V}_{2x}O_{2+x}$ layer (Section 5.4). In the absence of stronger oxidants than H_2O this layer appears to passivate the surface.

While uraninite (UO_{2+x}) is the primary U^{IV} mineral, it is commonly observed in intimate contact with coffinite ($USiO_4$) in geological locations (Szenknect et al. 2020). As U^{IV} solids, both phases are associated with reducing environments. Thermodynamic calculations show coffinite to be less stable than a crystalline UO_2 and quartz mixture at a low temperature (25 °C) (Szenknect et al. 2016, 2020). However, coffinite has been shown to precipitate in solutions undersaturated with respect to amorphous $UO_2 \cdot 2H_2O$ in silicate solutions with concentrations typical of groundwater (i.e., $[Si]_{tot} \sim 7 \times 10^{-3}$ mol/L (White 1995; Szenknect et al. 2016, 2020). This suggests the possibility that its formation could be observed under DGR conditions which would provide a destabilizing mechanism for UO_2 allowing radionuclide release as its transformation to coffinite progresses.

With this possibility in mind a considerable effort has been expended to determine the viability of such a transformation under DGR conditions (Janecek et al. 1996; Amme et al. 2005; Robit-Pointeau et al. 2006; Duro et al. 2010; Evins and Jensen 2012; Szenknecht et al. 2020). Szenknecht et al. (2020) demonstrated that the transformation did occur on the surface of UO_2 in a solution saturated with respect to amorphous silica (pH = 9) at room temperature under slightly oxidizing conditions. Geochemical calculations using available thermodynamic data showed coffinite could exist with $U^{VI}O_2(OH)_3^-$ as the predominant solution species, suggesting that the production of U^{VI} by self-irradiation or the presence of non-stoichiometry (UO_{2+x}) was an essential feature of the process. Examination of the potential-pH diagram (Figure 66) shows only a narrow range of slightly reducing redox conditions is able to support coffinite formation. While the exact mechanism of this transition remains undefined, it is likely that the more extreme reducing conditions imposed in the presence of H_2 would prevent such a transformation by suppressing E_h below the narrow E_h-pH zone within which it is stable by comparison to UO_2.

A number of measurements of fuel dissolution rates (as opposed to corrosion rates) have been made (Bruno et al. 1991; Grambow and Giffaut 2006; Ollila et al. 2003, Ollila 2008; Poinssot et al. 2005; Saleh et al. 2006) with values ranging from $(6 \pm 2.5) \times 10^{-5}$ mol/m^2·a in dynamic flow through experiments (Bruno et al. 1991) to (4 to 35) x 10^{-8} mol/m^2·a in static experiments (Olilla et al. 2003). Given the range of measurements and analytical techniques employed, the variation in experimental conditions from static to dynamic, the difficulties in measuring the surface area of the fuel specimens used, and the need to exclude air for the duration of the measurements, such a wide range of values is not surprising. Generally, experiments conducted under dynamic conditions yielded higher values than those performed under static

conditions, which would be consistent with the avoidance of solubility equilibrium under dynamic conditions.
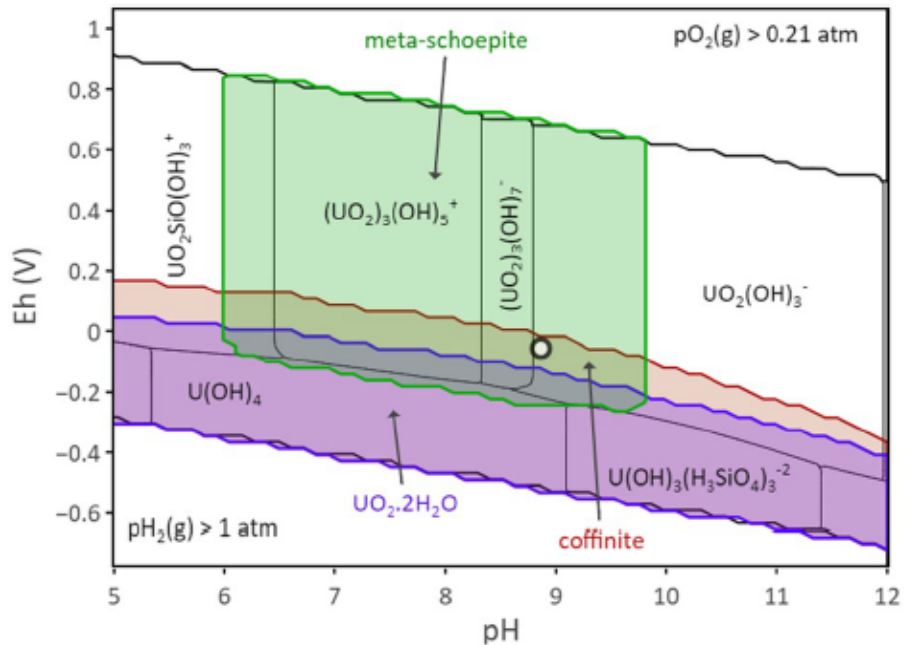
Figure 66: Pourbaix Diagram for U. Predominance Domains of the Major Aqueous Species and Solid Phases Are Shown as a Function of the Reduction Potential (E_h) and pH for $[U]_{total}$ = 5 x 10^{-6} mol/L in Water Containing Silicate Ions with $[Si]_{total}$ = 2 x 10^{-3} mol/L in Equilibrium with the Atmosphere (Szenknect et al. 2020)

9. NATURAL ANALOGUES

Given the time frame for which the containment of spent nuclear fuel is required and the ensuing difficulty in validating claims made based on inevitably short term experiments, natural analogues offer a unique support for the performance assessment of the direct geological disposal of spent nuclear fuel (Lumpkin and Geisler-Wierwille 2012; Bruno and Ewing 2006; Alexander et al. 2015; Cramer 1994; Côme and Chapman 1987: Casas et al. 1992; Bruno et al. 1994). Many potential analogues are ore bodies at relatively shallow depths where high fluxes of groundwater, which are commonly oxidizing, will dominate their corrosion behaviour. This makes the Cigar Lake natural ore deposit in Saskatchewan (Canada) particularly important since it exhibits many features that parallel those incorporated into the design of a Canadian DGR. It is located at a depth (430 m) similar to that of a planned DGR and is surrounded by a clay halo (Figure 67). The key feature of this deposit is its survival (since formation ~ 1.3 Ga ago) in a dominantly U^{IV} state as uraninite (UO_{2+x}), a close analog for nuclear fuel. The absence of any surface indication of its presence indicates that the combination of natural barriers has been effective in isolating the ore from the surface environment.

Given these features a substantial amount of research has been conducted to determine the key geological and chemical features of this deposit (Cramer and Smellie 1994; Cramer and

Karlsson 1996) with the accumulation of evidence supporting the maintenance of reducing conditions:

- The groundwaters sampled in the ore were found to be reducing (E_h = -242 mV) and near neutral pH.

- XPS analyses showed the extent of oxidation to be low with the U^{VI}/U^{IV} ratio being generally < 0.5 and most commonly in the range 0.16 to 0.29 (Sunder et al. 1987,1991b (When these analyses were performed, spectral resolution was not sufficiently accurate to separate U^V and U^{VI})). XRD analyses confirmed the presence of an oxidized phase, most likely α-U_3O_7, consistent with the maintenance of the cubic fluorite lattice emblematic of the UO_2 structure.

- The average U concentrations in groundwater collected from the ore body ranged from 3.27 x 10^{-8} to 1.07 x 10^{-7} mol/L suggesting equilibration with a partially oxidized uraninite (UO_{2+x}) (Bruno and Casas 1994), consistent with the XPS/XRD analyses and mineralogical characterizations.

- The measured [H_2] in the ore body was 8.25 x 10^{-4} mol/L, i.e., at levels shown to effectively suppress fuel corrosion under laboratory conditions (Section 6).
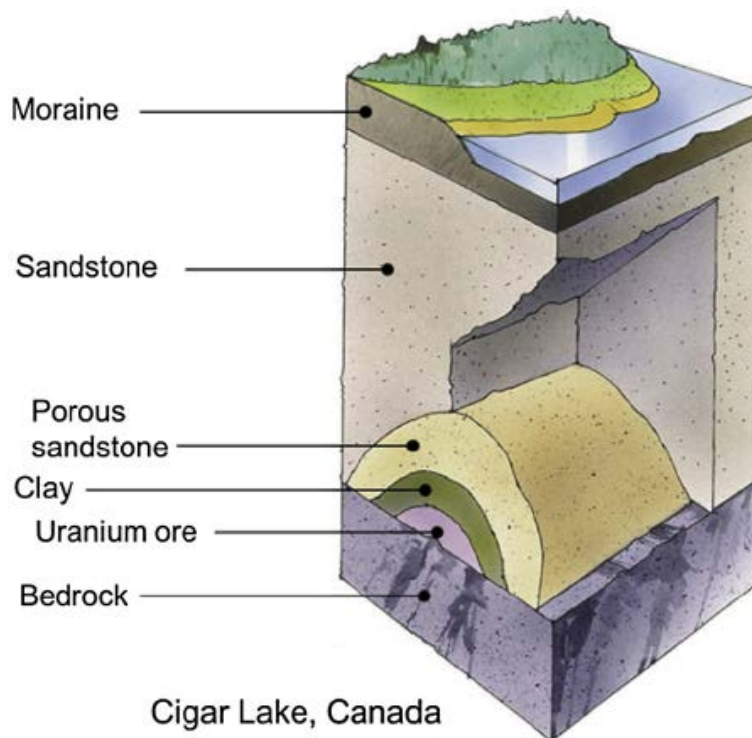
Figure 67: A Schematic Representation of the Main Geological Units at the Cigar Lake Uraninite Ore Deposit (Bruno and Spahiu 2014)

Radiolysis models (Jansson 1996; Jinsong and Neretnieks 1996) indicated that α-radiolysis was the only meaningful source of oxidants (and H_2) within the ore body. Calculating the extent of radiolytic oxidant production was complicated by the grain structure of the deposit which made it difficult to determine the proportion of α-radiation which escaped the solid to radiolytically decompose H_2O. Despite this limitation, calculations (Jinsong and Neretnieks 1996) yielded oxidant production rates approximately two orders of magnitude greater than could be accounted for presuming the oxidants were only consumed by SH^- (present as pyrite (FeS_2)), oxidation to SO_4^{2-} or the oxidation of Fe^{II} to Fe^{III} (as hematite (α-Fe_2O_3) (Cramer and Smellie 1994; Smellie and Karlsson 1996). Based on the accumulated evidence from the studies described in Section 6, Bruno and Spahiu (2014) made a convincing argument that the majority of radiolytic oxidants produced within the deposit were scavenged by radiolytic H_2 via the radical-UO_{2+x} catalyzed mechanism described in Section 6. This provides a supporting observation for the claims (based on laboratory studies) that radiolytic H_2 will suppress spent fuel corrosion in a DGR.

10. SUMMARY AND CONCLUSIONS

The basic properties of unirradiated and in-reactor irradiated UO_2 fuel have been reviewed. The radionuclides formed in-reactor are divided into two categories: (i) the instant release inventory/fraction (IRF) which is assumed to be released immediately on contact of the fuel with groundwater; and (ii) the matrix inventory which will be released at a rate controlled by the corrosion/dissolution of the spent fuel matrix. For CANDU fuels, which have low burnup, the IRF is small, typically several % or less. Even for current higher burn-up LWR fuels, the majority of the radionuclides are in the matrix inventory.

In an intact container with a dry interior, the fuel will retain the radionuclides. If the container fails, groundwater can enter. While groundwater entering the failed waste container will be anoxic, H_2O radiolysis will provide oxidants capable of driving fuel corrosion and radionuclide release. Assuming a reasonable container containment period prior to groundwater ingress, α-radiolysis will be the dominant source of oxidants, of which H_2O_2 will be the most important. The fuel corrosion/radionuclide release rate will be controlled by the redox conditions established at the fuel surface. Since two oxidation fronts exist within a failed container, radiolytic oxidants produced at the fuel surface can be scavenged by Fe^{2+} and H_2 produced by corrosion of the steel containment vessel.

A wide range of specimens have been used to investigate the fuel corrosion processes including natural UO_2 in both pellet and powder form, SIMFUELs to replicate chemical changes due to in-reactor irradiation, α-doped UO_2 to simulate fuels of different ages (after discharge from reactor), and spent nuclear fuel.

Corrosion of UO_2 proceeds via the formation of a thin layer of $U^{IV}_{1-2x}U^{V}_{2x}O_{2+x}$ which subsequently oxidizes to form U^{VI} which either dissolves as $U^{VI}O_2^{2+}$ or accumulates on the fuel surface as either schoepite ($UO_3 \cdot yH_2O$) or studtite ($UO_4 \cdot 4H_2O$). Under strongly oxidizing conditions (i.e., irradiated aerated conditions), more complex deposits incorporating groundwater anions and cations can form, but this would not be expected for the anoxic conditions and α-radiation fields anticipated in a Canadian DGR.

Of the chemical species expected in groundwaters, only HCO_3^-, Ca^{2+}, and SiO_4^{4-} will have significant effects on fuel corrosion, HCO_3^- by complexing UO_2^{2+} and accelerating dissolution, Ca^{2+} and SiO_4^{4-} by stabilizing U^{VI} phases and suppressing dissolution. In the case of HCO_3^- and Ca^{2+}, complex surface interactions involving H_2O_2 could occur but are unlikely to be significant at the H_2O_2 concentrations anticipated under repository disposal conditions.

In-reactor RE^{III} (Rare Earth) doping of the UO_2 matrix and the formation of noble metal (ε) particles are the two features, along with α-radiation fields, which exert the biggest influence on the fuel corrosion behaviour. RE^{III} doping stabilizes the UO_2 matrix leading to > 95% of radiolytic H_2O_2 undergoing decomposition to H_2O and the much less reactive O_2 rather than causing corrosion. The influence of ε-particles is more ambiguous since, when galvanically coupled to the UO_2 matrix, they can both support and suppress corrosion by catalyzing the reduction of H_2O_2 or the oxidation of H_2 as well as catalyzing H_2O_2 decomposition and its scavenging by H_2.

Reactions involving H_2O_2 are complicated since it can participate in the corrosion process not only as an oxidant but also as a complexant involved in the fuel dissolution step. Most of the studies demonstrating this last feature were conducted at $[H_2O_2]$ well above those sustainable

by α-radiolysis making it very unlikely such reactions will exert any significant influence on the overall fuel corrosion process.

Both Fe^{2+} and H_2, produced by corrosion of the steel vessel can scavenge radiolytically-produced H_2O_2 and suppress the fuel corrosion rate with the influence of H_2 being particularly effective. A wide range of studies show that the corrosion rate is proportional to the α-radiation dose rate and that it can be suppressed by small $[H_2]$ well within the range achievable inside a failed container.

Extensive studies and model calculations have demonstrated this influence of H_2 can be attributed to its ability to use both the UO_2 surface and ε-particles to catalyze its reaction with H_2O_2 leading to recombination to produce H_2O rather than matrix corrosion. Both experimental measurements and model calculations demonstrate that complete suppression of corrosion/radionuclide release can be achieved with micromolar concentrations of H_2, and that radiolytically-produced H_2 also plays a significant role in this process. Since container failure should not occur until only α-radiation is important and significant groundwater $[H_2]$ have already developed due to steel corrosion, minimal to insignificant amounts of corrosion would be expected.

Under these reducing conditions in the container, only chemical dissolution, not electrochemical corrosion, would lead to destruction of the fuel matrix. Since the solubility of UO_2 is extremely low under reducing conditions, its dissolution will be slow as demonstrated in measurements conducted under controlled anoxic conditions. The influence of radiation-induced defects on dissolution have been shown to be negligible.

The conversion of UO_2 to coffinite ($USiO_4 \cdot nH_2O$: a known U^{IV} mineral sometimes observed associated with geologic uraninite ($UO_{2+}x$) deposits) appears to be the only process able to destabilize the fuel matrix, thereby accelerating its chemical dissolution and enhancing radionuclide release. Since the UO_2 to coffinite conversion involves an intermediate U^{VI} state, it is very unlikely to occur in the presence of H_2 when all potential oxidants have been scavenged.

Evidence from the Cigar Lake natural analogue provides a solid base of supporting evidence that corrosion will be minimal. It also yields solid support that H_2, in the geological case produced only radiolytically, will be the major factor in stabilizing U^{IV} and maintaining the very long-term stability of the UO_2 fuel matrix.

REFERENCES

Abrafah, J., S. Marschmann and E. Jensen. 1998. Examination of the surface coatings removed from K-East Basin fuel elements. Pacific Northwest Nuclear Laboratory Report, PNNL-11806. Richland, WA, USA.

Alexander, W.R., H.N. Reijonen and I.G. McKinley. 2015. Natural analogues: Studies of geological processes relevant to radioactive waste disposal in deep geological repositories. *Swiss J Geosci* 108: 75-100.

Albinsson, Y.A., A. Odegaard-Jensen, V.M. Oversby and L.O. Werme. 2003. Leaching of spent fuel under anaerobic and reducing conditions. *Mater Res Soc Symp P* 757: 407-413.

Amme, M. 2002. Contrary effects of the water radiolysis product H_2O_2 upon the dissolution of nuclear fuel in natural ground water and deionized water. *Radiochim Acta* 90: 399-406.

Amme, M., B. Renker, B. Schmid, H. Feth, H. Bertagnoli and W. Dobelin. 2002. Raman microspectrometric identification of corrosion products formed on UO_2 nuclear fuel during leaching experiments. *J Nucl Mater* 306: 202-212.

Amme, M., T.Wiss, H.Thiel, P. Boulet and H. Lang. 2005a. Uranium secondary phase formation during anoxic hydrothermal leaching processes of UO_2 nuclear fuel. *J Nucl Mater* 341: 209-223.

Amme, M., W. Bors, C. Michel, K. Stettmaier, G. Rasmussen and M. Betti. 2005b. Effects of Fe(II) and hydrogen peroxide interaction upon dissolving UO_2 under geologic repository conditions, *Environ Sci Technol* 39: 221-229.

Anastasijevic, N.A., Z.M. Cimitrijevu and R.R. Adzic. 1986. Oxygen reduction on a ruthenium electrode in alkaline electrolytes. *J Electroanal Chem* 199: 351-364.

Andersen, E.B., B.E. Burakov and E.M. Pazukhin. 1993. Secondary changes in fuel-containing masses from the fourth block of the Chernobyl NDP. *Sov Radiochem+* 345: 625 -630.

Ariani, I., Dose Rate Analysis to Support Radiolysis Assessment of Used CANDU Fuel, Nuclear Waste Management Organization Technical Report, NWMO-TR-2022-02. Toronto, Canada.

Armstrong, C.R., M. Nyman, T. Shvareva, G.E. Sigmon, P.C. Burns and A. Navrotsky. 2012. Uranyl peroxide enhanced nuclear fuel corrosion in seawater. *P Natl Acad Sci USA* 109: 1874-1877.

Baker, R.J. 2014. Uranium minerals and their relevance to long term storage of nuclear fuels. *Coordin Chem Rev* 266-267: 123-136.

Barb, W.G., J.H. Baxendale, P. George and K.R. Hargrave. 1951. Reactions of ferrous and ferric ions with H_2O_2. II The ferric reaction. *T Faraday Soc* 47: 591-616.

Barreiro-Fidalgo, A. and M.Jonsson. 2019. Radiation induced dissolution of (U,Gd)O_2 pellets in aqueous solution – a comparison to standard UO_2 pellets. *J Nucl Mater* 514: 216-223.

Barreiro-Fidalgo, A., B. Dahlgren, T. Brinck and M. Jonsson. 2016. Surface reactions of H_2O_2, H_2 and O_2 in aqueous systems containing ZrO_2. *J Phys Chem C* 120: 1609-1614.

Barreiro-Fidalgo, A., S. Sundin and M. Jonsson. 2014. Effect of bentonite on radiation induced dissolution of UO2 in an aqueous system. *J Nucl Mater* 447: 73-76.

Barriero-Fidalgo, A., Y. Kumagai and M. Jonsson. 2018. The role of surface-bound hydroxyl radicals in the reaction between H_2O_2 and UO_2. *J Coord Chem* 71: 1799-1807.

Bauhn, L., N. Hansson, C. Ekberg, P. Fors and K. Spahiu. 2018. The fate of hydroxyl radicals produced during H_2O_2 decomposition on a SIMFUEL surface in the presence of dissolved hydrogen. *J Nucl Mater* 507: 38-43.

Betteridge, J.S., N.A.M. Scott, D.W. Shoesmith, L.E. Bahen, W.H. Hocking and P.G. Lucuta. 1997. Effects of hyperstoichiometry and fission products on the electrochemical reactivity of UO_2 nuclear fuel. Atomic Energy of Canada Ltd. Report, AECL-11647, COG-96-331-1. Chalk River, Canada.

Bevan, D.J.M., I.E. Grey and B.T.M. Willis. 1986. The crystal structure of β-U_4O_{9-y}. *J Solid State Chem* 61: 1-7.

Beyenal, H., R.K. Sani, B.M. Peyton, A.C. Dohnalkova, J.E. Amonette and Z. Lewandowski. 2004. Uranium immobilization by sulfate-reducing biofilms. *Environ Sci Technol* 38: 2067-2074.

Brincat, N.A., M. Molinari, G.C. Allen, M.T. Storr and S.C. Parker. 2015. Density functional theory calculations of defective UO_2 at U_3O_7 stoichiometry. *J Nucl Mater* 467: 724-729.

Broczkowski, M.E. 2008. The effects of hydrogen and temperature on the electrochemistry and corrosion of uranium dioxide. Ph.D. Thesis, The University of Western Ontario, London, ON, Canada.

Broczkowski, M.E., J.J. Noël and D.W. Shoesmith. 2007. The influence of dissolved hydrogen on the surface composition of doped uranium dioxide under aqueous corrosion conditions. *J Electroanal Chem* 602: 8-16.

Broczkowski, M.E., J.J. Noël and D.W.Shoesmith. 2005. The inhibiting effects of hydrogen on the corrosion of uranium dioxide under nuclear waste disposal conditions. *J Nucl Mater* 346: 16-23.

Broczkowski, M.E., P.G. Keech, J.J. Noël and D.W. Shoesmith. 2010. Corrosion of uranium dioxide containing simulated fission products in dilute hydrogen peroxide and dissolved hydrogen. *J Electrochem Soc* 157: C275-C281.

Broczkowski, M.E., P.G. Keech. J.J. Noël and D.W. Shoesmith. 2011. The role of dissolved hydrogen on rare earth doped uranium dioxide corrosion in the presence of hydrogen peroxide. *J Electrochem Soc* 158: C439-C444.

Broczkowski, M.E., R. Zhu, Z. Ding, J.J. Noël and D.W. Shoesmith. 2006. Electrochemical, SECM and XPS studies of the influence of H_2 on UO_2 nuclear fuel corrosion. *Mater Res Soc Symp P* 932: 449-456.

Brown, R.A. 1980. Uranium precipitation with hydrogen peroxide. *Soc Min Eng AIME* 270: 1836-1840.

Bruno, J. and I. Casas. 1994. Spent fuel dissolution modelling. In: Final Report of the AECL/SKB Cigar Lake analog study (Editors Cramer, J.J. and J.A.T. Smellie). Atomic Energy of Canada Limited Report, AECL-10851. Chalk River, Canada.

Bruno, J., I. Casas, E. Cera, R.C. Ewing, R.J. Finch and L.O. Werme. 1994. The assessment of the long-term evolution of the spent nuclear fuel matrix by kinetic, thermodynamic and spectroscopic studies of uranium minerals. *Mater Res Soc Symp P* 353: 633-639.

Bruno, J., I. Casas and I. Puigdomenech. 1991. The kinetics of dissolution of UO_2 under reducing conditions and the influence of an oxidized surface layer (UO_{2+x}): Application of a continuous flow-through reactor. *Geochim Cosmochim Ac* 55: 647-658.

Bruno, J. and K. Spahiu. 2014. The long-term effect of hydrogen on the UO_2 fuel stability under anoxic conditions: Findings from the Cigar Lake natural analogue study. *Appl Geochem* 49: 178-183.

Bruno, J. and R.C. Ewing. 2006. Spent nuclear fuel. *Elements* 2: 343-349.

Buck, E.C., D.J. Wronkiewicz, P.A. Finn and J.K. Bates. 1997. A new uranyl oxide hydrate phase derived from spent fuel alteration. *J Nucl Mater* 249: 70-76.

Buck, E.C., R.J. Finch, P.A.Finn and J.K. Bates. 1998. Retention of neptunium in uranyl alteration phases formed during spent fuel corrosion. *Mater Res Soc Symp P* 506: 87-94.

Burns, P.C. and K.-A. Hughes. 2003. Studtite, $[(UO_2)(O_2)(H_2O)_2](H_2O)_2$: the first structure of a peroxide mineral. *Am Mineral* 88: 1165-1168.

Burns, P.C., R.C. Ewing and M.L. Miller. 1997a. Incorporation mechanisms of actinide elements into the structures of U^{6+} phases formed during the oxidation of spent nuclear fuel. *J Nucl Mater* 245: 1-9.

Burns, P.C., R.J. Finch, F.C. Hawthorne, M.L. Miller and R.C. Ewing. 1997b. The crystal structure of ianthinite $[UO_2^{4+}(UO_2)_4O_6(OH)_4(H_2O)_4](H_2O)_5$: a possible phase for Pu^{4+} incorporation during the oxidation of spent nuclear fuel. *J Nucl Mater* 249: 199-206.

Campbell, T.K., E.R. Gilbert, G.D. White, G.F. Piepel and B. Wrona 1989. Oxidation behaviour of nonirradiated UO_2. *Nucl Technol* 85: 160-171.

Carbol, P., J. Cobos-Sabate, J.-P. Glatz, C. Ronchi, V. Rondinella, D. H. Wegen, T. Wiss, A. Loida, V. Metz, B. Kienzler, K. Spahiu, B. Grambow, J. Quinones and A. Martinez Esparza Valiente. 2005. The effect of dissolved hydrogen on the dissolution of ^{233}U-doped $UO_2(s)$, high burn-up spent fuel and MOX fuel. Swedish Nuclear Fuel and Waste Management Company Report, TR-05-09. Stockholm, Sweden.

Carbol, P., P. Fors, S. Van Winckel and K. Spahiu. 2009a. Corrosion of irradiated MOX fuel in the presence of dissolved H_2. *J Nucl Mater* 392: 45-54.

Carbol, P., P. Fors, T. Gouder and K. Spahiu. 2009b. Hydrogen suppresses UO_2 corrosion. *Geochim Cosmochim Ac* 73: 4366-4375.

Casas, I., E. Cera and J. Bruno. 1992. Kinetic studies of natural minerals for the long-term evolution of spent nuclear under oxidizing conditions. *Mater Res Soc Symp P* 294: 521-528.

Casas, I., J. de Pablo, J. Gimenez, M.E. Torrero, J. Bruno, E. Cera, R.J. Finch and R.C. Ewing. 1998. The role of pe, pH and carbonate on the solubility of UO_2 and uraninite under nominally reducing conditions. *Geochim Cosmochim Ac* 62: 2223-2231.

Casella, A., B. Hanson and W. Miller. 2016. The effect of chemistry on UO_2 dissolution. *J Nucl Mater* 476: 45-55.

Cejka, J., J. Sejkora and M. Deliens. 1996. New data on studtite, $UO_4.4H_2O$ from Shinkolobwe, Shaba, Zaire. *Neues Jb Miner Monat* 3: 125-134.

Cerrato, J.M., C.J. Barrows, L.Y. Blue, J.E. Lezama-Pacheco, J.R. Barger and D.E. Giammar. 2012. Effect of Ca^{2+} and Zn^{2+} on UO_2 dissolution rates. *Environ Sci Technol* 46: 2731-2737.

Chadwick, M.B, M. Herman, P. Oblozinsky, M.E. Dunn, Y. Danon, A.C. Kahler, D.L. Smith, B. Pritychenko, G. Arbanas, R. Arcilla, R. Brewer, D.A. Brown, R. Capote, A.D. Carlson, Y.S. Cho, H. Derrien, K. Guber, G.M. Hale, S. Hoblit, S. Holloway, T.D. Johnson, T. Kawano, B.C. Kiedrowski, H. Kim, S. Kunieda, N.M. Larson, L. Leal, J.P. Lestone, R.C. Little, E.A. McCutchen, R.E. MacFarlane, C.M. McInnes, G.M. Mattoon, R.D. McKnight, S.F. Mughabghab, G.P.A. Nobre, G. Palmiotti, A. Palumbo, M.T. Pigni, V.G. Pronyaev, R.O. Sayer, A.A. Sonzogni, N.C. Summer, P. Talou, I.J. Thompson, A. Trkov, R.L. Vogt, S.C. van der Marck, A. Wallner, M.C. White, D. Wiarda and P.G. Young. 2011. ENDF/B-VII.1 nuclear data for science and technology: cross sections, covariances, fission product yields and decay data. *Nucl Data Sheets* 112: 2887-2996.

Cheong, W-J., P.G. Keech, J.C. Wren, Z. Qin and D.W. Shoesmith. 2007. Modelling the distribution of acidity within nuclear fuel (UO_2) corrosion product deposits and porous sites. *Mater Res Soc Symp P* 985.

Choi, J.W., R.J. McEachern, P.Taylor and D.D. Wood. 1996. The effect of fission products on the rate of U_3O_8 formation in SIMFUEL oxidized in air at 250ºC. *J Nucl Mater* 230: 250-258.

Christensen, H. and E. Bjergbakke. 1982. Radiolysis of groundwater from spent fuel. Swedish Nuclear Fuel and Waste Management Company Report, TR-82-18. Solna, Sweden.

Christensen, H., R. Forsyth, L. Lundquist and L.O. Werme. 1990. Radiation induced dissolution of UO_2. Studsvik Energiteknik AB Report, NS-90185. Nykoping, Sweden.

Christensen, H., S. Sunder and D.W. Shoesmith. 1994. Oxidation of nuclear fuel (UO_2) by the products of water radiolysis: development of a kinetic model. *J Alloy Compd* 213/214: 93-99.

Clarens, F., J. de Pablo, I. Diaz-Perez, I. Casas, J. Gimenez and M. Rovira. 2004. Formation of studtite during the oxidative dissolution of UO_2 by hydrogen peroxide. A SFM study. *Environ Sci Technol* 38: 6656-6661.

Clarens, F., J.Gimenez, J. de Pablo, I. Casas, M.Rovira, J. Dies, J. Quinones and A. Martinez-Esparza. 2005. Influence of β-radiation on UO_2 dissolution at different pH values. *Radiochim Acta* 93: 533-538.

Cobos, J., D. Papaioannou, J. Spino and M. Coquerelle. 1998. Phase characterization of simulated high burn-up UO_2 fuel. *J Alloy Compd* 271-273: 610-615.

Cobos, J., T. Wiss, T. Goudes and V.V. Rondinella. 2003. XPS and SEM studies on the corrosion of UO_2 containing plutonium in de-mineralized and carbonated water. *Mater Res Soc Symp P* 757: 365-375.

Cobos, J., V.V.R. Havela, J. de Pablo, T. Couder, J.-P. Glatz, P. Carbol and Hj. Matzke. 2002. Corrosion and dissolution studies of UO_2 containing α-emitters. *Radiochim Acta* 90: 597-602.

Colàs, E., A. Valls, D. García, L. Duro. 2021. Radionuclide Solubility Calculation (Phase 1). Nuclear Waste Management Organization Technical Report, NWMO-TR-2021-02. Toronto, Canada.

Colàs, E., A. Valls, D. García, L. Duro. 2022. Radionuclide Solubility Calculation (Phase 2). Nuclear Waste Management Organization Technical Report, NWMO-TR-2022-11. Toronto, Canada.

Côme, B and N.A. Chapman (editors). 1987. Natural analogues in radioactive waste disposal. Commission of European Communities Report, EUR 11037 EN.

Conradson, S.D., D. Manara, F. Wastin, D.L. Clark, G.H. Lander, L.A. Morales, J. Rebizant and V.V. Rondinella. 2004. Local structure and charge distribution in the UO_2-U_4O_9 system. *Inorg Chem* 43: 6922-6935.

Corbel, C., G. Sattonay, S. Guilbert, F. Garrido, M.-F. Barthe and C. Jegou. 2006. Addition versus radiolytic production effects of hydrogen peroxide on aqueous corrosion of UO_2. *J Nucl Mater* 348: 1-17.

Corcoran, E.C., M.H. Kaye, F. Akbari, J.D. Higgs, B.J. Lewis and W.T. Thompson. 2007. First principles CANDU fuel model and validation experimentation. International LWR fuel performance meeting, Paper 107: 99-106. San Francisco, CA, USA.

Cordfunke, E.H.P. and R.J.M. Konings. 1988. Chemical interactions in water-cooled nuclear fuel. A thermodynamic approach. *J Nucl Mater* 152: 301-309.

Corkhill, C.L., D.J. Bailey, F.Y. Tocino, M.C. Stennet, J.A. Miller, J.L. Provis, K.P. Travis and N.C. Hyatt. 2016. Role of microstructure and surface defects on the dissolution kinetics of CeO_2, a UO_2 fuel analogue. *ACS Appl Mater Inter* 8: 10562-10571.

Cramer, J. 1994. Natural analogs in support of the Canadian concept for nuclear fuel waste disposal. Atomic Energy of Canada Limited Report, AECL-10291, COG-92-258. Chalk River, Canada.

Cramer, J.J. and J.A.T. Smellie. 1994. Final report of the AECL/SKB Cigar Lake analog study. Atomic Energy of Canada Limited Report, AECL-10851. Chalk River, Canada.

Crocombette, J.-P., F. Jollet, L.T. Nga and J. Petit. 2001. Plane-wave pseudopotential study of point defects in uranium dioxide. *Phys Rev B* 64: 104107-104112.

Cui, D. and K. Spahiu. 2002. The reduction of U(VI) on corroded iron under anoxic conditions. *Radiochim Acta* 90: 623-628.

Cui, D., J. Low and K. Spahiu. 2011. Environmental behaviour of spent nuclear fuel and canister materials. *Energ Environ Sci* 4: 2537-2545.

Cui, D., K. Spahiu and P. Wersin. 2003. Redox reactions of iron and uranium dioxide in simulated cement pore water under anoxic conditions. *Mater Res Soc Symp P* 757: 427-432.

Cui, D., L. Low, V.V. Rondinella and K. Spahiu. 2010. Hydrogen catalytic effects of nanostructural alloy particles in spent fuel on radionuclide immobilization. *Appl Catal B-Environ* 94: 173-178.

De Pablo, J., I. Casas, F. Clarens, F. El Aamrani and M. Rovira. 2001. The effect of hydrogen peroxide concentration on the oxidative dissolution of unirradiated uranium dioxide. *Mater Res Soc Symp P* 663: 409-426.

De Pablo, J., I. Casas, J. Gimenez, V. Marti and M.E. Torrero. 1996. Solid surface evolution model to predict uranium release from inirradiated UO_2 and nuclear spent fuel dissolution under oxidizing conditions. *J Nucl Mater* 232: 138-145.

De Pablo, J., I. Casas, M. Jimenez, M. Molera, L. Rovira, L. Duro and J. Bruno. 1999. The oxidative dissolution mechanism of uranium dioxide. The effect of temperature in hydrogen carbonate medium. *Geochim Cosmochim Ac* 63: 3097-3103.

De Pablo, J., I. Casas, J. Gin, F. Clarens, L. Duro and J. Bruno. 2004. The oxidative dissolution mechanism of uranium dioxide. The effect of pH and oxygen. *Mater Res Soc Symp P* 807: 83-88.

Deliens, M and M.Piret. 1983. Metastudtite, $UO_4.2H_2O$, a new mineral from Shinkolobwe, Shaba, Zaire. *Am Mineral* 68: 456-458.

Desgranges, L., M. Ripert, J. Piron, H. Kodja and J. Gallier. 2003. Behaviour of fission gases in an irradiated nuclear fuel under alpha external irradiation. *J Nucl Mater* 321: 324-330.

Desgranges, L., G. Baldinozzi, D. Simeone, H.E. Fischer. 2016. Structural changes in the local environment of uranium atoms in the three phases of U_4O_9. *Inorg Chem* 55: 7485-7491.

Desgranges, L., G. Baldinozzi, P. Simon, G. Guimbretiere and A. Canizarro. 2012a. Raman spectrum of U_4O_9: a new interpretation of damage lines in UO_2. *J Raman Spectrosc* 43: 455-458.

Diaz-Arocas, P., J. Quinones, C. Maffiotte, J. Serrano, J. Garcia, J.R. Almazan and J. Esteban. 1995. Effect of secondary phase formation in the leaching of UO_2 under simulated radiolytic conditions. *Mater Res Soc Symp P* 353: 641-646.

Dong, W. and S.C. Brooks. 2006. Determination of the formation constants of ternary complexes of uranyl and carbonate with alkaline earth metals (Mg^{2+}, Ca^{2+}, Sr^{2+}, Ba^{2+}) using an anion exchange method. *Environ Sci Technol* 40: 4689-4695.

Duro, L., M. Grive, J. Bruno and R. Pehrman. 2010. Information on potential long-term conversion mechanisms of ceramic spent fuel in the late post-closure phase. Amphos[21] Consulting Report, R-2225.2. Barcelona, Spain.

Eary, L.E. and L.M. Cathles. 1983. A kinetic model of UO_2 dissolution in acidic H_2O_2 solutions that includes uranium peroxide hydrate precipitation. *Metall Trans B* 14B: 325-334.

Einziger, R.E., L.E. Thomas, H.C. Buchanan and R.B. Stout. 1992. Oxidation of spent fuel in air at 175 to 195°C. *J Nucl Mater* 190: 53-60.

Ekeroth, E. and M. Jonsson. 2003. Oxidation of UO_2 by radical oxidants. *J Nucl Mater* 322: 242-248.

Ekeroth, E., M. Granfors, D. Schild and K. Spahiu. 2020. The effect of temperature and fuel surface area on spent fuel dissolution kinetics under H_2 pressure. *J Nucl Mater* 531: 151981.

Ekeroth, E., O. Roth and M. Jonsson. 2006. The relative impact of radiolysis products in radiation induced oxidative dissolution of UO_2. *J Nucl Mater* 355: 38-46.

El Aamrani, F., I. Casas, C. Martin, M. Rovira and J. de Pablo. 1998. Effect of iron and canister corrosion products on the dissolution of UO_2. Spent Fuel Workshop, Las Vegas, NV, USA.

Elorrieta, J.M., L.J. Bonales, N.Rodriguez-Villagra, V.G. Baonza and G.Cobos. 2016. A detailed Raman and X-ray study of UO_{2+x} oxides and related structural transitions. *Phys Chem Chem Phys* 18: 28209-28216.

Eriksen, T.V., D.W. Shoesmith and M. Jonsson. 2012. Radiation induced dissolution of UO_2 based nuclear fuel – A critical review of predictive modelling approaches, *J Nucl Mater* 420: 409-423.

Evins, L.Z. and K.A. Jensen. 2012. Review of spatial relationships between uraninite and coffinite – Implications for alteration mechanisms. *Mater Res Soc Symp P* 1475: 89-96.

Fanhagel, Th. and V. Neck. 2002. Aquatic chemistry and solubility phenomena of actinide oxides/hydroxides. *Pure Appl Chem* 74: 1895-1907.

Ferry, C., C.Poinssot, C.Cappelaere, L.Desgranges, C.Jegou, F.Miserque, J.P. Piron, D. Roudil and J.M. Gras. 2006. Specific outcomes of the research on the spent fuel long-term evolution in interim dry storage and deep geological disposal. *J Nucl Mater* 352: 246-253.

Ferry, C., J.-P. Peron, A. Poulesquen and C. Poinssot. 2008. Radionuclide release from spent fuel under disposal conditions. Re-evaluation of the instant release fraction. *Mater Res Soc Symp P* 1107: 447-454.

Ferry, C., J-P. Piron and A. Ambard. 2010. Effect of helium on the microstructure of spent fuel in a repository: An operational approach. *J Nucl Mater* 407: 100-109.

Finch, R.J. and R.C. Ewing. 1991. Alteration of natural uraninite under oxidizing conditions from Shinkolobwe, Katanga, Zaire: a natural analog for the corrosion of spent fuel. *Radiochim Acta* 52/53: 395-401.

Finch, R.J. and R.C.Ewing.1992. The corrosion of uraninite under oxidizing conditions. *J Nucl Mater* 190: 133-156.

Finch, R.J., E.C. Buck, P.A. Finn and J.K. Bates. 1999. Oxidative corrosion of spent UO_2 fuel in vapour and dripping groundwater at $90^{\circ}C$. *Mater Res Soc Symp P* 556: 431-438.

Finn, P., J.K. Bates, J. Hoh, J. Emery, L.D. Hafenrichter, E.C. Buck, M. Gong. 1994a. Elements present in leach solutions from unsaturated spent fuel tests. *Mater Res Soc Symp P* 333: 399-404.

Finn, P.A., E.C. Buck, M. Gong, J.C. Hoh, J.W. Emery, L.D. Hafenrichter and J.K. Bates. 1994b. Colloidal products and actinide species in leachate from spent nuclear fuel. *Radiochim Acta* 66/67: 189-195.

Floyd, M., J. Novak and P.T. Truant. 1992. Fission gas release in fuel performing to extended burn-ups in Ontario Hydro nuclear generating stations. Atomic Energy of Canada Limited Report, AECL-10636. Chalk River, Canada.

Forbes, T.Z., P. Horan, T. Devine, D. McInnes and P.C. Burns. 2011. Alteration of dehydrated schoepite and soddyite to studtite $[(UO_2)(O_2)(H_2O)_2](H_2O)_2$. *Am Mineral* 96: 202-206.

Fors, P., P. Carbol, S. Van Winckel and K. Spahiu. 2009. Corrosion of high burn-up structured UO_2 fuel in the presence of dissolved H_2. *J Nucl Mater* 394: 1-8.

Freyss, M. T. Petit and J.-P. Crocombette. 2005. Point defects in uranium dioxide: Ab initio pseudopotential approach in the generalized gradient approximation. *J Nucl Mater* 347: 44-51.

Fu, D., X. Zhang, P.G. Keech, D.W. Shoesmith and J.C. Wren. 2010. An electrochemical study of H_2O_2 decomposition on single-phase γ-FeOOH films. *Electrochim Acta* 55: 3787-3796.

Fuger, J. 1997. Problems in the thermodynamics of the actinides in relation with the back-end of the nuclear cycle. *J Nucl Mater* 201: 3-14.

Garcia, M.F., A.M. Arias, J.C. Hanson and J.A. Rodriguez. 2004. Nanostructured oxides in chemistry: characterization and properties. *Chem Rev* 104: 4063-4104.

Garisto, F. 2017. Sixth Case Study: Features, Events and Processes. Nuclear Waste Management Organization Technical Report, NWMO-TR-2017-08. Toronto, Canada.

Garisto, F., D.H. Barber, E. Chen, A. Inglot and C.A. Morrison. 2009. Alpha, beta and gamma dose rates in water in contact with used CANDU fuel. Nuclear Waste Management Organization Technical Report, NWMO-TR-2009-27. Toronto, Canada.

Garisto, F., N. Avis, A. Calder, A. D'Andrea, P. Gierszewski, C. Kitson, T. Melnyk, K. Wei and L. Wojciechowski. 2004. Third Case Study – Defective container scenario. Ontario Power Generation Report, 06219-REP-01200-10126-R00. Toronto, Canada.

Garrido, F., R.M. Ibberson, L. Nowicki and B.T.M. Willis. 2003. Cuboctahedral clusters in U_3O_7. *J Nucl Mater* 322: 87-89.

Geng, H.Y., Y. Chen, Y. Kaneta, M. Iwasami, T. Ohnuma and M. Kinoshita. 2008. Point defects and clustering in uranium dioxide by LSDA + U calculations. *Phys Rev B* 77: 104120.1-104120.16.

Gimenez, J. ,E. Baraj, M.E. Torrero, I. Casas and J. de Pablo. 1996. Effect of H_2O_2, NaClO and Fe on the dissolution of unirradiated UO_2 in 5 mol/kg NaCl: Comparison with spent fuel dissolution experiments. *J Nucl Mater* 238: 64-69.

Gobien, M., F.Garisto, E. Kremer and C.D. Medri. 2018. Seventh case study: reference data and codes. Nuclear Waste Management Organization Technical Report, NWMO-TR-2018-10. Toronto, Canada.

Gobien, M., K. Liberda and C. Medri. 2021. Fuel radiotoxicity and screening analysis. Nuclear Waste Management Organization Report, NWMO-TR-2021-16 R002. Toronto, Canada.

Goff, G.S., L.F. Brodnax, M.R. Cisneros, S.M. Peper, S.E. Field, B.I. Scott and W.H. Runde. 2008. First identification and thermodynamic characterization of the ternary U(VI) species, $UO_2(O_2)(CO_3)_2^{4-}$ in UO_2-H_2O_2-K_2CO_3 solutions. *Inorg Chem* 47: 1984-1990.

Goldik, J.S., H.W. Nesbitt, J.J. Noel and D.W. Shoesmith. 2004. Surface electrochemistry of UO_2 in dilute alkaline hydrogen peroxide solutions. *Electrochim Acta* 49: 1699-1709.

Goldik, J.S., J.J. Noel and D.W. Shoesmith. 2005. The electrochemical reduction of hydrogen peroxide on uranium dioxide electrodes in alkaline solution. *J Electroanal Chem* 582: 241-248.

Goldik, J.S., J.J. Noel and D.W.Shoesmith. 2006a. Surface electrochemistry of UO_2 in dilute alkaline hydrogen peroxide solutions. Effect of carbonate ions. *Electrochim Acta* 51: 3278-3286.

Goldik, J.S., J.J. Noel and D.W. Shoesmith, 2006b. The effects of simulated fission products in the reduction of hydrogen peroxide on simulated nuclear fuel electrodes. *J Electrochem Soc* 153: E151-E159.

Goldik, J.S., J.J. Noel and D.W. Shoesmith. 2006c. Surface electrochemistry of UO_2 in dilute alkaline hydrogen peroxide solutions. Effects of carbonate ions. *Electrochim Acta* 51: 3278-3286.

Grambow, B., A, Loida, P. Dresser, H. Geckeis, J. Gago, I. Casas, J. de Pablo, J.Gimenez, M.E. Torrero. 1996a. Long term safety of radioactive waste disposal: chemical reaction of fabricated and high burn-up spent UO_2 fuel with saline brines. Forschungszentrum Karlsruhe Report, FZKA 5702. Germany.

Grambow, B., A. Loida, A. Martinez Esparza, P. Diaz-Arocas, J. de Pablo, G. Marse, J.-P. Glatz, K. Lemmens, K. Ollila and H. Christensen. 2000. Source term for performance assessment of spent fuel as a waste form. European Commission, Nuclear Science and Technology Report, EUR 19140EN. Belgium.

Grambow, B., E. Smailos, H. Geckeis, R. Muller and H. Hentschel. 1996b. Sorption and reduction of uranium (VI) on iron corrosion products under reducing saline conditions. *Radiochim Acta* 74: 149-154.

Grambow, B.G. and E. Giffaut. 2006. Coupling of chemical processes in the near field. *Mater Res Soc Symp P* 932: 55-66.

Grambow, B., J. Bruno, L. Duro, J. Merino, A. Tamayo, C. Martin, G. Pepin, S. Schumacher, O. Smidt, C. Ferry, C. Jegou, J. Quinones, E. Iglesias, N. Rodriguez Villagra, J.M. Nieto, A. Martinez-Esparza, A. Loida, V. Metz, B. Kienzler, G. Bracke, D. Pellegrini, G. Mathieu, V. Wasselin-Trupin, S. Serres, D. Wegen, M. Jonsson, L.H. Johnson, K. Lemmens, J. Liu, K. Spahiu, E. Ekeroth, I. Casas, J. de Pablo, C. Watson, P. Robinson and D. Hodgkinson. 2010. Model uncertainty for the mechanism of dissolution of spent fuel in a nuclear waste repository. European Commission, Nuclear Science and Technology Report, EUR 24597EN.

Grambow, B., C. Ferry, I. Casas, J. Bruno, J. Quinones and L.H. Johnson. 2011. Spent fuel waste disposal: analysis of model uncertainty in the MICADO project. *Enrgy Proced* 7: 487-494.

Grambow, B., K. Lemmens, Y. Minet, C. Poinssot, K. Spahiu, D. Bosbach, C. Cachoir, I. Casas, F. Clarens, B. Christiansen, J. de Pablo, C. Ferry, J. Gimenez, S. Gin, J.P. Glatz, J. Gago, E. Gonzalez Robles, N.C. Hyatt, E. Iglesias, B. Kienzler, B. Luckscheiter, A. Martinez Esparza Valiente, V. Metz, A. Odegaard-Jensen, K.Ollila, J. Quinones, A. Rey, S. Ribet, V. Rondinella, G. Skarnemark, D. Wegen, D. Serrano-Purroy and T. Wiss. 2008. NF-Pro Final synthesis report RTD component 1: Dissolution and release from the waste matrix. European Commission, Nuclear Science and Technology Deliverable, D1.6.3. Bruxelles, Belgium.

Grandstaff, D.E. 1976. A kinetic study of the dissolution of uraninite. *Econ Geol Bull Soc* 71: 1493-1506.

Gray, W.J. 1988. Effect of surface oxidation, alpha radiolysis and salt brine composition on spent fuel and UO2 leaching experiments: salt repository project. Pacific Northwest Lab Report, PNL/SRP-6689. Richland, WA, USA.

Gray, W.J., D.M. Strachan and C.N. Wilson. 1991. Gap and grain boundary inventories of Cs, Tc, Sr in spent LWR fuel. *Mater Res Soc Symp P* 257: 353-360.

Grenthe, I., J. Fuger, R.J. Konings, R.L. Lemire, A.B. Mueller, C. Nguyen-Trung and H. Wanner. 1992. Chemical thermodynamics of uranium. North Holland, Amsterdam.

Guillamont, R., X. Gaona, A.V. Plyasunov, L. Rao, W.H. Runde, B. Grambow, R.J.M. Konings, A.L. Smith and E.E. Moore. 2020. Second update on the chemical thermodynamics of uranium, neptunium, plutonium, americium and technetium. OECD-NEA Chemical Thermodynamics Vol. 14: 207-211. Elsevier, Amsterdam.

Gupta, F., G. Brillant and A. Pasturel. 2007. Correlation effects and energetics of point defects in uranium dioxide. A first principles investigation. *Philos Mag* 87: 2561-2569.

Ha. Y.K., Y.H. Cho, J.G. Kim, K.Y. Jee and W.H. Kim. 2006. Air-Oxidation Behaviour of UO_2 and Gd-doped UO_2 by XAS. In Recent Advances in Actinide Science (I.L. May, N.D. Bryan and R. Alvares, eds.). United Kingdom. 782-784.

Hall, D.S., M. Behazin, W.J. Binns and P.G. Keech 2021. An evaluation of corrosion processes affecting copper-coated nuclear waste containers in a deep geological repository. *Prog Mater Sci* 118: 100766.

Hanson, B., B. McNamara, E.C. Buck, J. Friese, E. Jensen, K. Krupka and B. Arey. 2005. Corrosion of commercial spent fuel/Formation of studtite and metastudtite. *Radiochim Acta* 93: 159-168.

Hanson, B.D. 1998. The burn-up dependence of light water reactor spent fuel oxidation. Pacific Northwest Laboratories Report, PNNL-11929. Richland, USA.

Hansson, N.L., P.L. Tam, C. Ekberg and K. Spahiu. 2021. XPS study of external α-radiolytic oxidation of UO_2 in the presence of Ar or H_2. *J Nucl Mater* 543: 152604.

Haschke, J.M., T.H. Allen and J.L. Stakebake. 1996. Reaction kinetics of plutonium with oxygen, water and humid air. *J Alloy Compd* 243: 23-35.

Haschke, J.M., T.H. Allen and L.A. Morales. 2000. Reaction of plutonium dioxide with water; Formation and properties of PuO_{2+x}. *Science* 287: 285-287.

Hastings, I. 1982. Structures in irradiated UO_2 fuel from Canadian reactors. Atomic Energy of Canada Limited Report, AECL-MISC-249. Chalk River, Canada.

Hastings, I.J., M.J.F. Notley and D.H. Rose. 1978. Irradiation-induced volume changes in commercial UO_2 fuel: comparison with model predictions. *J Nucl Mater* 75: 301-303.

He, H. 2010. The influence of non-stoichiometry and rare earth doping on the oxidation and dissolution of uranium dioxide. Ph.D. Thesis, University of Western Ontario.

He, H. and D.W. Shoesmith. 2010. Raman spectroscopic studies of defect structures and phase transitions in hyperstoichiometric UO_{2+x}. *Phys Chem Chem Phys* 12: 8108-8117.

He, H., Z. Ding and D.W.Shoesmith. 2009a. The determination of electrochemical reactivity and sustainability on individual hyper-stoichiometric UO_{2+x} grains by Raman microspectroscopy and scanning electrochemical microscopy. *Electrochem Commun* 11: 1724-1727.

He, H., R.K. Zhu, Z. Qin, P. Keech, Z. Ding and D.W. Shoesmith. 2009b. Determination of local corrosion kinetics on hyperstoichiometric UO_{2+x} by scanning electrochemical microscopy. *J Electrochem Soc* 156: C87-C94.

He, H., Z. Qin and D.W. Shoesmith. 2010. Characterizing the relationship between hyperstoichiometry, defect structure and local corrosion kinetics of uranium dioxide. *Electrochim Acta* 56: 53-60.

He, H., P.G. Keech, M.E. Broczkowski, J.J. Noel and D.W. Shoesmith. 2007. Characterization of the influence of fission product doping on the anodic reactivity of uranium dioxide. *Can J Chem* 85: 1.

Heckmann, K. and J. Edward. 2020. Radionuclide inventory for reference CANDU fuel bundles. Nuclear Waste Management Organization Technical Report, NWMO-TR-2020-05. Toronto, Canada.

Herrero, B., R. Bes, F. Audubert, N. Clavier, Myrtille O.J.Y. Hunault and G.Baldinozzi. 2020. Charge compensation mechanisms in Nd-doped UO_2 samples for stoichiometric and hyper-stoichiometric conditions: lack of miscibility gap. *J Nucl Mater* 539: 152276.

Hill, S.L.W., N. Liu, Z. Qin, D, Zagidulin and D.W. Shoesmith. 2015. Interactions between carbon steel and UO_2 corrosion fronts inside a failed nuclear waste container. Proceedings of the 17th International Conference on Environmental Degradation of Materials in Nuclear Power Systems: Water Reactors. August 9-12, Ottawa, ON, Canada.

Hiroki, A. and J.A. LaVerne. 2005. Decomposition of hydrogen peroxide at water-ceramic oxide interfaces. *J Phys Chem B* 109: 3364-3370.

Hiskey, J.B. 1980. Hydrogen peroxide leaching of uranium in carbonate solutions. *T I Min Metall C* 89: C145-C152.

Hocking, W., J.S. Betteridge and D.W. Shoesmith. 1991. The cathodic reduction of oxygen on uranium dioxide in dilute alkaline aqueous solution, Atomic Energy of Canada Limited Report, AECL-10402. Chalk River, Canada.

Hocking, W., J.S. Betteridge and D.W. Shoesmith. 1994. The cathodic reduction of oxygen on uranium dioxide in dilute alkaline aqueous solution. *J Electroanal Chem* 379: 339-351.

Hossain, M.M., E. Ekeroth and M. Jonsson. 2006. Effects of HCO_3^- on the kinetics of UO_2 oxidation by H_2O_2. *J Nucl Mater* 358: 202-208.

Hua, B., H. Xu, J. Terry and B. Deng. 2006. Kinetics of uranium (VI) reduction by hydrogen sulfide in anoxic aqueous systems. *Environ Sci Technol* 40, 4666-4671.

Idriss, H. 2010. Surface reactions of uranium dioxide, thin films and single crystals. *Surf Sci Rep* 65: 67-109.

Ilin, S.R., K. Spahiu and U-B. Eklund. 2001. Determination of dissolution rates of spent fuel in carbonate solutions under different redox conditions with a flow-through experiment. *J Nucl Mater* 297: 231-243.

Ilton, E.S., A. Haiduc, C.L. Cahil and A.R. Felny. 2005. Mica surfaces stabilize pentavalent uranium. *Inorg Chem* 44: 2986-2988.

Ilton, E.S., J.F. Boily and P. Bagus. 2007. Beam induced reduction of U(VI) during X-ray photoelectron spectroscopy; the utility of the U4f satellite structure for identifying uranium oxidation states in mixed valence uranium oxides. *Surf Sci* 601: 908-916.

Janecek, J., R.C. Ewing, V.M. Oversby and L.O. Werme. 1996. Uraninite and UO_2 in spent fuel: a comparison. *J Nucl Mater* 238: 121-130.

Jansson, M. 1996. Water Radiolysis in Cigar lake. In A Reappraisal of Some Cigar Lake Issues of Importance to Performance Assessment (J. Smellie and F. Karlsson, eds.). Swedish Nuclear Fuel and Waste Management Company Report, SKB-TR-96-08. Stockholm, Sweden.

Jegou, C., B. Muzeau, V. Broudic, S. Peuget, A. Poulesquen, D. Rondil and C. Corbel. 2005a. Effect of external gamma irradiation on dissolution of the spent UO2 fuel matrix. *J Nucl Mater* 341: 62-82.

Jegou, C., B. Muzeau, V. Broudic, A. Pulesquen, D. Roudil, F. Jorion and C. Corbel. 2005b. Effect of alpha irradiation on UO2 surface reactivity. *Radiochim Acta* 93: 35-42.

Jerden, J.L., K. Frey and W. Ebert. 2015. A multiphase interfacial model for the dissolution of spent nuclear fuel. *J Nucl Mater* 462: 135-146.

Jinsong, L. and I. Neretnieks. 1996. A model for radiation energy deposition in natural uranium-bearing systems and its consequences to water radiolysis. *J Nucl Mater* 231: 103-112.

Johnson, L.H. and D.F. McGuinnes. 2002. Partitioning of radionuclides in Swiss power reactor fuels. Swiss National Cooperative for the disposal of radioactive waste. Nagra Technical Report 02-07. Wettingen, Switzerland.

Johnson, L.H. and D.W. Shoesmith. 1988. Spent Fuel. In Radioactive Waste Forms for the Future (W.B.Lutze and R.C.Ewing, eds.). Elsevier Science Publishers, Amsterdam, Netherlands.

Johnson, L.H. and P.A. Smith. 2000. The interaction of radiolysis products and canister corrosion products and the implications for spent fuel dissolution and radionuclide transport in a repository for spent fuel. Nagra Technical Report 00-04. Wettingen, Switzerland.

Johnson, L.H., C. Ferry, C. Poinssot and P. Lovera. 2005. Spent fuel radionuclide source term model for assessing spent fuel performance in geological disposal. Part 1: assessment of the instant release fraction. *J Nucl Mater* 346: 56-65.

Johnson, L.H., D.M. Leneveu, F. King, D.W. Shoesmith, M. Kolar, D.W. Oscarson, S. Sunder, C. Onofrei and J.L. Crosthwaite. 1996. The disposal of Canada's nuclear fuel waste: A study of post-closure safety of in-room emplacement of used CANDU fuel in copper containers in impermeable plutonic rock: Volume 2 – Vault model. Atomic Energy of Canada Limited Report, AECL-11494-2, COG-95-552-2. Pinawa, Canada.

Johnson. L.H., D.M. Leneveu, D.W. Shoesmith, D.W. Oscarson, M.N. Gray, R.J. Lemire and N.C. Garisto. 1994. The disposal of Canada's nuclear fuel waste: the vault model for post-closure assessment. Atomic Energy of Canada Limited Report, AECL-10714, COG-94-4. Pinawa, Canada.

Jonsson, M., E. Ekeroth and O. Roth. 2004. Dissolution of UO_2 by one and two electron oxidants. *Mater Res Soc Symp P* 807: 77-82.

Jonsson, M., F. Nielsen, O. Roth, E. Ekeroth, S. Nilsson and M.M. Hossain. 2007. Radiation induced spent nuclear fuel dissolution under deep repository conditions. *Environ Sci Technol* 41: 7087-7093.

Keech, P.G., J.J. Noël and D.W. Shoesmith. 2008. The electrochemical reduction of hydrogen peroxide on uranium dioxide under intermediate pH to acidic conditions. *Electrochim Acta* 53: 5675-5683.

Keech, P.G., J.S. Goldik and D.W. Shoesmith. 2011. The anodic dissolution of SIMFUEL (UO_2) in slightly alkaline sodium carbonate/bicarbonate solutions. *Electrochim Acta* 56: 7923-7930.

Kienzler, B., V. Metz and A. Valls. 2015. Fast/Instant release of safety relevant radionuclides from spent fuel. FIRST-Nuclides, Final Scientific Report; Deliverable 5.13. Luxembourg, Germany.

Kim, J., H.J. Kim, W.-S. Kim and W. Um. 2018. Dissolution of studtite [$UO_2O_2(H_2O)_4$ in various geochemical conditions. *J Environ Radioactiv* 189: 57-66.

Kim, J.D., S.I. Pyun, T.H. Yang and J.B. Ju. 1995. A study of the mechanism of oxygen reduction on bare palladium in 0.1M LiOD solution using a Pt Ring-Pd-disc electrode. *J Electroanal Chem* 383: 161-166.

King, F. and D.W. Shoesmith. 2004. Electrochemical studies of the effect of H_2 on UO_2 dissolution. Swedish Nuclear Fuel and Waste Management Company Report, TR-04-20. Stockholm, Sweden.

King, F. and M. Kolar. 1999. Mathematical implementation of the mixed-potential model of fuel dissolution model version MPM-V1. Ontario Hydro Report, No. 06819-REP-01200-10005-R00.

King, F. and M. Kolar. 2002. Validation of the mixed-potential model for used fuel dissolution against experimental data. Ontario Power Generation Report No. 06819-REP-01200-10077-R00.

King, F. and M. Kolar. 2003. The mixed-potential model for UO_2 dissolution: MPM versions V1.3 and V1.4. Ontario Power Generation Report, No. 06819-REP-01200-10104-R00.

King, F. and S. Stroes-Gascoyne. 2000. An assessment of the long term corrosion behaviour of C-steel and the impact of redox conditions inside a nuclear fuel waste disposal container. Ontario Power Generation Report, No. 06819-REP-01200-10028-R00.

King, F., D.S. Hall and P.G. Keech. 2017. Nature of the near-field environment in a deep geological repository and the implications for the corrosion behaviour of the container. *Corros Eng Sci Techn* 52 (S1): 25-30.

King, F., M. Kolář, I. Puigdomenech, P. Pitkänen and C. Lilja. 2020. Modeling microbial sulfate reduction and the consequences for corrosion of copper canisters. *Mater Corros* 72: 339-347.

King, F., M.J. Quinn and N.H. Miller. 1999. The effect of hydrogen and gamma radiation on the oxidation of UO_2 in 0.1 mol.L NaCl solution. Swedish Nuclear Fuel and Waste Management Company Report, TR-99-27. Stockholm, Sweden.

Kleykamp, H. 1985. The chemical state of fission products in oxide fuels. *J Nucl Mater* 131: 221-246.

Kleykamp, H. 1988. The chemical state of fission products in oxide fuels at different stages of the nuclear fuel cycle. *Nucl Technol* 80: 412-422.

Kleykamp, H. 1990. Post-irradiation examinations and composition of the residues from nitric acid dissolution experiments of high burn-up LWR fuel. *J Nucl Mater* 171: 181-188.

Kleykamp, H. 1993. The solubility of selected fission products in UO_2 and PuO_2. *J Nucl Mater* 206: 82-86.

Kleykamp, H., J.O. Paschoal, R. Pejsa, F. Thommler. 1985. Composition and structure of fission product precipitates in irradiated oxide fuels: Correlation with phase studies in the Mo-Ru-Rh-Pd and $BaO-UO_2-ZrO_2-MoO_2$ systems. *J Nucl Mater* 130: 426-433.

Kubatko, K.-A., D. Unruh and P.C. Burns. 2006. Affects of hydrogen peroxide on the stability of becquerelite. *Mater Res Soc Symp P* 893: JJ05-19.

Kubatko, K.A.H., K.B. Helean, A. Navrotsky and P.C. Burns. 2003. Stability of peroxide-containing uranyl minerals. *Science* 302: 1191-1193.

Kumagai, Y., M. Takano and M. Watanabe. 2017. Reaction of hydrogen peroxide with uranium zirconium oxide solid solution – Zirconium hinders oxidative dissolution. *J Nucl Mater* 497: 54-59.

Kumagai, Y. and M. Jonsson. 2020. Gamma Radiation and H_2O_2 induced oxidative dissolution of uranium (IV) oxide in aqueous solution containing phthalic acid. *Dalton T* 49: 1907-1914.

Kumagai, Y., A. Barriero Fidalgo and M.Jonsson. 2019. Impact of stoichiometry on the mechanism and kinetics of oxidative dissolution of UO_2 induced by H_2O_2 and γ-irradiation. *J Phys Chem C* 123: 9919-9925.

Lampman, T. 2019. Update to fuel burnups and power ratings. Nuclear Waste Management Organization Report, NWMO-TR-2019-04. Toronto, Canada.

Lee, C.T., M.S. Odziemkowski and D.W.Shoesmith. 2006a. An in-situ Raman-electrochemical investigation of carbon steel corrosion under anoxic conditions. *J Electrochem Soc* 153: B33-B41.

Lee, C.T., Z.Qin, M.S. Odziemkowski and D.W.Shoesmith. 2006b. The influence of groundwater anions on the impedance behaviour of carbon steel corroding under anoxic conditions. *Electrochim Acta* 51: 1558-1568.

Lee, J., C. Kwon, J. Kim, Y-S. Yoon, J-Y. Kim, B. Han and S.H. Lim. 2019. Integrated study of experimental and first-principles computations for the characterization of a corium-type ZrO_8 complex in a Zr-doped UO_2. *Int J Energ Res* 43: 3322-3329.

Lemire, R. and F. Garisto 1989. The solubility of U, Np, Pu, Th and Tc in a geological disposal vault for used nuclear fuel. Atomic Energy of Canada Limited Report, AECL-10009. Pinawa, Canada.

Lemire, R.J. and P.R. Tremaine. 1980. Uranium and plutonium equilibria in aqueous solutions to 200ºC. *J Chem Eng Data* 25: 361-370.

Lemmens, K., C. Cachoir, T. Mennecart. 2019. Dissolution behaviour of spent nuclear fuel at highly alkaline conditions. Phenomenological synthesis report. Belgian Nuclear Research Centre Report, SCK-CEN/27622175. Belgium.

Li, J., A.C. Maier and M. Jonsson. 2020. Stability of studtite in aqueous suspension: Impact of HCO_3^- and ionizing radiation on the dynamics of dissolution. *ACS Appl Energy Mater* 3: 352-357.

Li, J., Z.Szabó and M. Jonsson. 2021. Metastudtite stability in aqueous solutions. Impact of HCO_3^-, H_2O_2 and ionizing radiation on dissolution and speciation. *Dalton T* 50: 6568-6577.

Li, L., F. Chen, J.Q. Lu and M.F. Luo. 2011. Study of defect sites in $Ce_{1-x}M_xO_{2-\delta}$ solid solutions using Raman spectroscopy. *J Phys Chem A* 115: 7972-7977.

Lin, S-S. and M.D. Gurol. 1998. Catalytic decomposition of hydrogen peroxide on iron oxide; kinetics, mechanism and implications. *Environ Sci Technol* 32: 1417-1423.

Lindemer, T.B. and T.M.Bessman. 1985. Chemical thermodynamics representation of UO_{2+x}, *J Nucl Mater* 130: 473-488.

Liu, L. and I. Neretnieks. 2002. The effect of hydrogen on oxidative dissolution of spent fuel. *Nucl Technol* 138: 69-77.

Liu, N., F. King, J.J. Noël and D.W. Shoesmith. 2021. An electrochemical and radiolytic study of the effects of H_2 on the corrosion of UO_2-based materials. *Corros Sci* 192: 109776.

Liu, N., L. Wu, Z. Qin and D.W. Shoesmith. 2016. Roles of radiolytic and externally generated H_2 in the corrosion of fractured spent nuclear fuel. *Environ Sci Technol* 50: 12348-12355.

Liu, N., H. He, J.J. Noël and D.W. Shoesmith. 2017a. The electrochemical study of Dy_2O_3-doped UO_2 in slightly alkaline sodium carbonate/bicarbonate and phosphate solutions. *Electrochim Acta* 235: 654-663.

Liu, N., Z. Qin, J.J. Noel and D.W. Shoesmith. 2017b. Modelling the radiolytic corrosion of α-doped UO_2 and spent nuclear fuel. *J Nucl Mater* 494: 87-94.

Liu, N., J-D. Kim, J.M. Lee, Y-S. Youn, J-G. Kim, J-Y. Kim, J.J. Noel and D.W. Shoesmith. 2017c. Influence of Gd doping on the structure and electrochemical behaviour of UO_2. *Electrochim Acta* 247: 496-504.

Liu, N., Z. Zhu, J.J. Noel and D.W. Shoesmith. 2018. Corrosion of nuclear fuel inside a failed waste container. In Encyclopedia of Interfacial Chemistry (K. Wandelt ed.). 172-182.

Liu, N., Z. Zhu, L. Wu, Z. Qin, J.J. Noel and D.W. Shoesmith. 2019. Predicting radionuclide release rates from spent nuclear fuel inside a failed waste disposal container using a finite element model. *Corrosion* 75: 302-308.

Livens, F.R., M.J. Jones, A.J. Hynes, J.M. Charnock, J.F.W. Mosselmans, C. Hennig, H. Steele, D. Collison, D.J. Vaughan. R.A.D. Pattrick, W.H. Reed and L.N. Moyes. 2004. X-ray absorption spectroscopy studies of reactions of technetium, uranium, and neptunium with mackinawite. *J Environ Radioactiv* 74: 211-219.

Loida, A., B. Grambow and H. Geckeis. 1996. Anoxic corrosion of various high burn-up spent fuel samples. *J Nucl Mater* 238: 11-22.

Loida, A., B. Grambow and H. Geckeis. 2001a. Congruent and incongruent radionuclide release during matrix dissolution of partly oxidized high burn-up spent fuel. *Mater Res Soc Symp P* 663: 417-426.

Loida, A., B. Grambow and H. Geckeis. 2001b. Spent fuel corrosion behaviour in salt solution in the presence of hydrogen overpressure. In Proc. ICEM'01, 8th International Conference on Radioactive Waste Management. Bruges, Belgium.

Loida, A., B. Grambow, H. Geckeis and P. Dressler. 1995. Processes controlling radionuclide release from spent fuel. *Mater Res Soc Symp P* 352: 577-584.

Loida, A., M.Kelm, B. Kienzler, B.Geckeis and A. Bauer. 2006. The effect of near field constraints on the corrosion behaviour of high burn-up spent fuel. *Mater Res Soc Symp P* 932: 473-480.

Loida, A., V. Metz, B. Kienzler and H. Geckeis. 2005. Radionuclide release from high burn-up spent fuel during corrosion in salt brine in the presence of hydrogen overpressure. *J Nucl Mater* 346: 24-31.

Lousada, C.M. and M. Jonsson. 2010. Kinetics, mechanism, and activation energy of H_2O_2 decomposition on the surface of ZrO_2. *J Phys Chem C* 114: 11202-11208.

Lousada, C.M. M. Yang, K. Nilsson and M. Jonsson. 2013a. Catalytic decomposition of hydrogen peroxide on transition metal and lanthanide oxides. *J Mol Catal A-Chem* 379: 178-184.

Lousada, C.M., A.J. Johansson and T. Brinck. 2013b. Reactivity of metal oxide clusters with hydrogen peroxide and water – a DFT study evaluating the performance of different exchange-correlation functionals. *Phys Chem Chem Phys* 15: 5539-5552.

Lousada, C.M., A.J. Johansson, T. Brinck and M. Jonsson. 2012. Mechanism of H_2O_2 decomposition on transition metal oxide surfaces. *J Phys Chem C* 116: 9533-9543.

Lousada, C.M., M. Trummer and M. Jonsson. 2013c. Reactivity of H_2O_2 towards different UO_2-based materials: the relative impact of radiolysis revisited. *J Nucl Mater* 434: 434-439.

Lovera, P., C. Ferry, C. Poinssot, L.H. Johnson. 2003. Synthesis report on the relevant diffusion coefficients of fission products and helium in spent nuclear fuels. French Alternative Energies and Atomic Energy Commission Report, CEA-R-6039. Gif-sur-Yvette, France.

Lucuta, P.G., R.A. Verrall, H. Matzke and B.J. Palmer. 1991. Microstructural features of SIMFUEL – Simulated high-burnup UO_2-based nuclear fuel. *J Nucl Mater* 178: 48-60

Luht, J.L.M. 1998. Anodic dissolution of uranium dioxide in simple electrolyte solutions and simulated groundwaters. M.Sc. Thesis, University of Manitoba, Winnipeg, MB, Canada.

Lumpkin, G.R. and T. Geisler-Wierwille. 2012. 5.22 – Minerals and natural analogues. In Comprehensive Nuclear Materials Volume 5: Materials performance and corrosion/waste materials (R.J.M. Konings, T.R. Allen, R.E. Stoller, S. Tamanaka, eds.). New York, USA. 563-600.

Maia, F.M.S., S. Ribet, C, Bailly, M. Grivé, B. Madé and G. Montavon. 2021. Evaluation of thermodynamic data for aqueous Ca-U(VI)-CO_3 species under conditions characteristic of geological clay formation. *Appl Geochem* 124: 104844.

Maier, A.C., P. Kegler, M. Klinkenberg, A. Baena, S. Finkeldei, F. Brandt and M. Jonsson. 2020. On the change in UO_2 redox reactivity as a function of H_2O_2 exposure. *Dalton T* 49: 1241-1248.

Martinovic, J.M., D.B. Sepa, M.V. Vojnovic and A. Damjanovic. 1988. Kinetics of electrochemical reduction of oxygen at rhodium. *Electrochim Acta* 33: 1267-1272.

Matzke, H and Hj Matzke. 1995. Oxygen potential measurements in high burn-up LWR UO_2 fuel. *J Nucl Mater* 223: 1-5.

Matzke, Hj. 1982. Radiation damage in crystalline insulators, oxides, and ceramic nuclear fuels. *Radiat Eff Defect S* 64: 3-33.

McEachern, R.J. 1997. A review of kinetic data on the rate of U_3O_7 formation on UO_2. *J Nucl Mater* 245: 238-247.

McEachern, R.J. and P.Taylor. 1998. A review of the oxidation of uranium dioxide at temperatures below 400°C. *J Nucl Mater* 254: 87-121.

McEachern, R.J., D.C. Doern and D.D. Wood. 1998. The effect of rare earth fission products on the rate of U_3O_8 formation on UO_2. *J Nucl Mater* 252: 145-149.

McNamara, B., E.C. Buck, B. Hanson. 2002. Observation of studtite and metastudtite on spent fuel. *Mater Res Soc Symp P* 757: II9.7.

Merino, J., E. Cera, J. Bruno, J. Quinones, I. Casas, F. Clarens, J.Gimenez, J. de Pablo, M. Rovira and A. Martinez-Esparza. 2005. Radiolytic modelling of spent fuel oxidative dissolution mechanism. Calibration against UO_2 dynamic leaching experiments. *J Nucl Mater* 346: 40-47.

Mohun, R., L. Desgranges, A. Canizares, N. Raimboux, F. Duval, R. Omnee, C. Jegou, S. Miro and P. Simon. 2018. Investigating the role of irradiation defects during UO_2 oxidative dissolution. *J Nucl Mater* 509: 305-312.

Moyes, L.N., R.H. Parkman, J.M. Charnock, D.J. Vaughan, F.R. Livens, C.R. Hughes and A. Braithwaite. 2000. Uranium uptake from aqueous solution by interaction with goethite, lepidocrocite, muscovite and mackinawite: An X-ray absorption spectroscopy study. *Environ Sci Technol* 34: 1062-1068.

Mühr-Ebert, E.L., F.Wagner and C.Walther. 2019. Speciation of uranium: Compilation of the thermodynamic database and its experimental evaluation using different analytical techniques. *Appl Geochem* 100: 213-222.

Muzeau, B., C. Jégou, F. Delaunay, V. Broudic, A. Brevet, H. Catalette, E. Simoni and C.Corbel. 2009. Radiolytic oxidation of UO_2 pellets doped with alpha emitters (^{238}Pu,^{239}Pu). *J Alloy Compd* 467: 578-589.

Neck, V and J.I. Kim. 2001. Solubility and hydrolysis of tetravalent actinides. *Radiochim Acta* 89: 1-16.

Nerikar, P., T. Watanabe, J.S. Tulenko, S.R. Phillpot and S.B. Sinnott. 2009. Energetics of intrinsic point defects in uranium dioxide from electronic structure calculations. *J Nucl Mater* 384: 61-69.

Nicol, M.J. and C.R.S. Needes. 1973. The mechanism of the anodic dissolution of uranium dioxide, Nat. Inst. Met. Report, No. 7079. Republic of South Africa.

Nicol, M.J. and C.R.S. Needes. 1975. The anodic dissolution of uranium dioxide - 1 In perchlorate solutions. *Electrochim Acta* 20: 585-589.

Nielsen, F. and M. Jonsson. 2006. Geometrical α and β dose distributions and production rates of radiolysis products in water in contact with spent nuclear fuel. *J Nucl Mater* 359: 1-7.

Nielsen, F., O. Roth, E. Ekeroth, S. Nilsson, M.M. Hossain and M. Jonsson. 2007. Radiation-induced spent nuclear fuel dissolution under deep repository conditions. *Environ Sci Technol* 41: 7087-7093.

Nielsen, F., K. Lundahl and M. Jonsson. 2008. Simulations of H_2O_2 concentration profiles in water surrounding spent nuclear fuel. *J Nucl Mater* 372: 32-35.

Nielsen F. and M. Jonsson. 2008. Simulations of H_2O_2 concentration profiles in the water surrounding spent nuclear fuel taking mixed radiation fields and bulk reactions into account. *J Nucl Mater* 374: 281-285.

Nilsson, S. 2008. Influence of metallic fission products and self irradiation on the rate of spent nuclear fuel-matrix dissolution. Licentiate Thesis in Chemistry, Royal Institute of Technology, Stockholm.

Nilsson, S. and M. Jonsson. 2007. On the catalytic effects of UO_2(s) and Pd(s) on the reaction between H_2O_2 and H_2 in aqueous solution. *J Nucl Mater* 372: 160-163.

Nilsson, S. and M. Jonsson. 2008. On the catalytic effects of $UO_2(s)$ and $Pd(s)$ on the reduction of UO_2^{2+} with H_2 in aqueous solution. *J Nucl Mater* 374: 290-292.

Nilsson, S. and M. Jonsson. 2011. H_2O_2 and radiation-induced dissolution of UO_2 and SIMFUEL. *J Nucl Mater* 410: 89-93.

Norskov, J.K., T. Bligaard, A. Lagodottir, J.R. Kitchin, J.G. Chen, S. Pandelov and U. Stimming. 2005. Trends in exchange currents for hydrogen evolution. *J Electrochem Soc* 152: J23-J26.

NWMO (Nuclear Waste Management Organization). 2017. Postclosure Safety Assessment of A Used Fuel Repository in Crystalline Rock. Nuclear Waste Management Organization Technical Report, NWMO-TR-2017-02. Toronto, Canada.NWMO (Nuclear Waste Management Organization). 2018. Postclosure Safety Assessment of A Used Fuel Repository in Sedimentary Rock. Nuclear Waste Management Organization Technical Report, NWMO-TR-2018-08. Toronto, Canada.

NWMO (Nuclear Waste Management Organization). 2019. RD 2019 – NWMO's Program for Research and Development for Long-Term Management of Used Nuclear Fuel. Nuclear Waste Management Organization Technical Report, NWMO-TR-2019-18. Toronto, Canada.

Odorowski, M., C. Jegou, L. De Windt, V. Broudic, G. Jouan, S. Peuget and C. Martin. 2017. Effect of metallic iron on the oxidative dissolution of UO_2 doped with a radioactive α-emitter in synthetic Callovian-Oxfordian groundwater. *Geochim Cosmochim Ac* 219: 1-21.

Ofori, D., P.G. Keech, J.J. Noël and D.W.Shoesmith. 2010. The influence of deposited films on the anodic dissolution of uranium dioxide, *J Nucl Mater* 400: 84-93.

Ofori. D. 2008. The influence of corrosion product deposits on UO_2 corrosion/dissolution. Ph.D. Thesis, The University of Western Ontario, London, Canada.

Ollila, K., Y. Abinsson, V. Oversby and M. Cowper. 2003. Dissolution rates of unirradiated UO_2, UO_2 doped with ^{233}U and spent fuel under normal atmospheric conditions and under reducing conditions using an isotope dilution method. Swedish Nuclear Fuel and Waste Management Company Technical Report, TR-03-13. Stockholm, Sweden.

Ollila, K.Y. 2008. Dissolution of unirradiated UO_2 and UO_2 doped with ^{233}U in low- and high-ionic strength NaCl under anoxic and reducing conditions. POSIVA Working Report, 2008-50. Eurajoki, Finland.

Oversby, V. 2000. Rates and mechanisms of radionuclide release and retention inside a waste disposal canister, In Can Processes. European Commission Final Report FIKW-CT-2000-00019. Bruxelles, Belgium.

Oversby, V.M. 1999. Uranium dioxide, SIMFUEL, and spent fuel dissolution rates – A review of published data. Swedish Nuclear Fuel and Waste Management Company Technical Report, TR-99-22. Stockholm, Sweden.

Paquette, J. and R.L. Lemire. 1981. A description of the chemistry of aqueous solutions of uranium and plutonium to 200^0C using potential-pH diagrams. *Nucl Sci Eng* 79: 26-48.

Park, K. and D.R. Olander. 1990. The stoichiometry and the oxygen potential change of urania fuels during irradiation. *High Temp Sci* 29: 203-211.

Park, K. and D.R. Olander. 1992. Defect models for the oxygen potentials of gadolinium- and europium-doped Urania. *J Nucl Mater* 187: 89-96.

Parks, G.A and D.C. Pohl. 1988. Hydrothermal solubility of uraninite. *Geochim Cosmochim Ac* 52: 863-875.

Pastina, B. and J.A. LaVerne. 2001. Effect of molecular hydrogen on hydrogen peroxide in water radiolysis. *J Phys Chem A* 105: 9316-9322.

Pastina, B. and J.A. LaVerne. 2021. An alternative conceptual model for the spent nuclear fuel-water interaction in deep geologic disposal conditions. *Appl Sci* 11, 8566.

Pastina, B., J. Isabey and B. Hickel. 1999. The influence of water chemistry on the radiolysis of primary coolant water in preesurized water reactors. *J Nucl Mater* 264: 309-318.

Pehrman, R., M. Trummer, C.M. Lousada and M. Jonsson. 2012. On the redox reactivity of doped UO_2 pellets – Influence of dopants on the H_2O_2 decomposition mechanism. *J Nucl Mater* 430: 6-11.

Pencer, J., M.H. McDonald, D. Roubtsov and G.W.R. Edwards. 2017. Implications of alpha-decay for long-term storage of advanced heavy water reactor fuels. *Ann Nucl Energy* 110: 400-405.

Peper, S.M., L.F. Brodnax, S.E. Field, R.A. Zehner, S.N. Valdez and W.H. Runde. 2004. Kinetic study of the oxidative dissolution of UO_2 in aqueous carbonate media. *Ind Eng Chem Res* 43: 8188-8193.

Pierce, E.M., J.P. Icenhower, R.J. Serne and J.G. Catalano. 2005. Experimental determination of UO_2(cr) dissolution kinetics: Effects of solution saturation state and pH. *J Nucl Mater* 345: 206-218.

Poinssot, C., C. Ferry, M. Kelm, B. Grambow, A. Martinez-Esparza Valiente, L.H.Johnson, Z. Andriambololona, J. Bruno, C. Cachoir, C.Jegou, K. Lemmens, A.Loida, P. Lovera, F.Miserque, J. de Pablo, A. Poulesquen, J. Quinones, V. Rondinella, K. Spahiu and D. Wegen. 2005. Spent fuel stability under repository conditions: Final report of the European Project. French Alternative Energies and Atomic Energy Commission Report, CEA-R-6039. Gif-sur-Yvette, France.

Poinssot, C., C. Ferry, B. Grambow, M. Kelm, K. Spahiu, A. Martinez, L. Johnson, E. Cera, J. de Pablo, J. Quinones, D. Wegen, K. Lemmens and T. McMenamin. 2006. Mechanisms governing the release of radionuclides from spent nuclear fuel in a geological repository: Major outcomes of the European Project SFS. *Mater Res Soc Symp P* 932: 421-432.

Popel, A.J., V.G. Petrov, V.A. Lebedev, J. Day, S.N. Kalmykov, R. Springell, T.B. Scott and I. Farnan. 2017. The effect of fission-energy Xe ion irradiation on dissolution of thin films. *J Alloy Compd* 721: 586-592.

Popel, A.J., T.W. Wietsma, M.H. Engelhard, A.S. Lea, O. Qafoku, C. Grygiel, I. Monnet, E.S. Ilton, M.E. Bowden and I. Farnan. 2018. The effect of ion irradiation on the dissolution of UO_2 and UO_2-based simulant fuel. *J Alloy Compd* 735: 1350-1356.

Popel, A.J., B.T. Tan, T. Gouder, G.I. Lampronti, J.Day, R. Eliordi, A. Siebert and I. Farnan. 2019. Surface alteration evidence for a mechanism of anoxic dissolution of UO_2. *Appl Surf Sci* 464: 376-379.

Popel, A.J., S.P. Spurgeon, B. Matthews, M.J. Olszta, B.T. Tan, T. Gouder, R. Eliordi, E.C. Buck and I. Farnan. 2020. An atomic scale understanding of UO_2 surface evolution during anoxic dissolution. *ACS Appl Mater Inter* 12: 39781-39786.

Poulesquen, A., C. Jegou and S.Peuget. 2006. Determination of alpha dose rate profile at the UO_2/water interface. *Mater Res Soc Symp P* 932: 505-512.

Puranen, A., A. Barreiro, L.Z. Evins and K. Spahiu. 2016. Spent fuel leaching in the presence of corroding iron. *MRS Adv* 2: 681-686.

Puranen, A., A. Barreiro, L.-Z. Evins and K. Spahiu. 2020. Spent fuel corrosion and the impact of Fe corrosion – The effects of hydrogen generation and formation of iron corrosion products. *J Nucl Mater* 542: 152423.

Qin, Z., W-J. Cheong, P.G. Keech, J.C. Wren and D.W. Shoesmith. 2014. Modelling development of acidification within corroding sites on spent fuel surfaces. *Corr Eng Sci Technol* 49: 583-587.

Quinones, J., J.A. Serrano, P. Diaz-Arocas, J.-L. Rodriguez-Almazan, J. Cobos, J.A. Esteban and A. Martinez-Esparza. 2001. Influence of container base material (Fe) on SIMFUEL leaching behaviour. *Mater Res Soc Symp P* 663: 435-439.

Rai, D., A.R. Felmy and J.L. Ryan. 1990. Uranium (IV) hydrolysis constants and solubility product of $UO_2 \cdot xH_2O$(am). *Inorg Chem* 29: 260-264.

Rai, D., M. Yui and D.A. Moore. 2003. Solubility and solubility product at 22°C of UO_2(c) precipitated from aqueous U(IV) solutions. *J Solution Chem* 32: 1-17.

Razdan, M. and D.W. Shoesmith. 2015. The influence of hydrogen peroxide and hydrogen on the corrosion of simulated spent nuclear fuel. *Faraday Discuss* 180: 283-299.

Razdan, M. and D.W. Shoesmith. 2014a. Influence of trivalent dopants on the structural and electrochemical properties of uranium dioxide (UO_2). *J Electrochem Soc* 161: H105-H113.

Razdan, M. and D.W. Shoesmith. 2014b. The electrochemical reactivity of 6.0wt% Gd-doped UO_2 in aqueous carbonate/bicarbonate solutions. *J Electrochem Soc* 161: H225-H234.

Razdan, M., D.S. Hall, P.G. Keech and D.W. Shoesmith. 2012. Electrochemical reduction of hydrogen peroxide on SIMFUEL (UO_2) in acidic pH conditions. *Electrochim Acta* 83: 410-419.

Rey, A., S. Utsunomiya, J. Gimenej, I. Casas, J. de Pablo and R.C.Ewing. 2009. Stability of uranium (VI) peroxide hydrates under ionizing radiation. *Am Mineral* 94: 229-235.

Robit-Pointeau, V., C. Poinssot, P. Vitarge, B. Grambow, D. Cui, K. Spahiu and H. Catalette. 2006. Assessment of the relevance of coffinite formation within the near-field environment of spent nuclear fuel geological disposals. *Mater Res Soc Symp P* 932: 489-495.

Rondinella, V.V. and T. Wiss. 2010. The high burn-up structure in nuclear fuel. *Mater Today* 13: 24-32.

Rondinella, V.V., Hj. Matzke, C.J. Cobos and T. Wiss. 2000. Leaching behaviour of UO_2-containing α-emitting actinides. *Radiochim Acta* 88: 527-532.

Rondinella, V.V., Hj. Matzke, J. Cobos and T. Wiss. 2011. Alpha radiolysis and α-radiation damage effects on UO_2 dissolution under spent fuel storage conditions. *Mater Res Soc Symp P* 556: 447-454.

Roth, O., C. Askeljung, A. Puranen, K.Johnson, D. Jädernäs, A. Barreiro-Fidalgo, L.-Z. Evins and K. Spahiu. 2021. Investigation of secondary phases formed during long-term aqueous leaching of spent nuclear fuel. *MRS Adv* 6: 90-94

Roudil, D., C. Jegou, V. Broudic, M. Tribet. 2009. Rim instant release radionuclide inventory from French burn-up spent MOX fuel. *Mater Res Soc Symp P* 1193: 627-633.

Roudil, D., C. Jegou, V. Broudic, B. Muzeau, S. Peuget, X. Deschanels. 2007. Gap and grain boundary inventories from pressurized water reactor spent fuel. *J Nucl Mater* 362: 411-415.

Rudnicki, J.D., R.E. Russo and D.W. Shoesmith. 1994. Photothermal deflection spectroscopy investigations of uranium dioxide oxidation. *J Electroanal Chem* 372: 63-74.

Röllin, S., K. Spahiu and U.-B. Eklund. 2001. Determination of dissolution rates of spent fuel in carbonate solutions under different redox conditions with a flow-through experiment. *J Nucl Mater* 297: 231-243.

Saleh, S.C., C. Cachoir, K. Lemmens and N. Maes. 2006. Static dissolution tests of alpha-doped UO_2 under repository relevant conditions: Influence of Boom clay and alpha activity on fuel dissolution rates. *Mater Res Soc Symp P* 932: 481-488.

Santos, B.G., H.W. Nesbitt, J.J. Noël and D.W. Shoesmith. 2004. X-ray photoelectron spectroscopy study of anodically oxidized SIMFUEL surfaces. *Electrochim Acta* 49: 1863-1873.

Santos, B.G., J.J. Noël and D.W. Shoesmith. 2006a. The influence of calcium ions on the development of acidity in corrosion product deposits on SIMFUEL (UO_2). *J Nucl Mater* 350: 320-331.

Santos, B.G., J.J. Noël and D.W. Shoesmith. 2006b. The influence of silicate on the development of acidity in corrosion product deposits on SIMFUEL. *Corros.Sci* 48: 3852-3868.

Santos, B.G., J.J. Noël and D.W. Shoesmith. 2006c. The effect of pH on the anodic dissolution of SIMFUEL (UO_2). *J Electroanal Chem* 586: 1-11.

Sattonay, G., C. Ardois, C. Corbel, J.F. Lucchini, M.-F. Barthe, F. Garrido and D. Gosset. 2001. Alpha radiolysis effects on UO_2 alteration in water. *J Nucl Mater* 288: 11-19.

Schindler, M., F.C.Hawthorne, M.S. Freund and P.C. Burns. 2009. XPS spectra of uranyl minerals and synthetic uranyl compounds. I – The U 4f spectrum. *Geochim Cosmochim Ac* 73: 2471-2487.

Scott, P.D., D. Glasser and M.J. Nicol. 1977. Kinetics of dissolution of β-uranium trioxide in acid and carbonate solutions. *J Chem Soc Dalton* 139: 1939-1946.

Segall, R.L., R.S.C. Smart and P.S. Turner. 1988. Chapter 13. In Surface and near Surface Chemistry of Oxide Minerals. Elsevier Science, Amsterdam.

Sellin, P. 2002. SR97: Hydromechanical evolution in a defective container. *Mater Res Soc Symp P* 663: 755-763.

Senanayake, S.D., G.I.N. Waterhouse, A.S.Y. Chan, T.E. Madey, D.R. Mullins and H. Idriss. 2007. The reactions of water vapour on the surfaces of stoichiometric and reduced uranium dioxide: a high resolution XPS study. *Catal Today* 120: 151-157.

Shoesmith, D.W. 2000. Fuel corrosion processes under waste disposal conditions. *J Nucl Mater* 282: 1-31.

Shoesmith, D.W. 2007. Used fuel and uranium dioxide dissolution studies – A review. Nuclear Waste Management Organization Technical Report, TR-2007-03. Toronto, Canada.

Shoesmith, D.W. and F. King. 1998. A mixed potential model for the prediction of the effects of alpha radiolysis, precipitation, and redox processes on the dissolution of used nuclear fuel. Ontario Power Generation Report, No: 06819-REP-01200-0038-R00. Pinawa, Canada.

Shoesmith, D.W. and S. Sunder. 1991. An electrochemically-based model for the dissolution of UO_2. Atomic Energy of Canada Limited Report, AECL-10488. Pinawa, Canada.

Shoesmith, D.W. and S.Sunder. 1992. The prediction of nuclear fuel (UO_2) dissolution rates under waste disposal conditions. *J Nucl Mater* 190: 20-35.

Shoesmith, D.W., J.C.Tait, S.Sunder, W.J. Gray, S.A. Steward, R.E. Russo and J.D. Rudnicki. 1995. Factors affecting the differences in reactivity and dissolution rates between UO_2 and spent nuclear fuel. Atomic Energy of Canada Limited Report, AECL-11515, COG-95-581. Pinawa, Canada.

Shoesmith, D.W., J.J. Noel, Z.Qin, C.T Lee, J.S. Goldik, B.G. Santos and M.E. Broczkowski. 2005. Corrosion of nuclear fuel (UO_2) inside a failed nuclear waste container. Ontario Power Generation Report, 06819-REP-01200-10145-R00.

Shoesmith, D.W., J.S. Betteridge and W.H. Hocking. 1996. The cathodic reduction of oxygen on n-type UO_2 in dilute alkaline aqueous solution. *J Electroanal Chem* 406: 69-81.

Shoesmith, D.W., M. Kolar and F. King. 2003. A mixed potential model to predict fuel (uranium dioxide) corrosion within a failed nuclear waste container. *Corrosion* 59: 802-816.

Shoesmith, D.W., S. Sunder and J.C. Tait. 1998. Validation of an electrochemical model for the oxidative dissolution of used CANDU fuel. *J Nucl Mater* 257: 89-98.

Shoesmith, D.W., S. Sunder and W.H. Hocking. 1994. Electrochemistry of UO_2 nuclear fuel. In Electrochemistry of Novel Materials (J. Lipkowski and P.N. Ross, eds.). VCH Publishers, New York, USA. 297-337.

Shoesmith, D.W., S. Sunder, M.G. Bailey and D.G. Owen. 1983. Anodic oxidation of UO_2. III. Electrochemical studies in carbonate solutions. In Passivity of Metals and Semiconductors, Proceedings of the Fifth International Symposium on Passivity, Bombannes, France (M. Froment, ed.). Elsevier, Amsterdam, 125-130.

Shoesmith, D.W., S. Sunder, M.G. Bailey and G.J. Wallace. 1984. Anodic oxidation of UO_2. IV. Electrochemical and X-ray photoelectron spectroscopic studies in carbonate solutions. *Appl Surf Sci* 20: 39-57.

Shoesmith, D.W., S.Sunder, M.G. Bailey and G.J. Wallace. 1989. Corrosion of nuclear fuel in oxygenated solutions. *Corros Sci* 29: 1115-1128.

Smellie, J.A.T. and F. Karlsson. 1996. A reappraisal of some Cigar lake issues of importance to performance assessment. Swedish Nuclear Fuel and Waste Management Company Report, SKB-TR-96-08. Stockholm, Sweden.

Smith, H.J., J.C. Tait and R.E.V. Massow. 1987. Radioactive decay properties of Bruce A CANDU UO_2 fuel and fuel recycle waste. Atomic Energy of Canada Limited Report, AECL-9072. Pinawa, Canada.

Spahiu, K., D. Cui and M. Lundström. 2004. The fate of radiolytic oxidants during spent fuel leaching in the presence of dissolved near-field hydrogen. *Radiochim Acta* 92: 625-629.

Spahiu, K., L. Werme and U.-B. Eklund. 2000. The influence of near field hydrogen on actinide solubilities and spent fuel leaching. *Radiochim Acta* 88: 507-511.

Spahiu, K., U.-B. Eklund, D. Cui and M. Lundström. 2002. The influence of near field redox conditions on spent fuel leaching. *Mater Res Soc Symp P* 713: 633-638.

Spano, T.L., J.L. Niedziela, A.E. Shields, J. McFarlane, A. Zirakparvar, Z. Brubaker, R.J. Kapsimalis and A. Miskowiecz. 2020. Structural, spectroscopic, and kinetic insight into the heating rate dependence of studtite and metastudtite dehydration. *J Phys Chem C* 124: 26699-26713.

Spino, J., and D. Papaioannou. 2000. Lattice parameter changes associated with the rim structure formation in high burn-up UO_2 fuels by micro X-ray Diffraction. 2002. *J Nucl Mater* 281: 146-162.

Stroes-Gascoyne, D.L. Moir, M. Kolar, R.J. Porth. J.L. McConnell and A.N. Kerr. 1994. Measurement of gap and grain boundary inventories of ^{129}I in CANDU fuels. *Mater Res Soc Symp P* 353: 625-631.

Stroes-Gascoyne, S. 1996. Measurements of instant release source terms for ^{137}Cs, ^{90}Sr, ^{99}Tc, ^{129}I and ^{14}C in used CANDU fuel. *J Nucl Mater* 238: 264-277.

Stroes-Gascoyne, S. L.H. Johnson, D.M. Sellinger. 1987. The relationship between gap inventories of stable Xe, ^{137}Cs and ^{129}I in used fuel. *Nucl Technol* 77: 320-330.

Stroes-Gascoyne, S. J.C. Tait, N.C. Garisto, R.J. Porth, J.P.M. Ross, G.A. Glowa and T.R. Barnsdale. 1992a. Instant release of ^{14}C, ^{99}Tc, ^{90}Sr, ^{137}Cs from used CANDU fuel at 25°C in distilled deionized water. *Mater Res Soc Symp P* 257: 373-380.

Stroes-Gascoyne, S., F. Garisto and J.S. Betteridge. 2005. The effects of alpha-radiolysis on UO_2 dissolution determined from batch experiments with ^{238}Pu-doped UO_2. *J Nucl Mater* 346: 5-15.

Stroes-Gascoyne, S., F. King and J.S. Betteridge. 2001. The effects of alpha radiolysis on UO_2 dissolution determined from preliminary electrochemical experiments with ^{239}Pu-doped UO_2. Ontario Power Generation Report, 06819-REP-01300-10030-R00.

Stroes-Gascoyne, S., F.King, J.S. Betteridge and F. Garisto. 2002. The effects of alpha-radiolysis on UO_2 dissolution determined from electrochemical experiments with ^{238}Pu-doped UO_2. *Radiochim Acta* 90: 603-609.

Stroes-Gascoyne, S., L.H. Johnson, D.M. Sellinger, D.L. Wilkin. 1992b. Release of fission products and actinides from used CANDU fuel fragments under reducing conditions at 100°C. 1992. Atomic Energy of Canada Limited report AECL-10574, COG-92-31. Pinawa, Canada.

Stultz, J., M.T. Paffet and M.T. Joyce. 2004. Thermal evolution of hydrogen following water adsorption on defective $UO_2(100)$. *J Phys Chem B* 108: 2362-2364.

Stumm, W. (editor). 1990. Aquatic chemical kinetics: Reaction rates of processes in natural waters. John Wiley, New York, N.Y.

Sunder, S., D.W. Shoesmith, H. Christensen and N.H. Miller. 1992. Oxidation of UO_2 fuel by the products of gamma radiolysis of water. *J Nucl Mater* 190: 78-86.

Sunder, S. 1998. Calculation of radiation dose rates in a water layer in contact with used CANDU UO_2 fuel. *Nucl Technol* 122: 409-423.

Sunder, S., D.W. Shoesmith and N.H. Miller. 1997. Oxidation and dissolution of nuclear fuel (UO_2) by the products of the alpha radiation of water. *J Nucl Mater* 244: 66-74

Sunder, S., D.W. Shoesmith, R.J. Lemire, M.G. Bailey and G.J. Wallace. 1991a. The effect of pH on the corrosion of nuclear fuel (UO_2) in oxygenated solutions. *Corros Sci* 32: 373-386.

Sunder, S., G.D. Boyer and N.H. Miller. 1990. XPS studies of UO_2 oxidation by alpha radiolysis of water at 100^oC. *J Nucl Mater* 175: 163-169.

Sunder, S., J.J. Cramer and N.H. Miller. 1991b. X-ray photoelectron spectroscopy study of Cigar Lake uranium ore: A natural analog for used fuel. *Mater Res Soc Symp P* 257: 449-457.

Sunder, S., N.H. Miller and D.W. Shoesmith. 2004. Corrosion of uranium dioxide in hydrogen peroxide solutions. *Corros Sci* 46: 1095-1111.

Sunder, S., P. Taylor and J.J. Cramer. 1987. XPS and XRD studies of uranium rich minerals from Cigar Lake, Saskatchewan. *Mater Res Soc Symp P* 112: 465-472.

Sundin, S., B. Dahlgren, O. Roth and M. Jonsson. 2013. H_2O_2 and radiation induced dissolution of UO_2 and SIMFUEL in HCO_3^- deficient aqueous solution. *J Nucl Mater* 443: 291-297.

Sutton, H.C. and C.C. Winterbourn. 1989. On the participation of higher oxidation states of iron and copper in Fenton reactions. *Free Radical Bio Med* 6: 53-60.

Szenknect, S., A. Mesbah, T. Cordara, N. Clavier, H.-P. Brau, X. LeGoff, C. Poinssot, R.C. Ewing and N. Dacheaux. 2016. First experimental determination of the solubility constant for coffinite. *Geochim Cosmochim Ac* 181: 36-53.

Szenknect, S., D. Alby, M. Lopez Garcia, C. Wang, R. Podor, F. Miserque, A. Mesbah, L. Duro, L. Zetterstrom Evins, N. Dacheux, J. Bruno and R.C. Ewing. 2020. Coffinite formation from UO_{2+x}. *Sci Rep-UK* 10: 12168.

Tait, J.C. and J.M. Luht. 1997. Dissolution rates of uranium from unirradiated UO_2 and uranium and radionuclides from used CANDU fuel using the single-pass-flow-through apparatus. Ontario Hydro Report, No: 06819-REP-01200-0006-R00, Toronto, Canada.

Tait, J.C. and L.H. Johnson. 1986. Computer modelling of alpha radiolysis of aqueous solutions in contact with used UO_2 fuel. Proceedings of the 2nd International Conference on Radioactive Waste Management, Winnipeg, MB, Canada. Canadian Nuclear Society, Toronto, 611-615.

Tamura, H., K. Goto and M. Nagayama. 1976. The effect of ferric hydroxide on the oxygenation of ferrous ions in neutral solutions. *Corros Sci* 16: 197-207.

Thomas, G.F. and G. Till. 1984. The dissolution of unirradiated UO_2 fuel pellets under simulated disposal conditions. *Nucl Chem Waste Man* 5: 141-147.

Thomas, L.E., R.E. Einziger and H.C. Buchanan. 1993. Effect of fission products on air oxidation of LWR spent fuel, *J Nucl Mater* 201: 310-319.

Torrero, M.E., E. Baraj, J. de Pablo, J. Gimenez and I. Casas. 1997. Kinetics of corrosion and dissolution of uranium dioxide as a function of pH. *Int J Chem Kinet* 29: 261-267.

Trummer, M. and M. Jonsson. 2010. Resolving the H_2 effect on radiation induced dissolution of UO_2-based spent nuclear fuel. *J Nucl Mater* 396: 163-169.

Turner, A.S. and D.J. Wronkiewicz. 2002. Synthesis of uranium phosphate phases and potential retardation effects on spent fuel radionuclide migration. *Mater Res Soc Symp P* 757: 441-446.

Une, K., Y. Tominago and S. Kashibe. 1981. Oxygen potentials and lattice parameter of irradiated BWR fuel. *J Nucl Sci Technol* 28: 409- 417.

USA Department of Energy, Office of Civilian Radioactive Waste management. 2004. CSNF Waste form degradation: summary abstraction ANL-EBS-MD-000015 REV 02.

Vermilyea, D.A. 1966. The dissolution of ionic compounds in aqueous media. *J Electrochem Soc* 113: 1067-1070.

Verrall, R.A., Z. He and J.F. Mouris. 2005. Characterization of fuel oxidation in rods with clad-holes. *J Nucl Mater* 344: 240-245.

Vracar, Lj.M., D.B. Sepa and A. Damjanovic. 1986. Palladium electrode in oxygen-saturated aqueous solutions. *J Electrochem Soc* 133: 1835-1839.

Vracar, Lj.M., D.B. Sepa and A. Damjanovic. 1987. Palladium electrode in oxygen-saturated solution. *J Electrochem Soc* 134: 1695-1697.

Walenta, K. 1974. On studtite and its composition. *Am Mineral* 59: 166-171.

Wang, G., E.R. Batista and P. Yang. 2019. Excess electrons on reduced AnO_2 (111) surfaces (An = Th, U, Pu) and their impacts on catalytic water splitting. *J Phys Chem C* 123: 30245-30251.

Wasywich, K.M., W.H. Hocking, D.W. Shoesmith and P. Taylor. 1993. Differences in oxidation behaviour of used CANDU fuel during prolonged storage in moisture-saturated air and dry air at 150^0C. *Nucl Technol* 104: 309-329.

Weck, P.F., E. Kim, C.F. Jové-Colón and D.C. Sassani. 2012. Structures of uranyl peroxide hydrates: a first principles study of studtite and metastudtite. *Dalton T* 32: 9748-9752.

Welsh, T.L., R.B. Baker, D.R. Hansen, G.R. Golcar and B. Mackenas. 1996. Analysis of sludge from Hanford K-East Basin floor and weasel pit. Westinghouse Hanford Company Report, WHC-SP-1182. Richland, WA, USA.

Werme, L. and C. Lilja. 2010. Fuel and canister process report for the safety assessment SR-site. Swedish Nuclear Fuel and Waste Management Company Report, SKB-TR-10-46. Stockholm, Sweden.

Werme, L., L.H. Johnson, V.M. Oversby, F. King, K. Spahiu and D.W. Shoesmith. 2004. Spent fuel performance under repository conditions: a model for use in SR-Can. Swedish Nuclear Fuel and Waste Management Company SKB-TR-04-19. Stockholm, Sweden.

Wersin, P., M.F. Hochella Jr., P. Person, G. Redden, J.O. Lechie and D.W. Harris. 1994. Interaction between aqueous uranium (VI) and sulfide minerals: Spectroscopic evidence for sorption and reduction. *Geochim Cosmochim Ac* 58: 2829-2843.

White, A.F. 1995. Chemical weathering rates of silicate minerals. In Reviews in Mineralogy (White A.F. and Brantley S.L., eds.). *Am Mineral* 31: 407-462.

Willis, B.T.M. 1987. Crystallographic studies of anion excess uranium oxides. *J Chem Soc Faraday T* 2: 83, 1073-1081.

Wilson, C.N. and W.J. Gray. 1990. Measurement of soluble nuclide dissolution rates from spent fuel. *Mater Res Soc Symp P* 176: 489-498.

Woodall, S.D., M. Hambley, J. Rawcliffe, D. Willey and D. Hambley. 2021. Characterisation of corrosion products from degraded uranium dioxide fuel. *J Nucl Mater* 552: 152986.

Wren, J.C., D.W. Shoesmith and S. Sunder. 2005. Corrosion behaviour of uranium dioxide in alpha radiolytically decomposed water. *J Electrochem Soc* 152: B470-B481.

Wronkiewicz, D.J. 1999. Uranium: Mineralogy, geochemistry and the environment. *Rev Mineral* 38: 475-498.

Wronkiewicz, D.J., J.K. Bates, S.F. Wolf and E.E. Buck. 1996. Ten-year results from unsaturated drip tests with UO_2 at 90ºC. *J Nucl Mater* 238: 78-95.

Wronkiewicz, D.J., J.K. Bates, T. Gerding, E. Veleckis and B.S. Tani. 1992. Uranium release and secondary phase formation during unsaturated testing of UO_2 at 90ºC. *J Nucl Mater* 190: 107-127.

Wronkiewicz, D.J.W., E.C. Buck and J.K. Bates. 1997. Grain boundary corrosion and alteration phase formation during oxidative dissolution of UO_2 pellets. *Mater Res Soc Symp P* 465: 519-526.

Wu, L., J. Goldik and D.W. Shoesmith. 2014a. The anodic reactions on simulated spent fuel (SIMFUEL) in H_2O_2 solutions: Effect of carbonate/bicarbonate. *J Electrochem Soc* 161: C363-C371.

Wu, L. and D.W. Shoesmith. 2014. An electrochemical study of H_2O_2 oxidation and decomposition on simulated nuclear fuel (SIMFUEL). *Electrochim Acta* 137: 83-90.

Wu, L., Y. Beauregard, Z. Qin, S. Rohani and D.W. Shoesmith. 2012. A model for the influence of steel corrosion products on nuclear fuel corrosion under permanent disposal conditions. *Corros Sci* 61: 83-91.

Wu, L., Z. Qin and D.W. Shoesmith. 2014b. An improved model for the corrosion of used fuel inside a failed waste container under permanent disposal conditions. *Corros Sci* 84: 85-95.

Wu, L., N. Liu, Z. Qin and D.W. Shoesmith. 2014c. Modeling the radiolytic corrosion of fractured nuclear fuel under permanent disposal conditions. *J Electrochem Soc* 161: E3259-E3266.

Yajima, T., Y.Kawamura and S. Ueta. 1995. Uranium (IV) solubility and hydrolysis constants under reducing conditions. 1995. *Mater Res Soc Symp P* 353: 1137-1142.

Yang, M., A.B. Fidalgo, S. Sundin and M. Jonsson. 2013. Inhibition of radiation induced dissolution of UO_2 by sulphide – A comparison with the hydrogen effect. *J Nucl Mater* 434: 38-42.

You, G.S., K.S. Kim, D.K. Min and S.G. Ro. 2000. Oxidation kinetic changes of UO_2 by additive addition and irradiation. *J Nucl Mater* 277: 325-332.

Zanonato, P.L., P. Di Bernado, Z. Szabo and I. Grenthe. 2012. Chemical equilibria in the uranyl (VI) -peroxide-carbonate system; identification of precursors for the formation of poly-peroxometallates. *Dalton T* 41: 11635-11641.

Zepp, R.G., B.G. Faust and J. Hoigné. 1992. Hydroxyl radical formation in aqueous reactions (pH 3-8) of iron (II) with hydrogen peroxide. The photo-Fenton reaction. *Environ Sci Technol* 26: 313-319.

Zhu, Z. 2018. The electrochemical study of simulated spent nuclear fuel (SIMFUEL) corrosion under permanent disposal conditions. Chapter 5. Ph.D. Thesis, University of Western Ontario, London, Canada.

Zhu, Z., J.J. Noel and D.W. Shoesmith. 2020. Hydrogen peroxide decomposition on simulated nuclear fuel in bicarbonate/carbonate solutions. *Electrochim Acta* 340: 135980.

Zhu, Z., L. Wu, J.J. Noël and D.W. Shoesmith. 2019. Anodic reactions occurring on simulated spent nuclear fuel (SIMFUEL) in hydrogen peroxide solutions containing bicarbonate/carbonate – the effect of fission products. *Electrochim Acta* 320: 134546.

Zigah, D., J. Rodriguez-Lopez and A.J. Bard. 2012. Catalytic decomposition of H_2O_2 leads to the formation of intermediate radical species which can bind to oxide surfaces on which decomposition occurs. *Phys Chem Chem Phys* 14: 12764-12772.